



저작자표시-비영리-변경금지 2.0 대한민국

이용자는 아래의 조건을 따르는 경우에 한하여 자유롭게

- 이 저작물을 복제, 배포, 전송, 전시, 공연 및 방송할 수 있습니다.

다음과 같은 조건을 따라야 합니다:



저작자표시. 귀하는 원저작자를 표시하여야 합니다.



비영리. 귀하는 이 저작물을 영리 목적으로 이용할 수 없습니다.



변경금지. 귀하는 이 저작물을 개작, 변형 또는 가공할 수 없습니다.

- 귀하는, 이 저작물의 재이용이나 배포의 경우, 이 저작물에 적용된 이용허락조건을 명확하게 나타내어야 합니다.
- 저작권자로부터 별도의 허가를 받으면 이러한 조건들은 적용되지 않습니다.

저작권법에 따른 이용자의 권리는 위의 내용에 의하여 영향을 받지 않습니다.

이것은 [이용허락규약\(Legal Code\)](#)을 이해하기 쉽게 요약한 것입니다.

[Disclaimer](#)

공학박사 학위논문

Finite Element Simulation of Hole Expansion Test using Microstructure based Dual-Scale Approach

미세조직 기반 다중 스케일 유한요소해석을
통한 강재의 구멍 확장성 예측

2021년 2월

서울대학교 대학원

재료공학부

박 시 욱

Finite Element Simulation of Hole Expansion Test using Microstructure based Dual-Scale Approach

지도 교수 한 홍 남

이 논문을 공학박사 학위논문으로 제출함
2021년 1월

서울대학교 대학원
재료공학부
박 시 옥

박시옥의 공학박사 학위논문을 인준함
2021년 1월

위 원 장 유 응 열

부위원장 한 홍 남

위 원 이 명 규

위 원 최 시 훈

위 원 한 상 호



(인)



(인)

ABSTRACT

With increasing attention to the reduction of fuel consumption and CO₂ emissions, many researchers globally have focused their research efforts on lightweight materials for automotive applications. Accordingly, steel makers have developed advanced high strength steels (AHSS) with superior combination of strength and ductility to conventional steels. Currently, over 30-50% of manufactured vehicle bodies are made of AHSS. However, even with improved ductility or formability of AHSS, premature edge cracking remains a challenge in formation of automotive parts with the AHSS. Though there have been many studies related to the prediction of forming limits during the sheet-metal forming process, it has been reported that the conventional methods for evaluating the ductility from uniaxial tensile tests or formability from the forming limit diagrams (FLD) are not appropriate because the edge cracking does not represent obvious localization before fracture. Therefore, other evaluation methods for the stretch-flangeability involving cracking at the sheet edge or flange should be investigated to replace the formability evaluation methods based on classical tensile tests or FLD. As an alternative to the formability evaluation using the FLD, a hole expansion test (HET) was proposed to quantitatively measure the stretch-flangeability of sheet metals. Therefore, in this study, a study was conducted to propose a new method to more accurately predict the HER of AHSS.

Firstly, a dual-scale finite element model is proposed to investigate the failure of AHSSs (ferrite-bainite dual-phase steel, hyper-burring ferrite single phase steel) in the hole expansion test. The dual-scale approach consists of finite element simulation in the following two steps. The first level simulation solves the elastic-plastic deformation behavior with phenomenological isotropic elastic-anisotropic plastic constitutive models, and its resulting local deformation histories are supplied to the second level simulation as boundary conditions. In the second level simulation, the local microstructure evolution is solved and provides the dislocation densities, equivalent plastic strains. A special formulation for calculating the dislocation density distribution in the form of dislocation pile-up at grain boundary areas is highlighted as the microscale level constitutive law. The microstructural information is provided from image analyses based on grain average image quality and grain average misorientation values observed using electron backscatter diffraction (EBSD). The data were used to identify the constituent phases of the investigated steel as the major input for the microstructure-based representative volume element (RVE). Nanoindentation tests are employed to validate the identified phase and to extract the phase-level mechanical properties. The distribution of dislocation pile-up within the microstructure calculated through FE simulation was verified by comparison with the distribution of geometrically necessary dislocations calculated from EBSD misorientation data.

Secondly, the damage at the hole edge caused by the shearing (punching) process was analyzed by dividing it into three factors: surface roughness, hole edge

geometry, and work hardening near the hole edge. Each factor was analyzed for various clearance conditions. Confocal microscopy was used to analyze the effect of surface roughness and hole edge geometry on HER. The concept of neighbor roughness deviation (NRD) was introduced as a method to quantitatively analyze the surface roughness of hole edge (both for the fractured zone and sheared zone), and FE modeling was performed using the measured dimension of hole edges. To consider the work hardening near the hole edge caused by the punching process, the hardness profile was measured along the radial direction, which was converted into an equivalent plastic strain and set as a pre-strain in the FE model.

Thirdly, the onset of failure at the hole edge during the hole expansion test is simulated by the proposed dual-scale numerical approach. Besides the plasticity in the hole expansion test, the ductile fracture model was implemented by monitoring the local stress triaxiality in the microscale simulation. For the parameter identification of local stress triaxiality fracture criterion, experiments and simulations were performed by fabricating notched tensile specimens with various notch radii to examine triaxiality evolution in different stress states.

Lastly, from the proposed fracture criterion and dislocation based hardening model incorporating dislocation pile-up near the grain boundaries, the microscale RVE simulations of hole expansion test were conducted. The simulation results showed that both the hole expansion ratio (HER) and the location of failure can be predicted successfully using the proposed dual scale scheme. For model verification, the dual-scale simulation was applied to the ferrite single phase steel, hyper burring

steel, and it was found that the predicted HER falls within the error range of the measured value.

From this study, a new simulation approach was developed to predict the HER of AHSS steel more accurately and practically. The example clarifies that the present approach based on local deformation histories and the resultant microstructure evolution with grain-level deformation inhomogeneity can be utilized for understanding the deformation and fracture of various type of steels. In addition, it can be used for microstructure design through analysis of the deformation behavior according to grain size and grain boundary characteristics.

Keywords: Dual-scale simulation, Finite element method (FEM), Hole expansion ratio, Sheared edge formability, Dislocation pile-up, Fracture criterion, Stress triaxiality, Ferrite-bainite steel, Hyper-burring steel, Phase identification, EBSD, TEM, Tensile test, Punching.

Student number: 2015-20818

Contents

Abstract	I
Table of Contents	V
List of Tables	X
List of Figures	XII

Chapter 1

Introduction

1.1 Limitation of prediction of formability of advanced high strength steel (AHSS)	1
1.2 Hole expansion ratio (HER)	2
1.3 Thesis motivation	5
1.4 References	6

Chapter 2

Microstructure and mechanical behavior of ferrite bainite steel

2.1 Introduction	7
2.2 Experimental procedure	8
2.2.1 Electron backscattered diffraction (EBSD)	8
2.2.2 Uniaxial tensile test	14
2.2.3 Nanoindentation	18
2.2.4 Hole expansion test	21
2.3 Conclusion	23
2.4 References	24

Chapter 3

Dual scale finite element simulation

3.1 Introduction	25
-------------------------------	----

3.2 Macroscale simulation	30
3.2.1 Uniaxial tensile test	30
3.2.2 Nanoindentation	36
3.2.3 Hole expansion test	41
3.3 Microscale simulation	46
3.3.1 Representative volume elements (RVEs)	46
3.3.2 Constitutive equation	49
3.3.3 Microscale parameter identification	56
3.3.4 Fracture criterion using local stress triaxiality	63
3.3.5 Hole expansion test	72
3.3.6 Dependence of strength difference of constituent phase on HER	79
3.4 Conclusion	83
3.5 References	85

Chapter 4

Prediction of hole expansion ratio for hyper burring steel

4.1 Introduction	88
4.2 Microstructure and mechanical behavior	90
4.3 Dual-scale FE simulation	96
4.3.1 Macroscale simulation	96
4.3.2 Microscale simulation	103
4.3.3 Fracture criterion	109
4.3.4 Hole expansion test	116
4.4 Effect of microstructural factors on HER: numerical sensitivity study	124
4.4.1 Grain size	124
4.4.2 Grain boundary characteristics	129
4.5 Conclusion	132
4.6 References	133

Chapter 5

Punching effect on hole expansion ratio

5.1 Introduction	135
5.2 Punch-die clearance	138
5.3 Surface roughness effect on HER	140
5.4 Geometrical effect	144
5.5 Work hardening effect	149
5.5.1 Grain size	149
5.5.2 Grain boundary characteristics	153
5.6 Conclusion	156
5.7 References	158

Chapter 6

Total conclusion	160
-------------------------------	------------

LIST OF TABLES

Table 2.1 The mean and standard deviation of grain average IQ and grain average misorientation distribution for each phase.

Table 2.2 Mechanical properties of the FB steel.

Table 3.1 Optimized material parameters for mixed Swift-Voce model (Eqs. (2) - (4)).

Table 3.2 Identified material parameters for the Hill1948 (Eq. (1)).

Table 3.3 Material constants for the dislocation based hardening model in Eq. (5) [28].

Table 3.4 Optimized parameters used for the microscale model (Eqs. (6), (11)).

Table 3.5 Material constants for local stress triaxiality fracture model (Eq. (16)).

Table 3.6 Material constants of local stress triaxiality fracture model for Cond. 2 (Eq. (16)).

Table 4.1 Chemical composition of HB780 steel sheet (weight %).

Table 4.2 Chemical composition of HB780 steel sheet (weight %).

Table 4.3 Optimized material parameters used in macro and micro constitutive equations.

Table 4.4 Material constants for the dislocation-density-based hardening model [3].

Table 4.5 Critical fracture values and material constants for each fracture criterion.

Table 4.6 Optimized material parameters and predicted HER values from the local stress triaxiality criterion for the microscale model with different grain sizes.

Table 4.7 Optimized material parameters and predicted HER values from the local stress triaxiality criterion for the microscale model of Cond.2–4.

LIST OF FIGURES

Figure 1.1 Schematic image of the hole expansion test.

Figure 2.1 Microstructure of hot-rolled FB steel. (a) Grain average IQ map, (b) grain average misorientation map, and (c) ND inverse pole figure (IPF) map.

Figure 2.2 Distribution of (a) grain average IQ and (b) grain average misorientation.

Each distribution is fitted with lognormal distribution for each phase.

Figure 2.3 The tensile specimen dimension for smooth and notched tension.

Figure 2.4 The stress–strain curves (a) for each direction and (b) for both smooth and notched tensile tests.

Figure 2.5 (a) The EBSD image with SPM image at indented area and (b) the resulting load–displacement curves.

Figure 3.1 Flowchart of dual-scale simulation.

Figure 3.2 Results of experimental and simulated stress–strain curves: (a)

Experimental stress–strain curves along RD, TD, and DD; (b)–(d) the experimental stress–strain curve (dot) and curves simulated using Hill1948 yield function (red line) and isotropic yield function (blue line) along RD, TD, and DD.

Figure 3.3 The finite element model for macroscale simulation of nanoindentation.

Contour map shows the displacement along z-direction.

Figure 3.4 The experimental and simulated load–displacement curves for each phase and the resulting stress–strain curves. (a) Bainite phase, (b) ferrite phase, and (c) stress–strain curves for the investigated steel and constituent phases. The dotted curves are obtained from uniaxial tensile test for the investigated steel and macroscale nanoindentation simulation for each constituent phase. The solid lines correspond to the results of microscale RVE simulation.

Figure 3.5 Schematic representation of the HET and (b) mesh configuration of the specimen.

Figure 3.6 Deformed mesh after the hole expansion test simulation (Contour map of effective stress) and true strain versus HER for various spots. (a) Contour map of Mises stress during the hole expansion test indicating the extraction position of principal strain, (b) ~ (d) principal strains extracted at the RD hole edge along the thickness direction (Spot 1, Spot 2, and Spot 3), (e) ~ (g) principal strains extracted at the DD hole edge along thickness direction (Spot 1, Spot 2, and Spot 3), (h) ~ (j) principal strains extracted at the TD hole edge along thickness direction (Spot 1, Spot 2, and Spot 3). The black, red, and blue lines refer to the maximum, medium, and minimum principal strain, respectively.

Figure 3.7 (a) Thickness strains along the radial direction at (a) RD, (b) DD, and (c) TD of FB steel. The scale of the magnified graph is from 13.5 to 16 mm on the x-axis and -0.55 to -0.3 on the y-axis, and the major grids are drawn at intervals of 0.5 mm and 0.05, respectively. The details of spatial radial coordinates are schematically shown on the lower right of the figure.

Figure 3.8 RVE constructed from the measured EBSD image. (a) IPF map, (b)

geometry part, and (c) mesh constructed for FE simulation.

Figure 3.9 Two-beam bright-field TEM images showing the dislocation source length of the investigated steel.

Figure 3.10 (a) Schematic image of 3D RVE and (b) strain histories obtained from the macroscale simulation.

Figure 3.11 Contour map of (a) effective stress (MPa), (b) dislocation density ($1/\text{m}^2$), and (c) logarithmic strain under the macroscopic strain of 0.02.

Figure 3.12 Distributions of dislocation density at strain 4 % (a-d), and 6 % (e-h).

The FE simulated dislocation densities (b, f), the geometrically necessary dislocation densities for dual-phase (d, h), and for only ferrite phase (c, g) were calculated from the measured local misorientation. The enlarged images (a, e) show the same scale of microstructure as RVE model.

Figure 3.13 (a) Phase map of FB steel and contour map (top view) of (b) effective stress and (c) stress triaxiality. The grain boundary elements are superimposed on

each contour map.

Figure 3.14 Averaged stress triaxiality versus equivalent plastic strain calculated from the microscale simulation of uniaxial tensile tests.

Figure 3.15 (a) Averaged stress triaxiality versus equivalent plastic strain calculated from the microscale simulation of uniaxial tensile tests. (b) The hole edge image after the hole expansion test. The red circle indicates the location of crack initiated during the hole expansion test.

Figure 3.16 Experimental and predicted HER for each position.

Figure 3.17 Equivalent plastic strain at the onset of fracture and stress triaxiality at initial deformation for the spot 1-3 of RD hole edge.

Figure 3.18 (a) Fracture criterion derived from macroscale uniaxial tensile tests and (b) deformation histories for spot 1-3 of RD hole edge calculated from macroscale simulation of hole expansion test.

Figure 3.19 (a) The stress–strain behaviors of ferrite and bainite of the investigated FB steel (Cond. 1) and those of when the strength between the two phases is deliberately set small (Cond. 2) and (b) the fracture criterion obtained through microscale simulation for each condition.

Figure 3.20 The deformation history in RD Spot 1 for Cond.1 and Cond. 2.

Figure 4.1 Microstructure of the investigated steel. (a) IQ map and (b) ND inverse pole figure map.

Figure 4.2 Results of uniaxial tensile tests: (a) Experimental load–displacement curves for the smooth and notched tensile tests, (b) comparison between the experimental engineering stress–strain curve and the one simulated (blue line) using the Swift hardening model, and (c) comparison between the experimental and simulated (red line) true stress–strain curves using dislocation-based constitutive equations.

Figure 4.3 Finite element models of the uniaxial tensile tests. The thickness of all

models is 3 mm.

Figure 4.4 (a) Finite element model of the HET and (b) mesh configuration of the specimen.

Figure 4.5 Deformed mesh after the HET simulation. The strain histories were extracted at three points of the hole edge (i.e. Spot 1, Spot 2, Spot 3).

Figure 4.6 (a) RVE generated from the EBSD image. (a) IPF map, (b) grain boundary map, and (c) mesh generated from microstructure image.

Figure 4.7 Contour map of (a) dislocation density ($1/m^2$), (b) effective stress (MPa), and (c) logarithmic strain under the macroscopic strain of 0.10.

Figure 4.8 Contour map (top view) of stress triaxiality under the uniaxial tension at the strain of 0.1. The grain boundary elements are superimposed.

Figure 4.9 (a) Simulated local stress triaxiality during the uniaxial tensile tests and (b) the relationship between the equivalent strain to fracture and stress triaxiality

under various stress conditions.

Figure 4.10 Contour map (top view) of constant fracture strain (a) Spot 1 (HER: 225%), (b) Spot 2 (HER: 228%), (c) Spot 3 (HER: 207%).

Figure 4.11 Contour map (top view) of the Cockcroft–Latham criterion (a) Spot 1 (HER: > 245.7%), (b) Spot 2 (HER: > 245.7%), (c) Spot 3 (HER: > 245.7%). No fracture occurred for each spot over an HER of 245.7%.

Figure 4.12 Contour map (top view) of the Clift criterion (a) Spot 1 (HER: 233%), (b) Spot 2 (HER: 235%), (c) Spot 3 (HER: 215%).

Figure 4.13 (a) Equivalent plastic strains of three critical elements at each spot as a function of stress triaxiality and (b) the apparent fracture strain considering the deformation history at spot 1.

Figure 4.14 HER values predicted using various fracture criteria.

Figure 4.15 Five types of microstructure models. The size of the model has expanded

to 2, 3, 4, and 5 times that of the original model (the leftmost one).

Figure 4.16 Apparent fracture strain and deformation history for models with grain sizes of (a) 10 μm , (b) 15 μm , (c) 20 μm , and (d) 25 μm .

Figure 4.17 Effect of grain boundary characteristics (or dislocation distribution) on HER. (a) The contour map of dislocation density under the true strain of 0.12. The magnified image shows the profiling direction and the distance of dislocation density, (b) the profile of dislocation density, and (c) the predicted HER for each condition.

Figure 5.1 The schematic representation of punch process.

Figure 5.2 The confocal microscope image of hole edge and the neighbor roughness distribution (NRD) mapping of measured image.

Figure 5.3 The relationship between the NRD and HER for each clearance. Averaged NRD for (a) whole edge region, (b) only fracture region, (c) only fracture region with NRD value over 10 μm .

Figure 5.4 The schematic representation of hole edge for each clearance condition.

Figure 5.5 Averaged stress triaxiality versus equivalent plastic strain calculated from the microscale simulation of hole expansion tests.

Figure 5.6 Predicted HER from microscale RVE simulation for various clearance condition (work hardening is not considered).

Figure 5.7 Experimentally measured hardness profile for each clearance condition.

Figure 5.8 Calculated strain histories at the hole edge (spot 1) during the hole expansion test for the samples with and without hardening effect.

Figure 5.9 The microscale RVE model after applying work hardening effect as a pre-strain and averaged stress triaxiality versus equivalent plastic strain calculated from the microscale simulation of hole expansion test.

Figure 5.10 Experimental and predicted HER for each clearance condition.

Chapter 1

Introduction

1.1 Limitation of prediction of formability of advanced high strength steel (AHSS)

With increasing attention to the reduction of fuel consumption and CO₂ emissions, many researchers globally have focused their research efforts on lightweight materials for automotive applications. Accordingly, steel makers have developed advanced high strength steels (AHSS) with superior combination of strength and ductility to conventional steels. Currently, over 30-50% of manufactured vehicle bodies are made of AHSS [1]. However, even with improved ductility or formability of AHSS, premature edge cracking remains a challenge in formation of automotive parts with the AHSS. Though there have been many studies related to the prediction of forming limits during the sheet-metal forming process [2, 3], it has been reported that the conventional methods for evaluating the ductility from uniaxial tensile tests or formability from the forming limit diagrams (FLD) are not appropriate because the edge cracking does not represent obvious localization before fracture. Therefore, other evaluation methods for the stretch-flangeability involving cracking at the sheet edge or flange should be investigated to replace the formability evaluation methods based on classical tensile tests or FLD.

1.2 Hole expansion ratio (HER)

As an alternative to the formability evaluation using the FLD, a hole expansion test (HET) was proposed to quantitatively measure the stretch-flangeability of sheet metals. This test uses sheets with a circular hole at the center of sample and expands the hole by either conical-shaped punch or flat bottom punch before the onset of through-thickness crack at the hole edge. The stretch-flangeability is quantified by a hole expansion ratio (HER), which is defined as the ratio of the expanded hole diameter at the instance of crack formation to the initial hole diameter.

$$HER(\%) = \frac{d_f - d_0}{d_0} \times 100 \quad (1)$$

The d_0 and d_f are the initial and final hole diameter, respectively. The final hole diameter was measured right after the onset of hole edge fracture. The schematic view of the HET is shown on Fig. 1.1. It is reported that the hole expansion ratio (HER) is highest for a conical punch and lowest for a flat-bottom punch [4], which is the result of difference in the deformation behavior and strain gradient through the thickness of the sheet [5]. It is well known that the HER is highly sensitive to the microstructure of materials and the edge surface conditions introduced during the hole fabrication. For example, Kim et al. [6] investigated the effect of a dual-phase microstructure on the hole expansion formability of DP980 steels of the same strength grade with different microstructural morphologies and martensite volume fractions. Mori et al. [7] investigated the stretch-flangeability of an ultra-high-

strength steel sheet by improving the quality of sheared edge. Levy et al. [5] also investigated the effect of shearing process on sheared-edge stretching, and observed that the shear-affected zone, which is a zone of deformation adjacent to the shear face, has the dominant effect on sheared-edge stretchability.

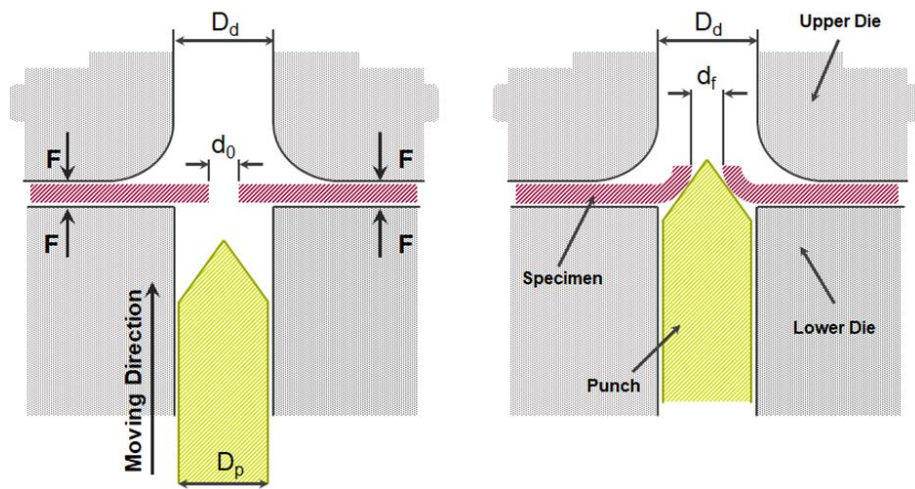


Figure 1.1 Schematic image of the hole expansion test.

1.3 Thesis motivation

In this study, a new microstructure based dual-scale FE simulation is proposed to predict deformation and failure of steel sheet under the HET. In the first level simulation, the elastic-plastic deformation of steel sheet during the HET is solved with conventional phenomenological elastic-anisotropic plasticity constitutive models. The second level simulation predicts the local microstructure evolution and provides the dislocation densities, local plastic deformation, and distributed stress triaxiality that predict the local failure in the microstructure of investigated steel. A dislocation density based hardening model is developed and implemented in the microscale simulation to include the effect of dislocation pile-up at grain boundary areas. Experimental novelty is highlighted by identifying the constituent phases and their mechanical properties in investigated steel using the grain average image quality, grain average misorientation values observed by electron backscatter diffraction (EBSD), and nanoindentation test. Finally, the failure at the hole edge during the HET is simulated by the proposed dual-scale simulations, and the accuracy of the modeling is validated by predicting the hole expansion ratio (HER) and the location of failure at the hole edge.

1.4 References

- [1] N. Lutsey, Review of technical literature and trends related to automobile mass-reduction technology, 2010.
- [2] H.N. Han, K.-H. Kim, J. Mater. Process. Tech. 142(1) (2003) 231-238.
- [3] V. Uthaisangsuk, U. Prahl, S. Münstermann, W. Bleck, Comput. Mater. Sci. 43(1) (2008) 43-50.
- [4] A. Konieczny, T. Henderson, SAE Transactions (2007) 20-29.
- [5] B. Levy, C. Van Tyne, J. Mater. Eng. Perform. 21(7) (2012) 1205-1213.
- [6] J.H. Kim, M.-G. Lee, D. Kim, D.K. Matlock, R. Wagoner, Mater. Sci. Eng. A 527(27-28) (2010) 7353-7363.
- [7] T. Mori, K. Tanaka, Acta Metall. 21(5) (1973) 571-574.

Chapter 2

Microstructure and mechanical behavior of ferrite bainite steel

2.1 Introduction

Dual phase steels are widely used for automobile part due to its high strength and formability. The most widely used type of dual phase steel is a ferrite-martensite type DP steel consisting of a soft ferrite and a hard martensite phase, and has a higher hardening rate and longer uniform elongation than a single phase steel. However, ferrite and martensite are known to have low stretch-flangeability due to the large difference in hardness between the two phases. To improve this low stretch-flangeability problem, steel with a microstructure of ferrite-bainite was developed. Ferrite-bainite steel has also been reported to have lower yield ratio, the ratio of yield strength to tensile strength, and at the same time have higher strain hardenability [1]. It has been reported that the ferrite bainite steel has the highest strain hardenability when the steel consist of ferrite with 30-40% of bainite phase [2]. In this study, a hot rolled ferrite-bainite (FB) steel sheet with a chemical composition of Fe-1.5Mn-1.5Si-0.06C (wt.%) and a thickness of 2.7 mm was investigated. Ferrite and bainite phases with the same body centered cubic (BCC) crystal structure were distinguished by grain average image quality (IQ) map and grain average misorientation.

2.2 Experimental

2.2.1 Electron backscattered diffraction (EBSD)

A hot rolled ferrite-bainite (FB) steel sheet with a chemical composition of Fe-1.5Mn-1.5Si-0.06C (wt.%) and a thickness of 2.7 mm was investigated. The microstructure of the FB steel sheet was observed using FE-SEM equipped with electron backscattered diffraction (EBSD) system (FE-SEM: SU70, Hitachi, Japan and EBSD: Hikari EBSD detector with TSL OIM 7.3 software, EDAX/TSL, USA). Specimens were prepared by a mechanical grinding followed by electropolishing with a solution of 10% perchloric acid and 90% ethanol at a temperature of 20 °C and a voltage of 24 V. In the observation of EBSD, the accelerating voltage was 15 kV and the working distance was 15 mm. The step size was set to 0.2 μm , and a critical misorientation angle of 5° was adopted for grain identification.

The microstructures measured from EBSD of investigated FB steel are displayed in Fig. 2.1. Owing to their identical body centered cubic (BCC) crystal structure, it is difficult to distinguish the ferrite and bainite phases of the investigated FB steel using the electron backscatter Kikuchi patterns. Therefore, numerous studies have been conducted on phase identification using other indicators that can be obtained from EBSD analyses. The low temperature induced phases such as martensite and bainite frequently reveal an inferior EBSD pattern quality (PQ) and band contrast (BC) due to the severe deformation during phase transformation [3]. Kang et al. [4] discriminated the martensite phase from ferrite phase in DP steel using the threshold value of grain averaged BC and Li et al. [5] segmented bainite phase

from ferrite phase from the value of grain orientation spread. Consequently, Wilson et al. [6] reported that the ferrite and martensite phases in dual phase steel could be successfully identified by using the PQ value. As an alternative to the PQ analysis, the image quality (IQ) and kernel average misorientation (KAM) have been applied to identify the phases in steels. For example, Wu et al. [7] distinguished the martensite phase from matrix ferrite by separating an IQ profile into two Gaussian peaks and Zaefferer et al. [8] suggested a new analysis option using the grain reference orientation deviation (GROD) and KAM to separate the bainitic ferrite and ferrite phases. In this study, the grain average IQ and grain average misorientation values are used to identify the constituent phases of the investigated FB steel. The distributions of grain average IQ and grain average misorientation are shown on Fig. 2.2a and b, respectively. As expected, both grain average IQ and grain average misorientation show bimodal distribution because the FB steel consists of two phases. When the bainite phase degraded grain average IQ and the higher value of grain average misorientation were compared with the ferrite phase, each distribution was divided into two lognormal distributions, which is defined as follows:

$$y = \frac{1}{x\sigma_{ln} \sqrt{2\pi}} \exp \left\{ -\frac{(\log x - \mu_{ln})^2}{2\sigma_{ln}^2} \right\} \quad (1)$$

$$m = \exp(\mu_{ln} + \sigma_{ln}^2 / 2) \quad (2)$$

$$s = \exp(2\mu_{ln} + \sigma_{ln}^2)(\exp(\sigma_{ln}^2) - 1) \quad (3)$$

where m and s are mean and standard deviation of logarithmic values, respectively,

and μ_{lnd} and σ_{lnd} are the lognormal distribution parameters. From the phase identification results, the fraction of bainite phase was approximately 30%. The mean and standard deviation of the grain average IQ and grain average misorientation distribution for each phase are listed in Table 2.1.

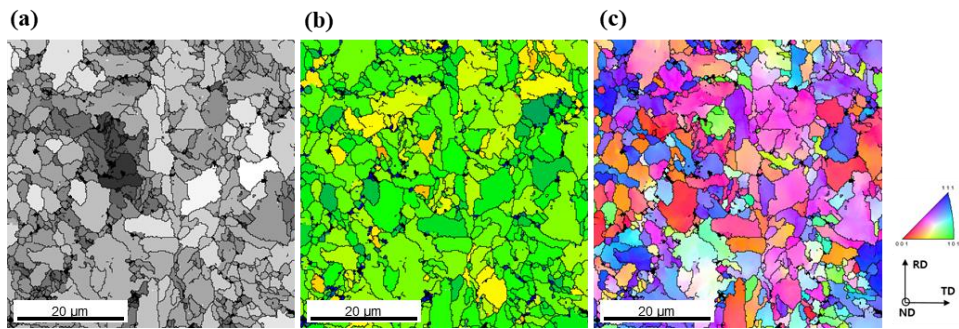


Figure 2.1 Microstructure of hot-rolled FB steel. (a) Grain average IQ map, (b) grain average misorientation map, and (c) ND inverse pole figure (IPF) map.

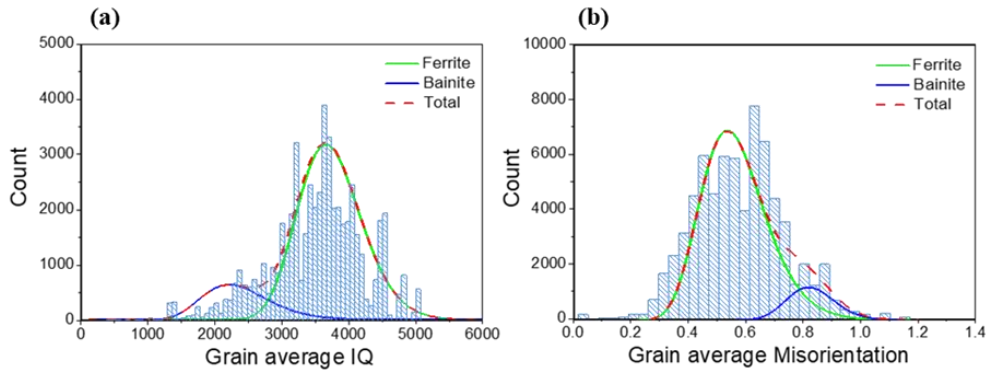


Figure 2.2 Distribution of (a) grain average IQ and (b) grain average misorientation.

Each distribution is fitted with lognormal distribution for each phase.

Table 2.1 The mean and standard deviation of grain average image quality and grain average misorientation distribution for each phase.

	Grain average IQ		Grain average misorientation	
	Mean (m)	Standard deviation (s)	Mean (m)	Standard deviation (s)
Ferrite	3745.1	481.3	0.566	0.013
Bainite	2367.4	519.8	0.828	0.007

2.2.2 Uniaxial tensile test

The basic mechanical properties were obtained from the standard uniaxial tensile tests following the ASTM E8 standard. To investigate the plastic anisotropy of ferrite-bainite steel, sub-sized specimens with the dimensions 25 mm × 6 mm (length × width in gage section) fabricated along 0°, 45° (diagonal direction, DD), and 90° (transverse direction, TD) from RD. The R-value which shows the state of anisotropy is measured during the uniaxial tensile test. This is defined as the ratio of width strain, $\epsilon_w = \ln(w/w_0)$, to thickness strain, $\epsilon_t = \ln(t/t_0)$.

$$R = \frac{\ln \frac{w}{w_0}}{\ln \frac{w_0 l_0}{wl}} \quad (4)$$

The measurement of R-value is taken at the engineering strain of 5%. Besides the standard tensile specimen, the notched tensile specimens with notch radii of 2, 4, 6, and 12 mm were fabricated for the notched tensile tests. The specimen dimension for smooth and notched tensile tests are presented in Fig. 2.3. The tensile strain rate was set to be 0.001/s. The stress–strain curves for each direction are presented in Fig. 2.4a and the curves for both smooth and notched tensile tests are shown in Fig. 2.4b. The mechanical properties of the hot-rolled FB steel are listed in Table 2.2.

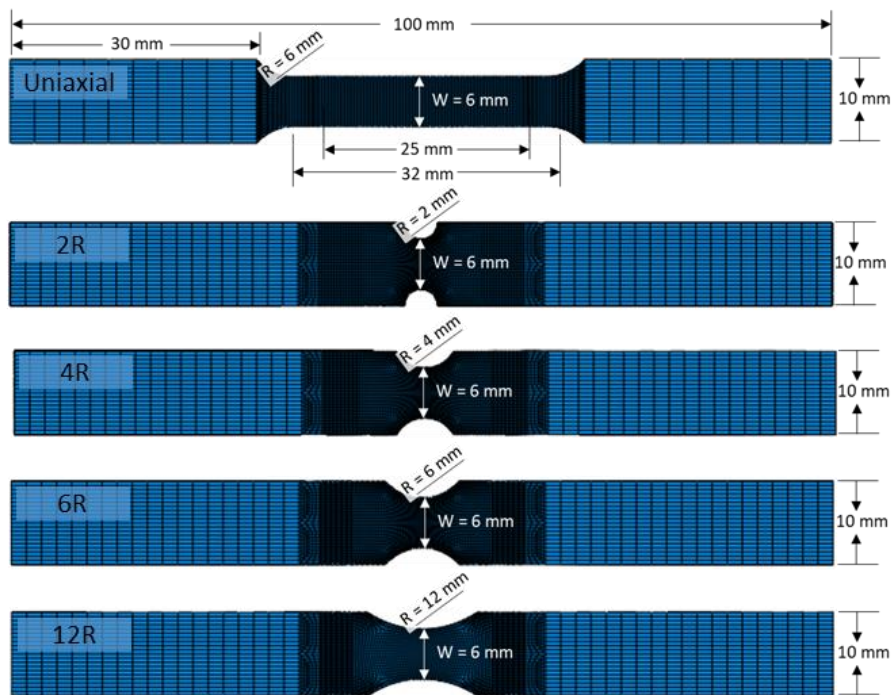


Figure 2.3 The tensile specimen dimension for smooth and notched tension.

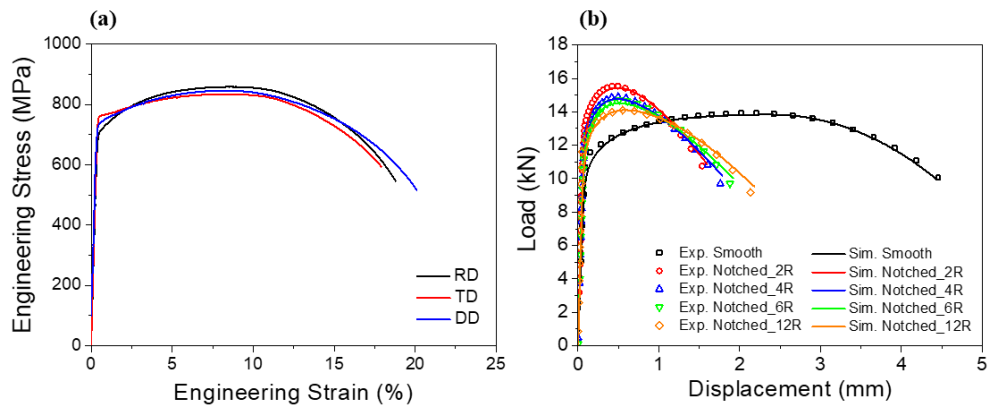


Figure 2.4 The stress–strain curves (a) for each direction and (b) for both smooth and notched tensile tests.

Table 2.2 Mechanical properties of the FB steel.

Tensile direction from RD (°)	Young's modulus (GPa)	Poisson's ratio	Yield stress (MPa)	Tensile stress (MPa)	Uniform elongation (%)	Post elongation (%)	R- value
0	209	0.3	714.2	858.8	8.67	10.12	0.8147
45	209	0.3	742.7	846.1	8.29	11.80	1.0786
90	209	0.3	764.1	834.1	8.44	9.47	0.9376

2.2.3 Nanoindentation

The nanoindentation test was performed to measure the mechanical properties of each phase and verify the phase separation results conducted using EBSD data. The tests were conducted in a load control mode using the Hysitron TI 750 Ubi (Minneapolis, MN) nanoindentation system with a Berkovich-type diamond indenter having a radius of 450 nm. The indenter tip moved linearly for 5 s up to the load of 1 mN, followed by unloading down to 0 N in 5 s. To eliminate any effect of grain boundary during the indentation, only those indentations located inside the grains were selected for analysis, with the aid of a scanning probe microscope (SPM). By comparing the EBSD image with the SPM image, in which the phase separation was completed through the previously suggested phase separation process, the indentation of each phase was performed. Because the average grain size is small, indentation can influence more than one grain if a large loading is applied. In this case, there may be an additional hardening effect such as the grain boundary etc., and there is a possibility that the hardness of ferrite and bainite phase may be mixed. Figs. 2.5a and 2.5b show the EBSD image with the SPM image at indented areas and the resulting load–displacement curves, respectively. As shown in Fig. 2.5b, part of load-displacement curves for bainite phase were scattered because indentation was performed at low load (maximum load of 1mN), but this compromise was inevitable to obtain the intrinsic property of each phase. The result demonstrates that the identified phases represent different indentation depths and nanohardnesses between the ferrite and bainite phases. The nanohardnesses of the ferrite and bainite phases

are 4.35 ± 0.07 GPa and 5.45 ± 0.58 GPa, respectively, which confirms the validity of the phase identification using the grain average image quality and grain average misorientation. The experimentally obtained load–displacement curves were utilized to determine the parameters in constitutive equation of each constituent phase.

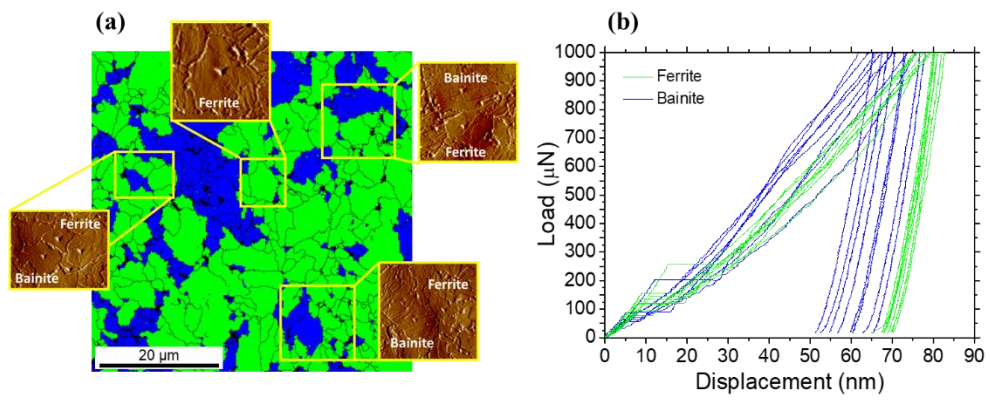


Figure 2.5 (a) The EBSD image with SPM image at indented area and (b) the resulting load–displacement curves.

2.2.4 Hole expansion test

Stretch-flangeability for steel sheets has often been evaluated through tests with hole expansion. For hole expansion experiments, the most popular approaches used in the laboratory are tests using either a flat-bottom punch or a conical punch, as tools for expanding a circular hole. The deformation near the hole edge depends on the geometry adopted. For example, a conical punch induces through-thickness strain gradients at the edge, which results in suppression of the onset of necking. In contrast, the flat-bottom HET with a cylindrical punch involves relatively uniform deformation at the edge, which leads to the initiation of necking at the location away from the hole edge corresponding to the plane strain stress state [9]. For details about the effect of punch geometry on the hole expansion formability, refer to the work by Levy et al. [10], in which the authors observed that the forming limit strain was higher for the test with a conical punch.

In this study, the conical punch with an angle of 60° was used for the HET, and the HER was measured by halting the experiment when the crack propagated completely through the thickness at the hole edge. The deformation of sheet was observed with an aid of image analysis software (auto HER tester, Chongro scientific co. Ltd), and the onset of fracture at the hole edge was determined manually. The final hole diameter was measured right after the onset of hole edge fracture. The initial diameter of the hole was 10 mm, which was fabricated at the center of a rectangular sample sheet with dimension of 120 mm \times 120 mm. The holes are usually manufactured by a punching process that causes micro cracks and dimples near the

shear edges of the holes. However, in this study, the wire cutting method was adopted to prepare for the center hole to eliminate the effect of prior damage in the test. The effect of punched edge condition is out of the scope of the current study. The punch velocity for the HET was 8 mm/min with a sufficiently large holding force to prevent the drawing of the steel sheet.

2.3 Conclusion

In this chapter, the analysis of microstructure and mechanical properties was performed. The investigated steel consist of accicular ferrite and bainite phase. Because both ferrite and bainite phases are same BCC crystal structure, it is difficult to distinguish these phases only using the electron backscatter Kikuchi patterns. Therefore, phase separation was conducted using grain average IQ value and grain average misorientation value. To verify the phase separation result, nanoindentation tests were performed. From the nanoindentation results, the nanohardnesses of the ferrite and bainite phases are 4.35 ± 0.07 GPa and 5.45 ± 0.58 GPa, respectively. This confirms the validity of the identification of each phase using the grain average IQ and grain average misorientation. The microstructure image obtained as a result of phase identification was used in the construction of a representative volume element which will be described in detail in a later section.

To analyze the plastic anisotropy of steel, tensile properties in the RD, DD, and TD directions were measured. Overall, the plastic anisotropy was not remarkable, but the tensile strength was the highest in RD. The measured R-value and yield stress were used to optimize the parameters of the yield function to take into account the plastic anisotropy which also will be explained in a following section.

2.4 References

- [1] S. endo, M. Kurihara, N. Suzuki, A. Kato, M. Yoshikawa, Mater. Jpn., 39 (2000) 167.
- [2] N. Ishikawa, H. Sueyoshi, S. Endo, N. shikanai, Tetsu-to-Hagne, 91 (2005) 809.
- [3] D.H. Kim, S.-J. Kim, S.-H. Kim, A.D. Rollet, K.H. Oh, H.N. Han, Acta Mater., 59 (2011) 5462-5471.
- [4] J.-Y. Kang, D.H. Kim, S.I. Baik, T.-H. Ahn, Y.-W. Kim, H.N. Han, H.-C. Lee, S.H. Han, ISIJ Int., 51 (2011) 130-136.
- [5] X. Li, A. Ramanzani, U. Prahl, W. Bleck, Mater. Chract., 142 (2018) 179-186.
- [6] A.W. Wilson, J.D. Madison, G. Spanos, Scr. Mater., 45 (2001) 1335-1340.
- [7] J. Wu, P.J. Wray, C.I. Garcia, M. Hua, A J. Deardo, ISIJ Int., 45 (2005) 254-262.
- [8] S. Zaefferer, P. Romano, F. Friedel, J. Microsc., 230 (2008) 499-508.
- [9] J.-Y. Lee, K.-J. Lee, M.-G. Lee, T. Kuwabara, F. Barlat, Int. J. Solids. Struct., 156-157 (2019) 107–118.
- [10] B.S. Levy, C.J. Van Tyne, J. Mater. Eng. Perform., 17 (2008) 842–848.

Chapter 3

Dual scale finite element simulation

3.1 Introduction

There are numerous studies on the fracture behavior of metals, which are based on either numerical simulations or experiments. Most of the studies focused on the effect of hydrostatic stress, stress triaxiality, and lode parameters on macroscopically observed ductile fracture [1-2]. The macroscopic approach for modeling the ductile fracture can partially account for the microstructural effect such as plastic anisotropy and the evolution of mathematically formulated void growth etc. However, this approach is challenging when considering detailed effects of microstructure characteristics of the polycrystalline metals on the fracture behavior. The microstructural features to be investigated include the grain size, grain morphology, and plastic deformation inhomogeneity associated to the slip activities. Recently, the crystal plasticity (CP) approach has been efficiently applied to the study on the microstructure effect on both plasticity and ductile fracture [3-4]. Although the CP based FE simulations could reproduce the grain scale plastic inhomogeneity and the resultant ductile fracture response within a reasonable accuracy, significantly increased computational cost by solving the individual slip activities and the interactions among grains remains a challenge when applying the microstructure

based modeling for ductile fracture.

One of the main objectives of the present study is to investigate the effect of microstructure on the fracture of a steel sheet during the hole expansion test. Conventional finite element simulation could be used to estimate the formability and fracture of sheets by employing macroscopic plasticity models, based on a yield function and a strain hardening law, and fracture models. The continuum-based fracture models can be either fully coupled with the plasticity model or an independent criterion [5]. Although this macroscopic approach can marginally consider the effect of microstructure by using anisotropic plasticity, realistic microstructure and local fracture behavior could not be incorporated. As an alternative numerical approach for considering the microstructure and microscale mechanical behavior of metallic materials, the crystal plasticity model has been successfully applied, but its greater computational cost compared with that of the conventional numerical approach is a technical challenge to be overcome for large-scale sheet metal forming.

Therefore, a more practical dual-scale approach is proposed in this study for reducing the computational cost of the microscale simulation based on crystal plasticity, while considering the microstructure effect during the HET efficiently. The proposed dual-scale numerical method forms a bridge between the macroscale hole expansion simulation and the microstructure-based RVE finite element simulation. The output of the macroscale simulation is mainly the deformation paths during the uniaxial tensile test and HET, which will be used in the microscale RVE simulations.

The material parameters for the macroscale simulation were determined by best-fitting the uniaxial tensile stress–strain curve and the same parameters were used for the macroscopic HET. For the microscale simulation, a realistic microstructure-based RVE was constructed.

The microscopic model is based on the dislocation-density-based constitutive law. In each grain, the dislocation density is non-uniformly distributed, considering the pile-ups of dislocations near the grain boundaries. For the simplification of the modeling of dislocation pile-ups and their non-uniform distribution in the grain interior, the dislocation density is assumed to be a function of distance from the grain boundary. As the nodal coordinates are not passed into the UMAT of ABAQUS software employed in this study, they are calculated using the deformation gradients of the adjacent integration points. The procedure is summarized as follows. The grain boundary nodes are extracted in the original configuration. Subsequently, the deformation gradient of the nearest element to each boundary node is used to track the moving direction of the grain boundary. The updated nodal coordinates are used for calculating the dislocation density. The material parameters for the dislocation-density-based hardening model are optimized through the best-fitting of the true strain–true stress curve using deformation history obtained from the macroscale simulation of the uniaxial tensile test. The HER is predicted using the two-scale model with proper introduction of failure criterion only in the microscale level. The critical values for the fracture models are determined from the microscale simulations using the deformation history obtained from the macroscopic simulation

of the uniaxial tensile test. The identification procedures are detailed in Chapter 3.4. The overall procedure of the proposed dual-phase simulation approach is schematically shown as a flowchart in Fig. 3.1. The details of the main idea of the dual-scale simulation approach are presented in the authors' previous work [6]. All the simulations were conducted using the implicit FE software ABAQUS/Standard, except the macroscale nanoindentation simulations, which were performed using ABAQUS/Explicit to avoid divergence issues by abrupt contact changes in the implicit code. In the macroscale simulation, the deformation history of a material point of interested region is extracted. The temporal deformation is set as boundary conditions for the microscale simulation. From this approach, the microscale model parameters are identified by simulating the uniaxial tensile test at macroscale level. In this study, additional nanoindentation simulations were performed to predict the flow stress of constituent phases in ferrite bainite steel. Finally, the macroscale hole expansion test was simulated, from which the deformation history at the edge of the hole was obtained and used for the inputs of the microscale simulation.

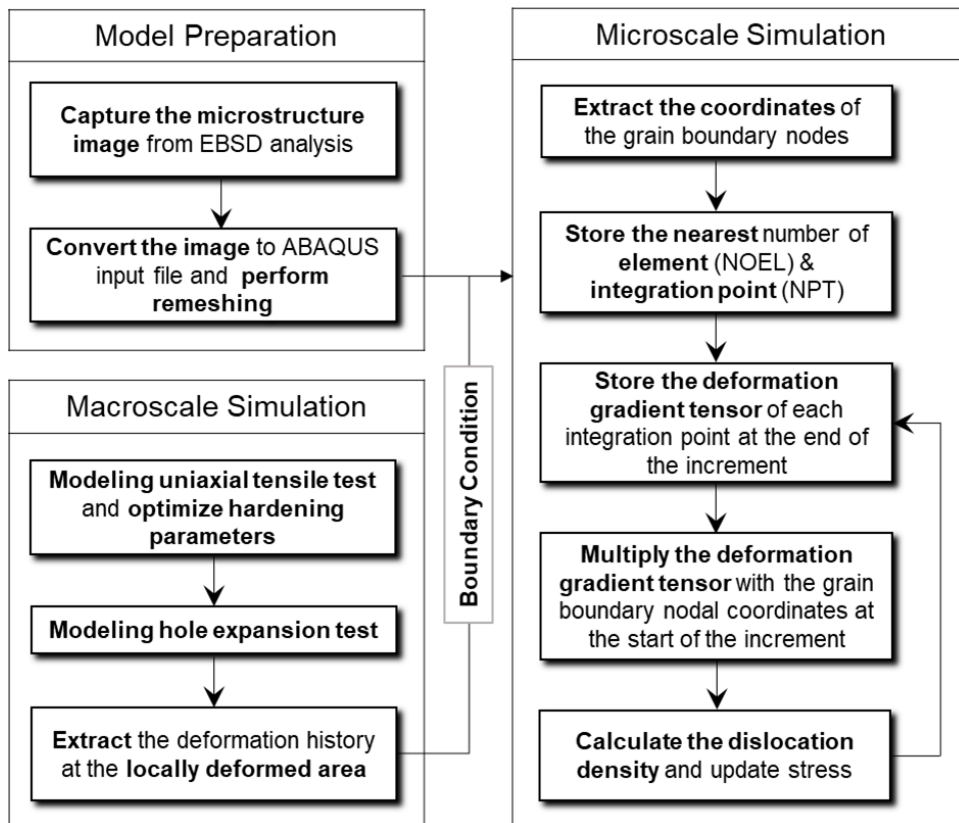


Figure 3.1 Flowchart of dual-scale simulation.

3.2 Macroscale simulation

3.2.1 Uniaxial tensile test

A simple uniaxial tension simulation was performed through the conventional continuum-based finite element method using an isotropic elasto-plastic constitutive model. Considering the anisotropy in yield strength and R-value of the sheet, plastic anisotropy was modeled by using the Hill1948 yield function (Hill, 1948). The yield criterion is expressed as

$$F(\sigma_{xx} - \sigma_{zz})^2 + G(\sigma_{zz} - \sigma_{yy})^2 + H(\sigma_{yy} - \sigma_{xx})^2 + 2(L\tau_{yz}^2 + M\tau_{zx}^2 + N\tau_{xy}^2) = \bar{\sigma}^2 \quad (1)$$

where σ_{xx} , σ_{yy} , σ_{zz} , τ_{xy} , τ_{yz} , and τ_{zx} are the components of the Cauchy stress tensor; F, G, H, L, M, and N are anisotropic coefficients; and $\bar{\sigma}$ is the equivalent stress. For the sheet metals, x and y refer to the RD and TD, respectively. The anisotropy coefficients of the Hill1948 yield function were identified using the R-values and the yield stresses obtained from the uniaxial tensile tests along three different directions (RD, DD, and TD). Since each of the stress–strain curves showed yield point phenomenon, the yield stress value was redefined using 0.2% offset strain by fitting the curve and ignoring the yield point phenomenon. Besides the standard uniaxial tensile test, the notched tensile tests simulations were carried out to consider the effect of stress triaxiality on fracture.

The measured stress–strain curve of ferrite bainite steel was optimized with the mixed Swift-Voce Law as follows.

$$\bar{\sigma} = \alpha \bar{\sigma}_{Swift}(\bar{\varepsilon}_p) + (1 - \alpha) \bar{\sigma}_{Voce}(\bar{\varepsilon}_p) \quad (2)$$

$$\bar{\sigma}_{Swift}(\bar{\varepsilon}_p) = k_1 (\bar{\varepsilon}_0 + \bar{\varepsilon}_p)^n \quad (3)$$

$$\bar{\sigma}_{Voce}(\bar{\varepsilon}_p) = k_2 + Q(1 - \exp(-\beta \bar{\varepsilon}_p)) \quad (4)$$

where α , k_1 , ε_0 , n , k_2 , Q , and β are material constants. The plastic properties were obtained from uniaxial tensile tests and for the elastic properties, linear isotropic elasticity was assumed. The Young's modulus (E) and Poisson's ratio (ν) are 209 GPa and 0.3, respectively. fracture.

To identify the mixed Swift-Voce law and to calculate the strain history before the onset of fracture, the engineering stress–strain curve along RD was used. Because the deformation after necking is dependent on the size of mesh, preliminary simulations were conducted until the optimal size of mesh with no significant difference from the simulation results using smaller sized elements was determined. In addition to the standard uniaxial tensile test, the notched tensile tests simulations were performed to account for the effect of local stress triaxiality on fracture. The optimized material parameters for mixed Swift-Voce model are listed in Table 3.1 and the simulated load–displacement curves for both smooth and notched tensile tests are shown in Fig. 2.4.

The stress–strain curves for the three directions (RD, TD, and DD) are shown in Fig. 3.2a. The stress–strain curves along TD and DD indicate the yield point phenomena; however, it disappears in the curve along RD. These typical changes in the yield point of skin passed low carbon steel resulted from the rolling process,

which lowered the upper yield point and diminished the plateau elongation [7]. The material investigated in this study is a hot rolled steel, and exhibited marginal anisotropy in both yield stress and R-value as shown in Table 2.2. For moderately pronounced anisotropic metals, the Hill yield function has been widely used within reasonable accuracy for describing anisotropy. For example, Choi et al. [8] analyzed void formation and crack propagation from a finite element simulation of hole expansion test using Hill1948 yield function on hot-rolled 590 FB steel with experimental validation. Therefore, in this study Hill1948 yield function was used for simplicity. The anisotropy coefficients of the Hill1948 yield function were determined from the R-value and yield stresses obtained from uniaxial tensile tests [9]. The identified material parameters for the Hill1948 are listed in Table 3.2. The simulated stress–strain curves using identified Hill1948 parameters along RD, TD, and DD are compared with experimental curves in Figs. 3.2b to 3.2d. For comparison, the isotropic case was superimposed. It can be observed from the simulation results that for the TD and DD, the stress–strain behavior is more similar to the experimental results until necking when the Hill 1948 yield function is employed. However, after necking for DD, it was confirmed that the simulation curve matched better with the experimental one when the isotropic plastic yielding is assumed.

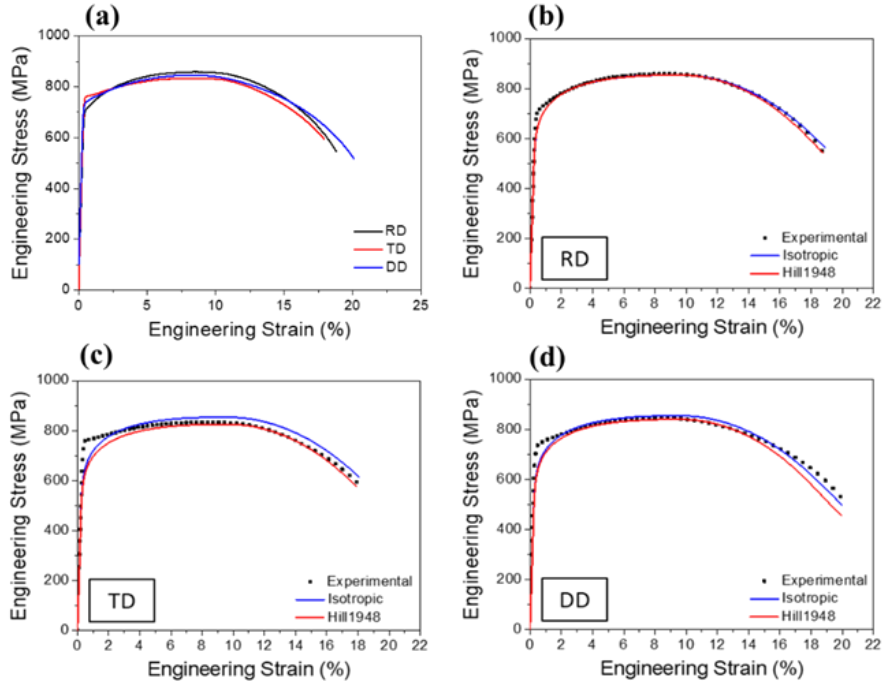


Figure 3.2 Results of experimental and simulated stress–strain curves: (a) Experimental stress–strain curves along RD, TD, and DD; (b)-(d) the experimental stress–strain curve (dot) and curves simulated using Hill1948 yield function (red line) and isotropic yield function (blue line) along RD, TD, and DD.

Table 3.1 Optimized material parameters for mixed Swift-Voce model (Eqs. (2) - (4)).

	α	k_1	ϵ_0	n	k_2	Q	β
FB Steel (Overall)	0.75	1205.8	3.4×10^{-09}	0.1122	785	200	38.7
Ferrite phase	0.82	1215.3	8.437×10^{-09}	0.1232	803	212	32.6
Bainite phase	0.52	1425.1	2.152×10^{-09}	0.1134	924	131	35.8

Table 3.2 Identified material parameters for the Hill1948 (Eq. (1)).

F	G	H	$L=M$	N
0.6154	0.5511	0.4489	1.5	1.4796

3.2.2 Nanoindentation

The investigated steel consists of ferrite and bainite phases. Extensive studies have been performed on the prediction of microstructure of constituent phases based on chemical compositions and process conditions. However, there are limited studies on the direct identification method for the mechanical properties of constituent phases. The analysis of the mechanical properties of each phase has been often conducted by two approaches: direct measurement and indirect prediction. Considering measurement for the mechanical properties directly from experiments, the micropillar tests on single phases have been proposed. However, the test involves a non-uniaxial deformation mode by bulged shape (due to friction) or fracture at large strain. Moreover, a large number of tests might be required because it may exhibit different stress–strain responses depending on crystal orientations. Another direct method is to fabricate single phase microstructure using heat treatment, and to test directly on the sample. Ishikawa et al. [10] employed this method to identify the mechanical properties of ferrite and bainite single phase steel. However, since the chemical compositions of constituent phases in the investigated steel and those of fabricated single phase steels are not identical owing to the different process conditions, the mechanical properties of the constituent phases of ferrite-bainite steel are not necessarily the identical. The flow stresses of multi-phase steels can be predicted using theoretical models. Scott et al. [11] used an original mean field model to quantify the flow behavior of DP steels based on the microstructural parameters. Tomota et al. [12] calculated stress–strain curves of dual phase steels from a

micromechanical approach considering the Eshelby's inclusion theory [13], the Mori-Tanaka's mean field concept [14], and plastic flow rule. Seok et al. [15] predicted the stress strain behaviors of two-phase steel from nanoindentation data measured using two spherical indenter tip with different radii and compared the results predicted by the isostrain method and the non-isostrain method. However, in this numerical approach, there is a limitation that certain assumptions cannot be avoided for the level of strain imposed on each phase.

In this study, nanoindentation simulations were conducted to investigate the stress-strain behavior of each constituent phase. Similarly to the macroscale uniaxial tensile simulation, the mixed Swift-Voce hardening law was applied to the simulations, and their model parameters were optimized by comparing the resultant load-displacement curves to those of experiments. Fig. 3.3 shows the FE model for the macroscale nanoindentation simulation. For the boundary conditions, the indenter tip first moved linearly for 5 s up to the load of 1 mN, followed by unloading down to 0 N in 5 s. The friction coefficient was assumed as 0.2 for contact between the specimen and the tip. Since the deformation by the indentation is considerably local, the deformation on other faces is insignificant. The stress-strain behavior of ferrite and bainite phase can be obtained from the hardening parameters of each phase obtained through the macroscale nanoindentation simulations. The indentation simulations were repeatedly performed until the results were well matched to the experimental data, which are shown in Figs. 3.4a and 3.4b for ferrite phase and bainite phase, respectively. In Table 3.1, the optimized material parameters used in

Figs. 3.4a and 3.4b are listed. Through the optimized material parameters, the stress–strain curves of the ferrite and bainite phases can be obtained as shown in the green and blue dots in Fig. 3.4c. The obtained stress–strain curves of each phase were used in the optimization process of microscale model parameters that will be introduced in detail in the next section.

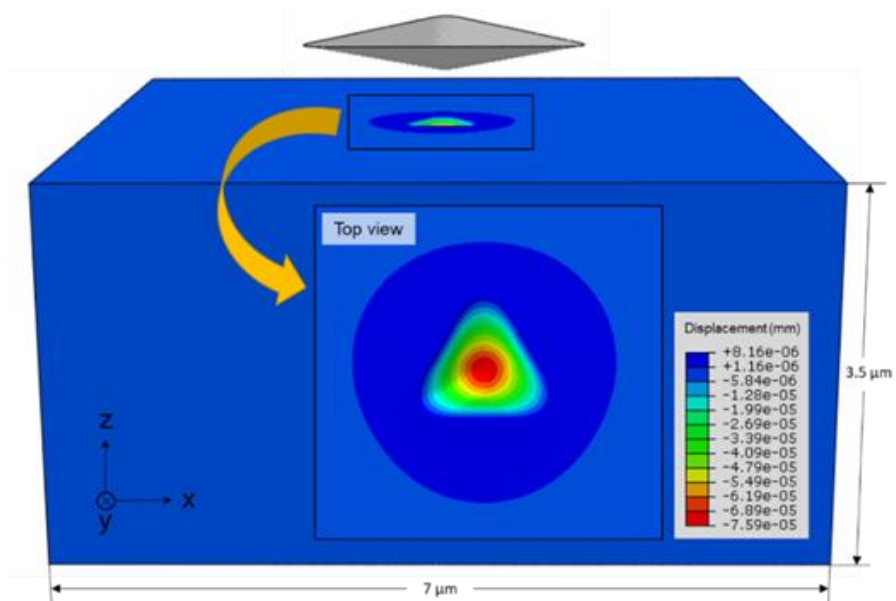


Figure 3.3 The finite element model for macroscale simulation of nanoindentation.

Contour map shows the displacement along z-direction.

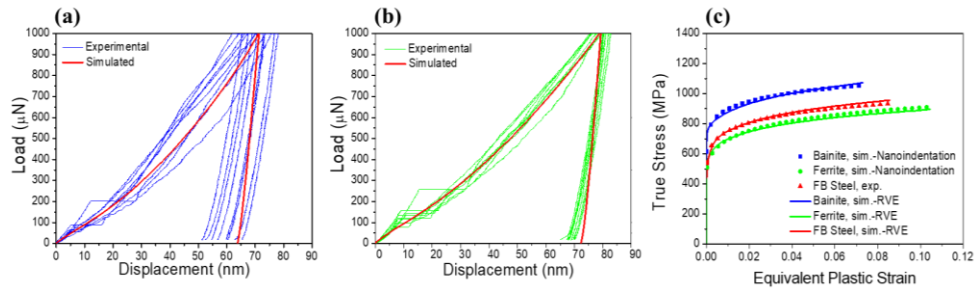


Figure 3.4 The experimental and simulated load–displacement curves for each phase and the resulting stress–strain curves. (a) Bainite phase, (b) ferrite phase, and (c) stress–strain curves for the investigated steel and constituent phases. The dotted curves are obtained from uniaxial tensile test for the investigated steel and macroscale nanoindentation simulation for each constituent phase. The solid lines correspond to the results of microscale RVE simulation.

3.2.3 Hole expansion test

Hole expansion simulations were performed using elastoplastic constitutive model considering anisotropic plastic yield function, Hill1948 as in the simulations of uniaxial tensile tests. Fig. 3.5a represents the schematic image of the hole expansion test model. For a steel sheet, the fully integrated linear brick elements (C3D8) were used, whereas rigid analytical surfaces were used for upper and lower holder; tip. The tip radius was 50 mm and the angle was 60° . The friction coefficient was set to 0.1 for contacts between the blank sheet and tools. The FE model used a quarter of the geometry considering the symmetry. Finer meshes were applied near the edge of hole for more precise analysis (Fig. 3.5b). The hole expansion simulation was conducted using a static implicit user subroutine code, ABAUQS/Standard with rate-independent constitutive equation, which means the velocity of tip does not affect the results of simulation.

The deformation histories at the edge of hole are extracted from macroscale simulation of the hole expansion test. The principal strains are used as boundary conditions for the microscale RVE model. Besides the HER that corresponds to the onset of fracture at the hole edge, the location of the initial fracture is predicted by investigating the deformation histories of the nine selected spots. The spots are the three locations through the thickness in the RD, DD, and TD, which are indicated in Fig. 3.6a. The principal strains of the nine spots are presented in Figs. 3.6b to 3.6j.

The macroscopic simulation results of hole expansion test can be validated by comparing the experimentally measured thickness strains near the hole edge with

those obtained from the FE simulation [16-17]. In this study, the thickness strains along the radial direction at three orientations RD, DD and TD are compared. Fig. 3.7 shows the comparisons between experiment and FE simulations based on Hill1948 and von Mises yield functions. For the Hill1948 model, the anisotropic coefficients were identified based on either R-value (Hill1948R) or yield stress (Hill1948S). In general, all three yield functions could well reproduce the thickness distributions at three sheet orientations, but more accurate predictions were achieved by the Hill1948S at the hole edges in the RD and TD (Fig. 3.7 (a) and (c)). In DD orientation, the three yield functions presented marginally similar accuracy for the predicted thickness strains (Fig. 3.7(b)). Based on this analysis, it is confirmed that the Hill 1948 yield function identified from yield stresses can be appropriate for the macroscopic simulation of hole expansion test.

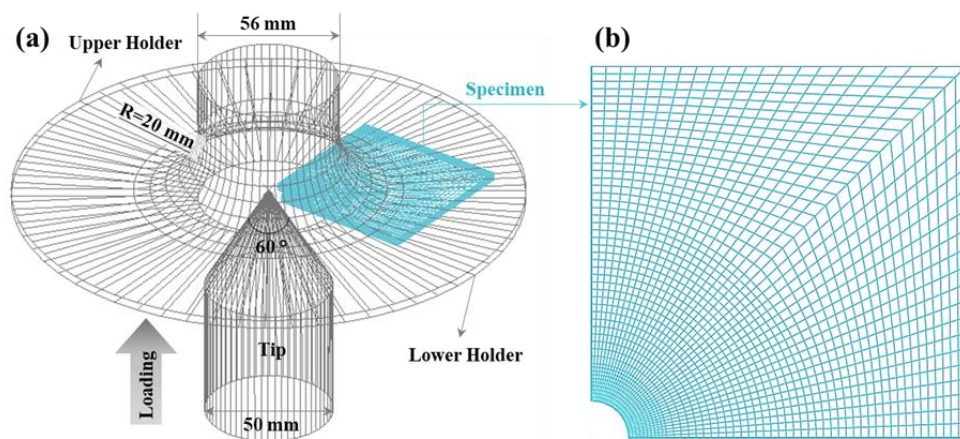


Figure 3.5 Schematic representation of the HET and (b) mesh configuration of the specimen.

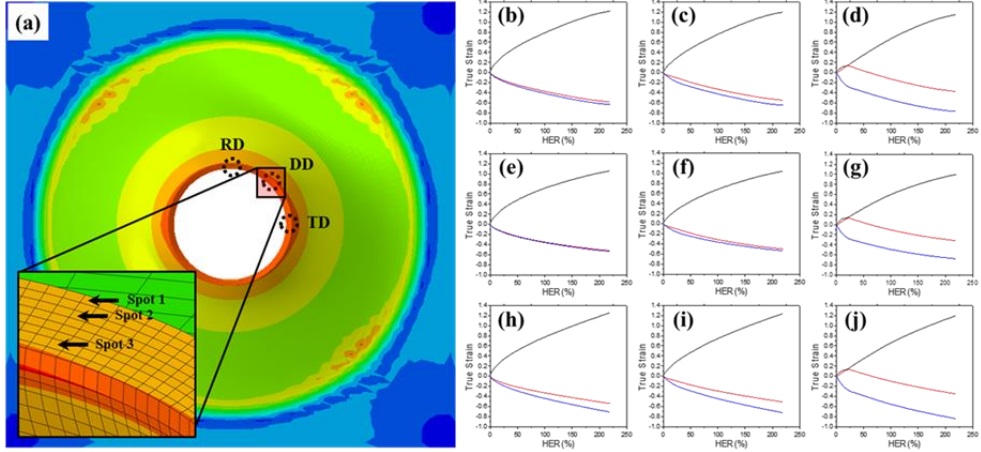


Figure 3.6 Deformed mesh after the hole expansion test simulation (Contour map of effective stress) and true strain versus HER for various spots. (a) Contour map of Mises stress during the hole expansion test indicating the extraction position of principal strain, (b) ~ (d) principal strains extracted at the RD hole edge along the thickness direction (Spot 1, Spot 2, and Spot 3), (e) ~ (g) principal strains extracted at the DD hole edge along thickness direction (Spot 1, Spot 2, and Spot 3), (h) ~ (j) principal strains extracted at the TD hole edge along thickness direction (Spot 1, Spot 2, and Spot 3). The black, red, and blue lines refer to the maximum, medium, and minimum principal strain, respectively.

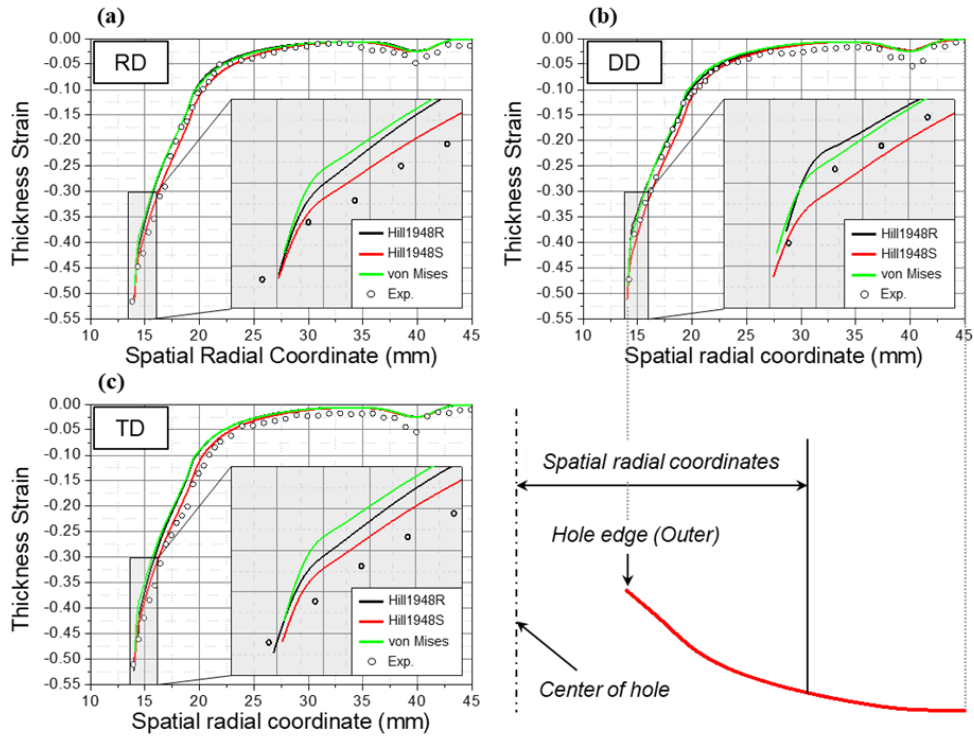


Figure 3.7 (a) Thickness strains along the radial direction at (a) RD, (b) DD, and (c) TD of FB steel. The scale of the magnified graph is from 13.5 to 16 mm on the x-axis and -0.55 to -0.3 on the y-axis, and the major grids are drawn at intervals of 0.5 mm and 0.05, respectively. The details of spatial radial coordinates are schematically shown on the lower right of the figure.

3.3 Microscale simulation

3.3.1 Representative volume elements (RVEs)

The microscale simulations were performed using RVEs generated from microstructure image measured with EBSD. The geometry part was generated from IPF map, which was meshed for the FE analysis. The minimum misorientation angle for grain boundary was set as 5° . The grain sizes of acicular ferrite and bainite phases were obtained as 4.7 ± 2.6 and 3.2 ± 1.9 μm , respectively. For the case of uniaxial deformation mode, there have been many previous studies that successfully predicted fracture of polycrystalline metals using the 3D RVEs having columnar grain structure. Choi et al. [18] successfully simulated the deformation behavior and failure behavior of DP980 steel using quasi-3D RVE (one element in normal direction). In addition, in their follow-up study [8], void formation and micro-crack propagation during the hole expansion tests of 590FB steel were simulated through quasi-3D RVE with validation by experiment. They employed the crystal plasticity finite element models (CPFEM), but the overall impact of the microstructure should be similar as that of our current study. There are other studies based on the CPFEM that introduced the columnar grain structure, instead of realistic microstructure. Lim et al. [19] investigated the effect of grain configuration with CPFEM incorporating the effect of grain boundary. This study also showed no meaningful difference in the mechanical responses, and the local lattice curvature derived from the dislocation density distribution. Moreover, Kim et al. [20] performed FE simulation through 2D RVE of two DP steels with different microstructures, and verified the difference in

hole expansion formability. Achineethongkham et al. [21] used the 2D RVE with GTN models to predict the equivalent fracture strain in stretch-bending tests and the HER values of the specimens subjected to different pre-strains. Their results also confirmed the validity of the 2D RVE scheme by showing good agreement with the experimentally measured results. Based on the previous studies with similar dual-phase steel, it can be seen that the 3D RVE approach with columnar grain structure might be a reasonable assumption for simulating the uniaxial tension and hole expansion models. Therefore, though the thickness of the steel sheet was larger than the grain size, the grain morphology was assumed to be columnar in the z-direction for the simplicity of calculation. The size of RVE was $20\text{ }\mu\text{m} \times 20\text{ }\mu\text{m}$ with a thickness of $0.5\text{ }\mu\text{m}$. Fig. 3.8 shows the microstructure image of the investigated steel and meshes constructed from the EBSD image. The phase identification was carried out by applying the same criteria explained in the previous section using grain average IQ and grain average misorientation. The phase fraction of bainite was measured to be 31%, which is in good agreement with the fraction of 30% derived from the phase identification results. The total number of elements and nodes are approximately 203,000, and 255,000, respectively. The smaller meshes were constructed near grain boundaries for more accurate calculation of local deformation due to dislocation pile-ups.

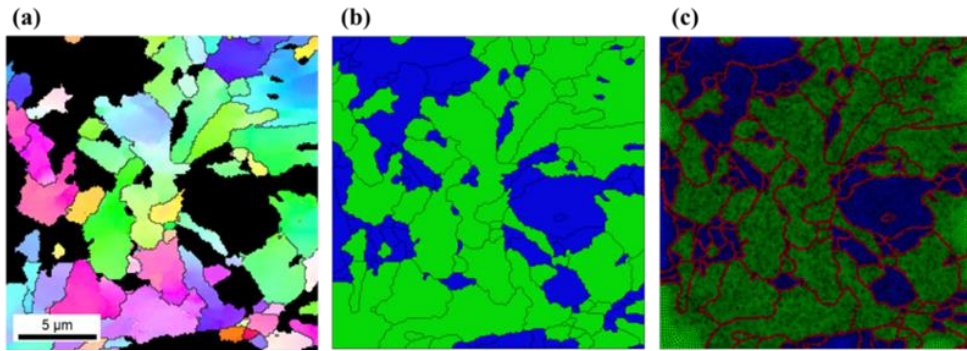


Figure 3.8 RVE constructed from the measured EBSD image. (a) IPF map, (b) geometry part, and (c) mesh constructed for FE simulation.

3.3.2 Constitutive equation

The proposed microscale simulation was performed based on isotropic linear elasticity and isotropic plasticity. For the plasticity, the von Mises yield function and the associated flow rule were adopted. The anisotropy of investigated steel was considered indirectly by applying the deformation path, which was calculated from macroscale simulation considering the Hill1948 yield function, as boundary conditions. Unlike the conventional continuum based simulation, the hardening during plastic deformation is described by the motion of dislocations, which is mathematically expressed as a function of dislocation density, i.e., dislocation density based model. In this study, the modified Kocks–Mecking dislocation density based hardening law was employed [22]:

$$\sigma = \sigma_0 + \alpha \cdot M \cdot \mu \cdot \sqrt{b} \cdot \sqrt{\frac{1 - \exp(-M \cdot k_r \cdot \varepsilon)}{k_r \cdot L_m}} \quad (5)$$

where σ_0 is the term for Peierls stress and solid solution hardening, α is a material constant depending on the dislocation type, M is the Taylor factor, μ is the elastic shear modulus, b is the Burgers vector, k_r is a recovery rate, ε is the equivalent plastic strain, and L_m is the dislocation mean free path. The recovery rates for ferrite and bainite phases are assumed to be a function of the grain size of each phase [23]. The mean free path depends on various obstacles such as grain boundaries, second phase particles, and forest dislocations. However, in this study only dislocation density is considered. Thus, the mean free path is expressed as

$$L_m = A \cdot \sqrt{\frac{1}{\rho}} \quad (6)$$

where A is a material constant, and ρ is the dislocation density. The constant A was introduced in the model as a multiplication factor to take into account the influence of other defects and can be identified by fitting the stress–strain curve calculated using the investigated microscale-level RVE simulations.

The material constant σ_0 was determined as 490 MPa for ferrite and 830 MPa for bainite, which correspond to the yield stress of each stress–strain curve obtained from macroscale nanoindentation simulation. The material parameters in Eq. (5) are listed in Table 3.3.

In the current microscale-level model, the deformation inhomogeneity in the grain is represented by the local accumulation of dislocation density at grain boundaries; or the dislocation pile-up. Unlike the crystal plasticity model where the crystallographic slip activities on individual slip systems are rigorously calculated, the present modeling simplified the effect of dislocation-grain boundary interactions in terms of the 1-dimensional pile-up theory of dislocation. The number of dislocations in unit length, or number density, can be calculated from the solution of the well-known Peach–Kohler equation [24]. The equation is written as

$$0 = \frac{\mu b}{2\pi(1-\nu)} PV \left(\int_a^D \frac{n(x') dx'}{x-x'} \right) + \sigma_A \quad (7)$$

where PV denotes the principal value of the integral, ν is the Poisson's ratio, D is the length between dislocation source and grain boundary, and σ_A is the averaged

resolved shear stress. For simplicity, D is approximated as the half size of average grain diameter. Thus, Eq. (6) results in the following number density $n(x)$ at a local coordinate x measured from the grain boundary toward the grain interior in the orthogonal direction.

$$n(x) = \frac{2\sigma_A(1-\nu)}{\mu b} \cdot \sqrt{\frac{(x-\beta)}{D-x}} \quad (8)$$

In the above equation, β is the length of dislocation pile-up, which is expressed as follows.

$$\beta = \left(\frac{\sigma_c}{\sigma_A} \right)^2 \cdot D \quad (9)$$

where σ_c is the source activation stress shown below.

$$\sigma_c = \frac{0.3\mu b}{\pi L_d} \cdot \ln \left(\frac{L_d}{r_c} \right) \quad (10)$$

where r_c is the dislocation core radius, which is assumed to be 3 times the Burgers vector, and L_d is the length of the dislocation source. The latter value was directly measured from the transmission electron microscopy (TEM) analysis which was used for both ferrite and bainite phases. Fig. 3.9 shows the two-beam bright-field TEM images at different locations, in which the lengths of dislocation sources for the investigated steel were directly measured. The estimated average length of the dislocation source and the source activation stress calculated from Eq. (10) were 13 nm and 420 MPa, respectively.

The dislocation density used for the calculation of mean free path in Eq. (6) is the areal density (or the total length of dislocation line per unit volume), whereas the density calculated in Eq. (8) is linear density (or number density). To correlate the number density in Eq. (8) with the areal dislocation density representing the total dislocation line per unit volume, a simple equation with a correlation factor p is introduced as follows [25].

$$\rho(x) = \frac{n(x)}{p} \quad (11)$$

The material parameter p can be obtained from optimization of proposed constitutive equation to the experimental stress–strain curve.

It is reported that the dislocation density increased during the plastic deformation does not monotonically increase, but has limit or saturation. This might be similar to the three stage stress–strain curve of single crystal. The saturated hardening originates from the cross slips of dislocations that glide on multiple slip systems. For polycrystalline metals, Adachi et al. [26] measured the change in dislocation density under uniaxial tension for specimens with ultra-fine grain, fine grain, and coarse grain using an in-situ x-ray diffraction technique. They found that there were saturated evolutions of dislocation densities at large strain. Therefore, in this study, this phenomenon is incorporated into the hardening relationship between stress and dislocation density. The resolved shear (flow) stress at microscale can be related to the dislocation density as following equation [27], in which the macroscopic stress can be expressed with the resolved shear stress.

$$\sigma_{Taylor} = \sqrt{3}\tau \quad (12)$$

Then, the shear stress in turn can be a function of dislocation density with specific microstructure parameters

$$\tau = \alpha\mu b\sqrt{\rho} \quad (13)$$

where α is a material constant between 0.2 and 0.4, μ is the shear modulus, b is the magnitude of Burgers vector, ρ is the dislocation density. Based on the two equations above, the maximum admissible dislocation density ρ_{crit} corresponding to the initial flow stress is expressed as [25],

$$\rho_{crit} = \left(\frac{1}{\sqrt{3}\alpha b} \frac{\sigma_{y0}}{\mu} \right)^2 \quad (15)$$

The maximum dislocation density was used in the calculation, thus the dislocation density cannot increase beyond the calculated critical dislocation density.

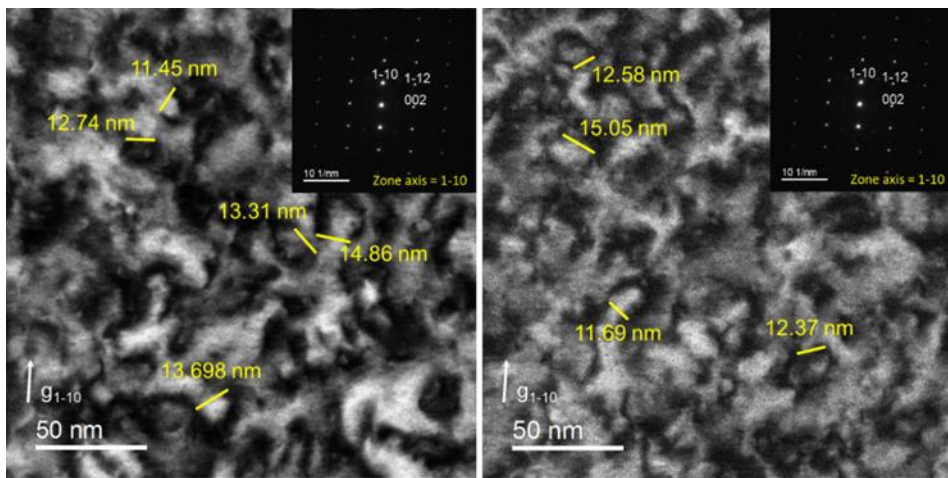


Figure 3.9 Two-beam bright-field TEM images showing the dislocation source length of the investigated steel.

Table 3.3 Material constants for the dislocation based hardening model in Eq. (5) [28].

α	M	μ (GPa)	b (m)	k_r (Unitless)
0.33	3	80	2.5×10^{-10}	$10^{-5}/d$ (d, grain size)

3.3.3 Microscale parameter identification

The dislocation density based microscale model used in this study has two undetermined parameters A and p for each phase. These parameters were optimized from the microscale simulations of uniaxial tensile tests. Thus, principal strains at locally deformed regions of macroscale simulations of uniaxial tensile tests were extracted. The principal strains were imposed as the boundary conditions in RVE model. The schematic 3D RVE image and its face labels are presented in Fig. 3.10a. The boundary conditions imposed on the FE simulation of the uniaxial tensile test and hole expansion test using the microscale RVE model are as follows. All nodes on Face 2, 4, and 6 along three mutually orthogonal coordinates are uniformly displaced along the normal direction of each face by the predefined deformation histories; i.e. maximum, medium, and minimum principal strains. The deformation histories are calculated from the macroscale simulation as shown in Fig. 3.10b. On the other hand, the nodes on Faces 1, 5, and 3 are constrained from moving along their face normal directions.

The parameters of each phase of the microscale model were iteratively determined by fitting the flow curves of ferrite and bainite phases which were obtained from macroscale nanoindentation simulation. The true stress– true strain curves calculated from the microscale simulation show good agreement with those of each phase obtained through nanoindentation simulation, as well as the experimentally measured true stress–true strain curve of investigated steel (Fig. 3.4c). The parameters A and p obtained from the proposed optimization process are listed

in Table 3.4. Figs. 3.11a-c present the contour map of effective stress, dislocation density, and logarithmic strain at the macroscopic strain of 2 %. Note that the present model can capture the dislocation pile-up at the grain boundaries and the strain is concentrated in the soft ferrite phase.

To validate the proposed two-level FE simulations, the geometrically necessary dislocation (GND) of investigated dual-phase steel was calculated from the measured local misorientations. The calculation of GND was based on the Nye's dislocation density tensor, in which the maximum misorientation was set as 5° . The GND density was assumed null wherever the measured misorientation between adjacent points exceeds this maximum misorientation as suggested by Field et al. [30]. Fig. 3.12 shows the contour maps of dislocation densities calculated from the present FE simulation and the distributions of GND obtained from EBSD measured at 4 % and 6 % strains. In the FE simulations, the dislocation density reached the aforementioned maximum dislocation density in the case of bainite phase and the same dislocation density is shown in the whole grains (Fig. 3.11b). Similarly, it was confirmed that the GNDs calculated from the EBSD data also showed almost uniform distribution of dislocation densities in the grains of the bainite phase (Fig. 3.12d and Fig. 3.12e). Also, it is observed that the dislocation pile-ups at grain boundaries are featured in case of ferrite phase, which is similar to the simulation results. Moreover, it can be also confirmed that the degree of pile-ups increases as the strain increases. Note that because the calculated dislocations from the EBSD measurement represent only GND component (not the total dislocation density), the

quantitative comparison is not feasible. But, the above analysis can validate the predictive ability for local hardening at grain boundary area and the distribution of dislocation densities within the investigated microstructures of dual-phase steel.

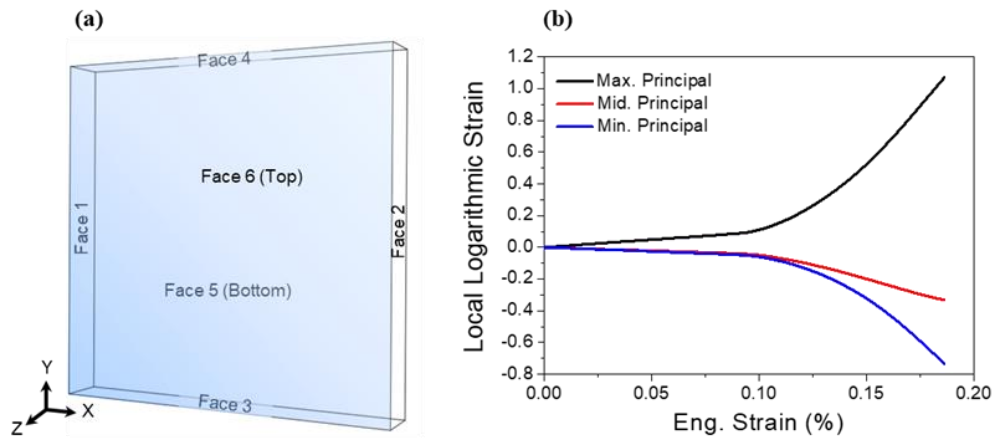


Figure 3.10 (a) Schematic image of 3D RVE and (b) strain histories obtained from the macroscale simulation.

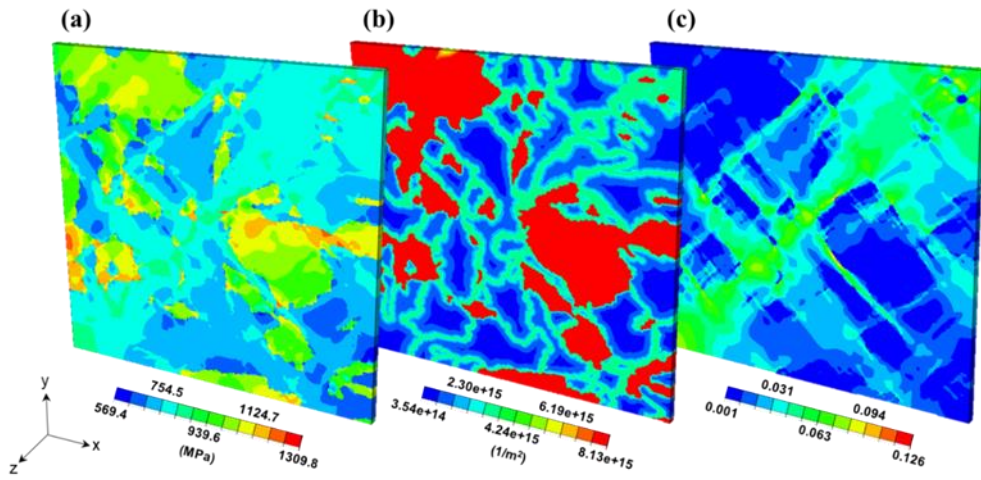


Figure 3.11 Contour map of (a) effective stress (MPa), (b) dislocation density ($1/m^2$), and (c) logarithmic strain under the macroscopic strain of 0.02.

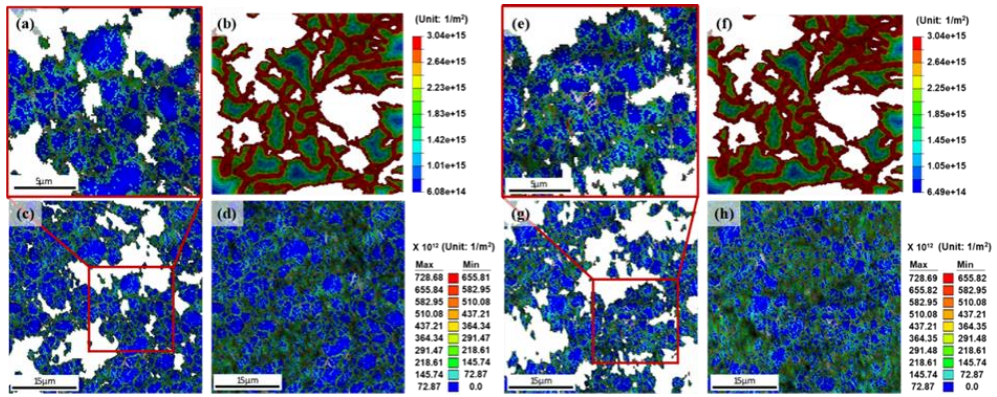


Figure 3.12 Distributions of dislocation density at strain 4 % (a-d), and 6 % (e-h). The FE simulated dislocation densities (b, f), the geometrically necessary dislocation densities for dual-phase (d, h), and for only ferrite phase (c, g) were calculated from the measured local misorientation. The enlarged images (a, e) show the same scale of microstructure as RVE model.

Table 3.4 Optimized parameters used for the microscale model (Eqs. (6), (11)).

Ferrite		Bainite	
A	p	A	p
192	1.04×10^{-7}	183	1.09×10^{-8}

3.3.4 Fracture criterion using local stress triaxiality

For fracture analysis in the hole expansion process, numerous studies have been performed to understand the relationship between the microstructure of materials and their ductile fracture behaviors. Simple empirical observations from the uniaxial tensile ductility and microstructure of advanced high-strength steels have shown that the hole expansion properties are improved by lowering the strength differential between soft and hard phases. Furthermore, from Hasegawa [30] and Fang's [31] work, the interface crack propagation has been found to be the main source of fracture in the hole expansion process for multiphase steels. Comprehensive numerical simulations by introducing damage or ductile failure models were also performed to analyze the stretch-flange formability of metal sheets quantitatively. Approaches based on forming limit diagram [32], Gurson [33] and Tvergaard's [34] coupled plasticity-damage models based on void growth and coalescence, and Johnson's ductile fracture criteria [35] considering stress triaxiality have been widely used to estimate the hole expansion formability of various materials including lightweight alloys and multiphase advanced high-strength steels.

The analyses based on continuum plasticity and damage or fracture models have provided reasonably good performances in predicting failed locations, thickness distributions around the hole edge, and through-thickness failure propagation [36, 37], with marginal consideration of the microstructure characteristics in terms of anisotropy and stress state dependent failure behavior. Other ductile damage models have been proposed for predicting fracture strains with more sophisticated

approaches. For example, Bai et al. [39] suggested a modified form of the Mohr–Coulomb fracture model for describing the ductile fracture of materials as a function of stress triaxiality and Lode parameters. Dunand and Mohr [39] proposed the Hosford–Coulomb fracture model from the analysis of a 3-D unit cell under proportional loading. This model linearly combines the Hosford effective stress and normal stress acting on the maximum shear plane and critical fracture strain is assumed when it exceeds a critical value [40]. These phenomenological ductile fracture models could accurately predict the onset of fracture for various ductile metals in many practical engineering applications.

Investigations on the effect of a local microstructure on stretch-flange formability have shown that the HERs can be distinctive even when the macroscopic mechanical properties are similar. For instance, two dual-phase steels with different ferrite-martensite structures but with almost the same strength and ductility in the uniaxial tensile test presented considerably different HERs [30]. Therefore, conventional phenomenological fracture models, which do not consider the details of microstructure, might not be appropriate for a comprehensive understanding of the deformation and failure of the hole expansion process. Alternatively, Ramazani [41] and Kim [20] proposed a micromechanics-based model considering the microscopic inhomogeneity of materials to simulate the hole expansion formability of lightweight alloys and multiphase steels. They used a representative volume element (RVE) [42] or a realistic microstructure directly obtained from microscopic images [43], in which the stretch-flange formability could be well related with the

morphology and strength of each constituent phase. A more physical approach for considering the effect of microstructure on plastic deformation, which is based on the local slip (or twin) activities as a major origin of plastic deformation, is also available, i.e., crystal plasticity. This approach can simulate elastic anisotropy, the evolution of anisotropy during plastic deformation, and local stress states at single and polycrystal levels. However, more material parameters for characterizing the single-crystal properties and grain-level orientation distribution exist. Moreover, this approach requires significant computational cost, and thus cannot be practically used for engineering purposes. For example, Choi et al. [8] investigated the effect of crystallographic orientation and spatial distribution of the constituent phases during the hole expansion test to analyze the relationship between the initial crystallographic orientation and the hot spots for void formation, but the fracture behavior could not be simulated owing to limited computational efficiency. In contrast, the phenomenological damage models, which can reproduce the failure of ductile metals with fewer model parameters, are computationally efficient when they are properly formulated considering the stress states. Despite these advantages, the phenomenological models cannot be used to investigate the direct relationship between the microstructure of ductile metals and their fracture characteristics. They can only include the microstructure effect in an indirect way by introducing the anisotropy in the plasticity model.

Therefore, one of the purposes of the present study is to provide a computational approach that can account for the microstructure effect in a practical way without

using crystal plasticity, while attaining accuracy for evaluating the fracture of ductile metals for engineering applications. A dual-scale finite element approach is proposed to simulate the hole expansion formability of investigated steel sheet. Conventional continuum-based finite element analyses based on the isotropic elasto-plastic constitutive model were implemented mainly for computational efficiency and to simplify the analysis, without weakening the main conclusions of the present study.

In the present study, an uncoupled isotropic ductile fracture model, which neglects the damage effects on the yield surface, is adopted to predict the onset of fracture in the microstructure. The proposed ductile fracture model is a function of the stress triaxiality, which is defined as the ratio of mean stress to the effective stress, $\sigma_m/\bar{\sigma}$. The macroscopically measured stress triaxiality under homogeneous uniaxial tensile deformation is 0.33. However, the stress triaxiality in the microscale-level is inhomogeneously distributed in the microstructure owing to the inhomogeneity of plastic deformation or effective stress through the grains. Therefore, the following model was suggested to include the effect of local stress triaxiality on critical fracture strain.

$$\bar{\varepsilon}_f = B_1 \cdot \exp(-B_2 \cdot \eta_{avg}) + B_3 \quad (16)$$

where $\bar{\varepsilon}_f$ is the equivalent plastic strain at the onset of failure, and B_1 , B_2 , and B_3 are material constants calibrated from the microscale simulation of smooth and notched tensile tests. Like the previous two-scale modeling procedure, the deformation histories were calculated from the macroscale smooth and notched

tensile simulations. The strain histories were applied to the microscale RVE model as boundary conditions. Through the microscale simulation, the averaged stress triaxiality values were calculated by integrating the local stress triaxiality over the equivalent plastic strain.

$$\eta_{avg} = \frac{1}{\bar{\varepsilon}_p} \int_0^{\bar{\varepsilon}_p} \eta d\bar{\varepsilon}_p \quad (17)$$

where $\bar{\varepsilon}_p$ and η are equivalent plastic strain and stress triaxiality, respectively. In order to take this path (or history) effect into account, the stress triaxiality value was introduced based on the equivalent plastic strain increment weighted average of the stress triaxiality to better capture the history of the stress triaxiality in large deformation.

The deformation histories under different stress states were obtained from macroscale simulations of notched tensile tests. These deformation histories were used as boundary conditions for the microscale RVE simulations. Fig. 3.13 shows the contour maps of the effective stress and stress triaxiality in the microstructure under the macroscopic uniaxial tension test at the strain of 0.08. This deformation history corresponds to the stress triaxiality of 0.33 in averaged sense. However, as aforementioned, the figure clearly illustrates that the stress triaxiality locally deviates from 0.33 and the value is very high at the vicinity of deformed phase boundary. Thus, to track the change of stress triaxiality in microscale point of view, the stress triaxiality values at the local point with the maximum equivalent plastic strain when fracture occurs were extracted, and the averaged stress triaxiality value was

calculated from the Eq. (17). Fig. 3.14 shows the relationship between the equivalent plastic strain and averaged stress triaxiality under different stress states. As mentioned above, in each case, since the analysis was performed on the local point where the deformation was concentrated, it was confirmed that the deformation occurred with a value larger than the stress triaxiality value analyzed in macroscale. Based on the calculated values until the onset of fracture, the material constants in Eq. (16) could be obtained and they are listed in Table 3.5.

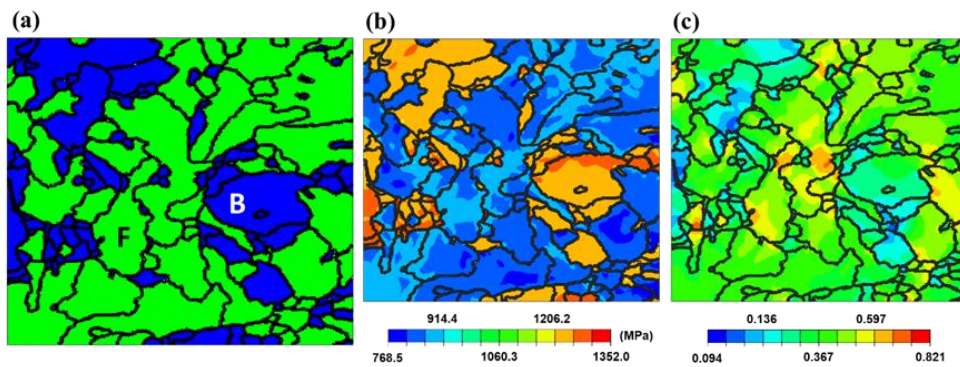


Figure 3.13 (a) Phase map of FB steel and contour map (top view) of (b) effective stress and (c) stress triaxiality. The grain boundary elements are superimposed on each contour map.

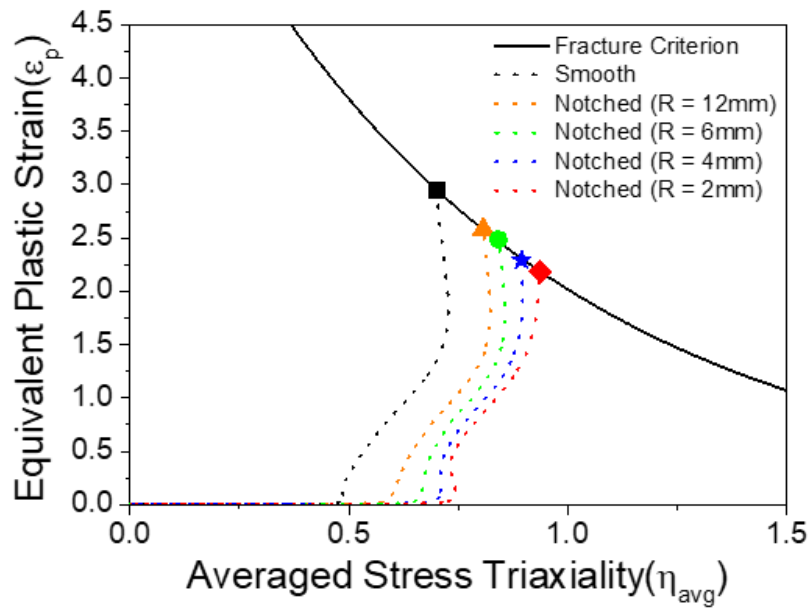


Figure 3.14 Averaged stress triaxiality versus equivalent plastic strain calculated from the microscale simulation of uniaxial tensile tests.

Table 3.5 Material constants for local stress triaxiality fracture model (Eq. (16)).

B_1	B_2	B_3
7.168	1.268	5.103×10^{-5}

3.3.5 Hole expansion test

The evolution of averaged stress triaxiality during hole expansion deformation was calculated from microscale simulation. Fig. 3.15a illustrates the equivalent plastic strains as a function of average stress triaxiality in each spot. Fig. 3.15a indicates that the evolution of the equivalent plastic strains at the spot 3 is different from the other two spots. These distinctive deformation histories can be also observed from Fig. 3.6. This is because spot 3 is located closer to the punch tip than the other two spots. Fig. 3.15a shows that the stress triaxialities of sheet materials at the hole edge region change significantly from low value near uniaxial tension to larger value over 1.0.

From the analysis of plastic deformation histories in different locations (Fig. 3.15a), the dual scale model coupled with the ductile fracture criterion predicted the onset of fracture at the spot 1. Furthermore, it predicted that the earliest fracture occurred along RD, which is consistent with the experimental result as shown in Fig. 3.15b. The predicted HER was 131%, which is similar to the experimentally measured HER of 138% (Fig. 3.16). In Fig. 3.16, the HER is further predicted by assuming isotropic model, which clearly overestimated the experimental value. The results clarify the importance of anisotropy in the macroscale-level simulation to accurately predict the HER.

Fig. 3.17 represents the equivalent plastic strain at the onset of fracture and stress triaxiality at initial deformation (under the hole expansion ratio of 20%) for the spot 1-3 of RD hole edge. From the previous microscale simulation, it was

confirmed that the first fracture occurred at spot 1, and as a result, the smallest deformation appeared in the circumferential direction at the time of fracture. An interesting observation is that the distribution of equivalent plastic strain at fracture is almost the same even if the deformation history at each spot is obviously different. The reason for the earliest fracture at the spot 1 is that it is deformed under high stress triaxiality from at the early stage of deformation where the strain corresponds to the HER of less than 25% (or, where the strain path of spot 3 is significantly different from that of other two spots (Fig.3.6d)) as can be seen in Fig. 3.15a. This observation is also confirmed by comparing the contour maps of stress triaxiality of each spot at the same HER level. Note that the stress triaxiality is quite lower for spot 3 than that of spot 1 and spot 2. The reason why the low stress triaxiality is observed in spot 3 is that a compressive stress is applied when the punch tip and the edge of the hole are in contact at the beginning of the HET. This compressive stress is applied until the contact is removed at the hole edge, which results in the relatively low stress triaxiality of spot 3. From the previous results, in the absence of geometrical imperfection of the hole edge, the crack occurred first at the location farthest from the punch tip (i.e. spot 1) when the HET was performed using a conical tip.

For more discussion, the model presented in this study was compared with the results obtained using only macroscale simulation. In general, fracture occurs with the onset of diffused instability followed by localized necking in the uniaxial tension. In this process, the strain is concentrated in local area, and the equivalent plastic

strain and stress triaxiality increase rapidly. However, only localized necking is involved without noticeable diffuse neck in the hole expansion test [44]. This can be seen in Fig. 3.18, which shows the deformation history calculated through the macroscale simulation of uniaxial tension (Fig. 3.18a) and HET (Fig. 3.18b). For a fracture criterion, the same equation of Eq. 16 was used and its parameters were optimized through macroscale uniaxial tension simulation.

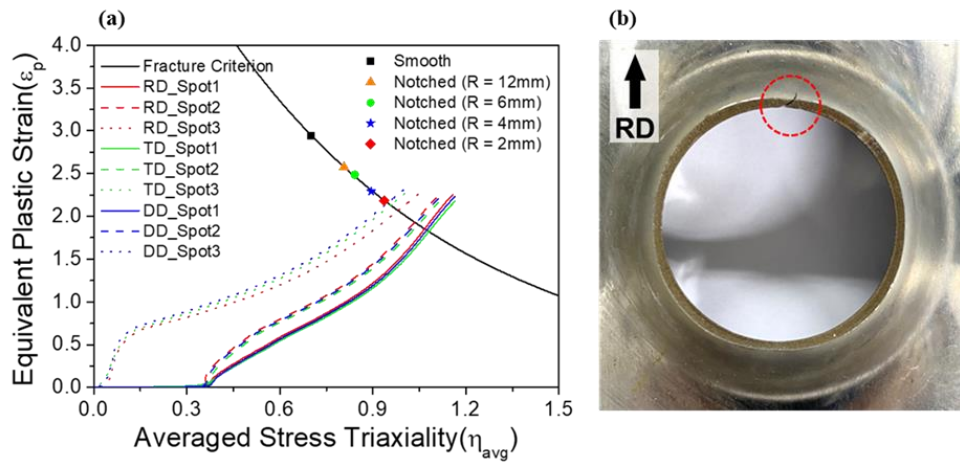


Figure 3.15 (a) Averaged stress triaxiality versus equivalent plastic strain calculated from the microscale simulation of uniaxial tensile tests. (b) The hole edge image after the hole expansion test. The red circle indicates the location of crack initiated during the hole expansion test.

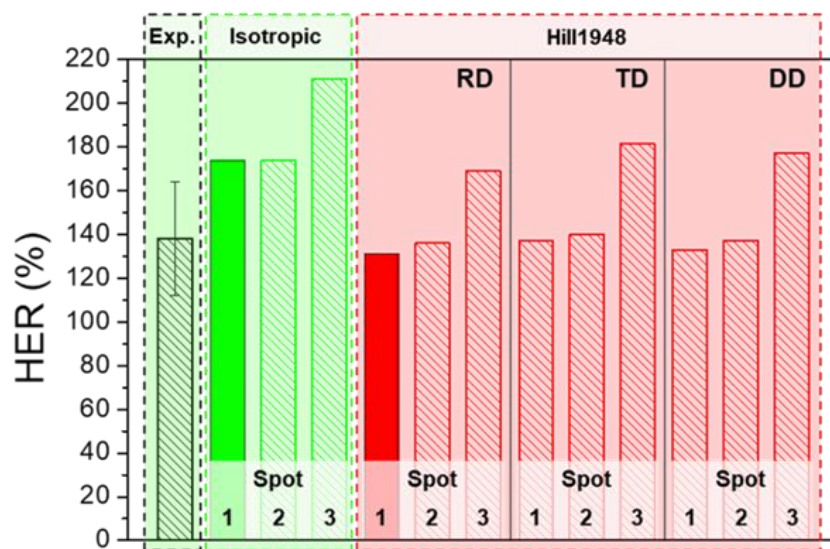


Figure 3.16 Experimental and predicted HER for each position.

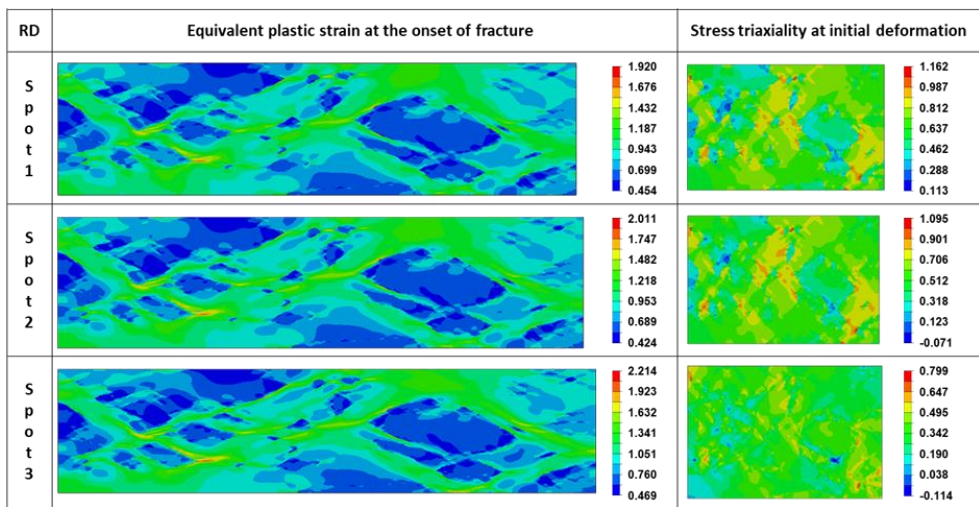


Figure 3.17 Equivalent plastic strain at the onset of fracture and stress triaxiality at initial deformation for the spot 1-3 of RD hole edge.

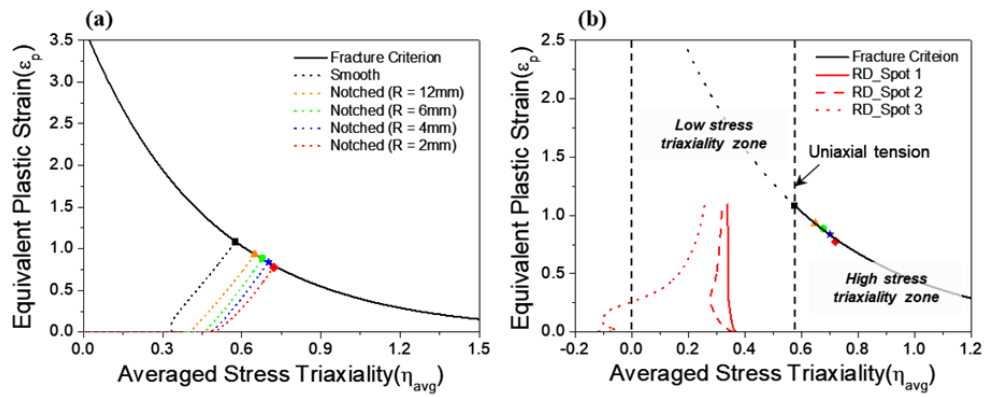


Figure 3.18 (a) Fracture criterion derived from macroscale uniaxial tensile tests and (b) deformation histories for spot 1-3 of RD hole edge calculated from macroscale simulation of hole expansion test.

3.3.6 Dependence of strength difference of constituent phase on HER

In general, HER is known to be affected by the difference in strength of constituent phases. In the case of AHSS, it is often composed of two or more phases such as dual phase (DP) steel and complex phase (CP) steel. Thus, controlling the strength difference of constituent phases is essential to obtain the required properties according to its application. In this study, microscale simulation was performed by deliberately lowering the strength difference of constituent phases in order to investigate the effect of the strength difference of constituent phases on the HER.

Fig. 3. 19a shows the stress–strain behaviors of ferrite and bainite of the investigated FB steel (Cond. 1) and those of when the strength between the two phases is deliberately set small (Cond. 2). Note that the total stress–strain curve is identical for each condition. Fig. 3. 19b shows the fracture criterion obtained through microscale simulation for Cond.1 and Cond. 2. As the strength difference between the phases decreases, the strain localization in the microstructure decreases. Therefore, it can be seen from Fig. 3. 19b that the fracture criterion is shifted toward the equivalent plastic strain with a lower value. The material parameters of local stress triaxiality criterion for Cond. 2 are listed in Table 3.6. Fig. 3. 20 shows the deformation history in RD Spot 1 for Cond.1 and Cond. 2. Likewise, since less strain localization occurs, it can be seen that deformation occurs at a lower equivalent plastic strain level. The predicted HER of Cond. 2 from the microscale simulation result was 143%, which is higher than that of Cond. 1, which means that the higher HER can be obtained with the smaller strength difference of constituent phases.

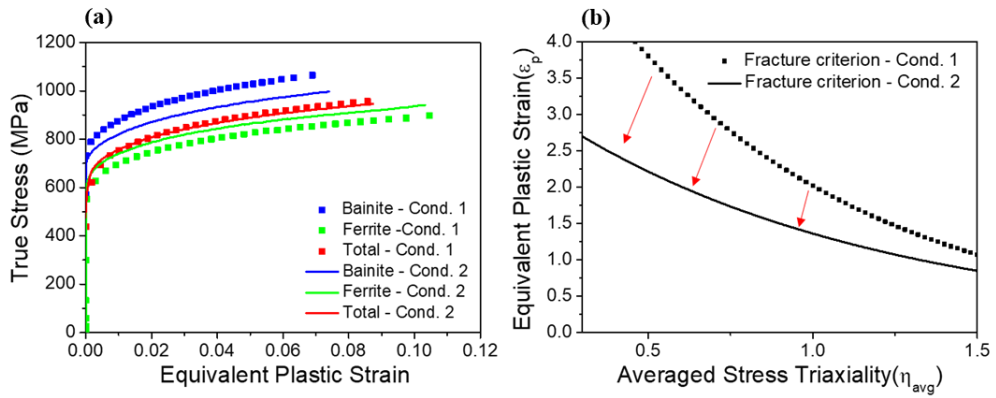


Figure 3.19 (a) The stress–strain behaviors of ferrite and bainite of the investigated FB steel (Cond. 1) and those of when the strength between the two phases is deliberately set small (Cond. 2) and (b) the fracture criterion obtained through microscale simulation for each condition.

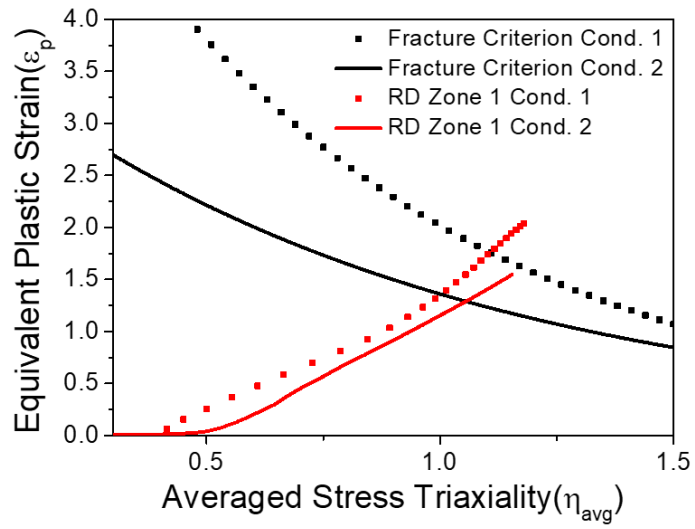


Figure 3.20 (a) The deformation history in RD Spot 1 for Cond.1 and Cond. 2.

Table 3.6 Material constants of local stress triaxiality fracture model for Cond. 2 (Eq. (16)).

B_1	B_2	B_3
3.56	1.016	0.0728

3.4 Conclusion

In this chapter, a new dual-scale simulation was proposed to practically account for the effect of microstructure of two-phase polycrystals on the ductile fracture behavior within the reasonable computational cost compared to the CP counterpart. The dual-scale approach is based on two step simulations consisting of both microscale and macroscale levels. In the macroscale level at the size of $\sim\text{mm}^2$ (or even larger), hole expansion simulation as an example, the strain histories in the interested regions (or material point) were obtained, which were transferred to the boundary conditions of the microscale level simulation. An RVE approach was used for the microscale level simulation, in which the detailed microstructure characteristics in the size of $\sim \mu\text{m}^2$ were provided. In the constitutive models, phenomenological yield function and hardening law were used for the macroscale simulation, whereas the dislocation density based hardening model coupled with the dislocation-grain boundary interaction was used for the microscale simulation.

Regarding the computational aspect, a numerical algorithm was developed to track the change of grain boundaries during the plastic deformation, which can be calculated by the prescribed nodal coordinates of initial grain boundary configuration and the updated deformation gradients of grain boundary elements during the deformation. Besides the plasticity in the hole expansion test, the ductile fracture model was implemented by monitoring the local triaxiality in the microscale simulation. The microscale RVE model coupled with dislocation pile-up formulation can be a practical tool for analyzing the grain boundary hardening and locally

inhomogeneous plastic deformation at the grain scale of the dual-phase ferrite bainite steel. In addition, the distribution of dislocations calculated through the microscale model was verified through experimentally measured EBSD GND data. Therefore, the proposed model can be employed as an alternative to the crystal plasticity approach for understanding the effect of local plastic deformation on fracture behavior without tracing the detailed slip activities of each grain.

The ductile fracture criterion as a function of averaged stress triaxiality was determined in the context of the proposed dual scale simulation. The onset of fracture at the hole edge (or equivalently the hole expansion ratio, HER) during hole expansion test could successfully be predicted by monitoring the local stress triaxialities and equivalent plastic strains in the microstructure RVEs selected from nine different locations. Besides the HER, the location of the initial fracture at the hole edge could be predicted accurately. The predictive ability of the dual-scale simulation for the HER was improved when the anisotropy of the sheet was considered in the macroscale-level simulation. For the isotropic model, the predicted HER was significantly overestimated in the experimental value.

3.5 References

- [1] T. Wierzbicki, Y. Bao, Y.-W. Lee, Y. Bai, *Int. J. Mech. Sci.*, 47 (2005) 719-743.
- [2] L. Xue, T. Wierzbicki, *Eng. Fract. Mech.*, 75 (2008) 3276-3293.
- [3] J. Kadkhodapour, A. Butz, S. Ziaei-Rad, S. Scauder, *Int. J. Plast.*, 27 (2011) 1103-1125.
- [4] D. Gerbig, A. Sivastava, S. Osovski, L. G. Hector, A. Bower, *Int. J. Fract.*, 209 (2018) 3-26.
- [5] K. Wang, L. Greve, T. Wierzbicki, *Int. J. Solids. Struct.*, 71 (2015) 206–218.
- [6] S. Park, J. Jung, K.I. Kim, H. Kim, S.-I. Kim, K.H. Oh, M.-G. Lee, H.N. Han, *Int. J. Mech. Sci.*, 156 (2019) 297-311.
- [7] J. Grassino, M. Vedani, G. Vimercati, G. Zanella, *Int. J. Precis. Eng. Manuf.*, 13 (2012) 2017-2026.
- [8] S.-H. Choi, E.-Y. Kim, S. I. Kim, *Int. J. Plast.*, 58 (2014) 184-200.
- [9] P. Dasappa, K. Inal, R. Mishra, *Int. J. Solids Struct.*, 49 (2012) 3528-3550.
- [10] N. Ishikawa, K. Yasuda, H. Sueyoshi, S. Endo, H. Ikeda, T. Morikawa, K. Higashida, *Acta Mater.*, 97 (2015) 257-268.
- [11] C.P. Scott, B. Shalchi Amirkhiz, I. Pushkareva, F. Fazeli, S. Y. P. Allain, H. Azizi, *Acta Mater.*, 159 (2018) 112-122.
- [12] Y. Tomota, K. Kuroki, T. Mori, I. Tamura, *Mater. Sci. Eng.*, 24 (1976) 85-94.
- [13] J. D. Eshelby, *Proc. Roy. Soc. London Ser. A*, 241 (1957) 376-396.
- [14] T. Mori, K. Tanaka, *Acta Metall.*, 21 (1973) 571-574.
- [15] M.-Y. Seok, Y.-J. Kim, I.-C. Choi, Y. Zhao, J.-I. Jang, *Int. J. Plast.*, 59 (2014)

108-118.

[16] T. Kuwabara, T. Mori, M. Asano, T. Hakoyama, F. Barlat, *Int. J. Plast.*, 93 (2017) 164-186.

[17] J.-Y. Lee, K.-J. Lee, M.-G. Lee, T. Kuwabara, F. Barlat, *Int. J. Solids Struct.*, 156 (2019) 107-118.

[18] S.-H. Choi, E.-Y. Kim, W. Woo, S.H. Han, J.H. Kwak, *Int. J. Plast.*, 45 (2013) 85-102.

[19] H. Lim, M.-G. Lee, J.H. Kim, B.L. Adams, R.H. Wagoner, *Int. J. Plast.*, 27 (2011) 1328-1354.

[20] J.H. Kim, M.-G. Lee, D. Kim, D.K. Matlock, R. Wagoner, *Mater. Sci. Eng. A* 527(27-28) (2010) 7353-7363.

[21] K. Achineethongkham, V. Uthaisangsuk, *Int. J. Mech. Sci.*, 183 (2020) 105828.

[22] R. Rodriguez, I. Gutierrez, *Mater. Sci. Forum*, 426 (2003) 4525-4530.

[23] S.K. Basantia, A. Bhattacharya, N. Khitai, D. Das, *Met. Mater. Int.*, (2019) 1-19

[24] L.H. Friedman, D.C. Chrzan, *Philos. Mag. A*, 77 (1998) 1185-1204.

[25] S. Brincmann, T. Siegmund, Y. Huang, *Int. J. Plast.* 22 (2006) 1784-1797.

[26] H. Adachi, Y. Miyajima, M. Sato, N. Tsuji, *Mater. Trans.* 56 (2015) 671-678.

[27] M.F. Ahsby, *Philos. Mag.*, 21 (1970) 399-424.

[28] S.K. Paul, A. Kumar, *Comput. Mater. Sci.*, 63 (2012) 66-74.

[29] D. P. Field, P. B. Trivedi, S. I. Wright, M. Kumar, *Ultramicroscopy*, 103 (2005) 33-39.

- [30] K. Hasegawa, K. Kawamura, T. Urabe, Y. Hosoya, *ISIJ Int.*, 44 (2004) 603-609.
- [31] X. Fang, Z. Fan, B. Ralph, P. Evans, R. Underhill, *J. Mater. Sci.*, 38 (2003) 1297-1319.
- [32] W. Kim, Y. Koh, H. Kim, Y.I. Chung, M.-G. Lee, K. Chung, *Met. Mater. Int.*, 23 (2017) 519-531.
- [33] A.L. Gurson, *J. Eng. Mater. Technol.*, 99 (1977) 2-15.
- [34] V. Tvergaard, *Int. J. Fract.*, 18 (1982) 237-252.
- [35] G.R. Johnson, W.H. Cook, *Eng. Fract. Mech.*, 21 (1985) 31-48.
- [36] L. Xu, F. Barlat, M.-G. Lee, *Scr. Mater.*, 66 (2012) 1012-1017.
- [37] K. Chung, N. Ma, T. Park, D. Kim, D. Yoo, C. Kim, *Int. J. Plast.*, 27 (2011) 1485-1511.
- [38] Y. Bai, T. Wierzbicki, *Int. J. Fract.*, 161 (2010) 1-20.
- [39] M. Dunand, D. Mohr, *J. Mech. Phys. Solids*, 66 (2014) 133-153.
- [40] D. Mohr, S.J. Marcadet, *Int. J. Solids Struct.*, 67 (2015) 40-55.
- [41] . Ramazani, K. Mukherjee, A. Schwedt, P. Goravanchi, U. Prah, W. Bleck, *Int. J. Plast.*, 43 (2013) 128-152.
- [42] V. Uthaisangasuk, U. Prah, W. Bleck, *Eng. Fract. Mech.*, 78 (2011) 469-486.
- [43] X. Sun, K.S. Choi, W.N. Liu, M.A. Khaleel, *Int. J. Plast.*, 25 (2009) 1888-1909.
- [44] S.K. Paul, *Materialia*, 9 (2020) 100566.

Chapter 4

Prediction of hole expansion ratio for hyper burring steel

4.1 Introduction

Stretchability of sheet materials as a measure of edge fracture has drawn increasing attention in automotive part forming processes. Successful forming without edge cracking is of particular concern as the microstructures of newly generated high strength steels have become complex and multi-phased. In the edge regions of sheet metals, the material experiences large plastic deformation, which is mainly uniaxial tension, but the formability of this edge region is significantly enhanced owing to the free surface. The geometrical instability, typically observed in the uniaxial tension test for ductile metals, is delayed owing to the compatibility between the free edge and surrounding material [1].

To prevent edge crack and increase stretch-flangeability, the hyper-burring (HB) steel was developed. HB steel consists of a single phase ferrite and has a homogeneous microstructure. In the case of single-phase steel such as HB steel, strain localization resulting from microstructural factors cannot be reflected by a conventional numerical approach that does not take into account hardening by dislocation pile ups near grain boundaries. In this chapter, the hole expansion ratio of HB steel was predicted using the dual-scale model combined with dislocation pile-

up model proposed in the previous chapter. For the fracture criterion to predict the hole expansion ratio, conventionally used Cockcroft and Latham, Clift criterion, along with the local stress triaxiality fracture criterion proposed in the previous chapter were used, and the predicted HER values were compared with experimentally measured one.

4.2 Microstructure and mechanical behavior

The material employed in this study is a hot-rolled hyper-burring steel with the tensile strength of 780 MPa and thickness of 3 mm. The material is named as “HB780” steel hereafter. The chemical composition of HB780 steel is listed in Table 4.1

The microstructure of the HB780 steel sheet was observed using electron backscatter diffraction (EBSD) and the image quality (IQ) map and the normal direction (ND) inverse pole figure obtained by applying a step size of 50 nm and a misorientation angle of 5° are shown in Fig. 4.1. The microstructure indicates that the HB780 steel consists of polygonal and acicular ferritic phases and the average grain size was ~5 μm .

The basic mechanical properties were obtained from the standard uniaxial tensile test following the ASTM E8 standard. Sub-sized specimens with the dimensions 25 mm \times 6 mm (length \times width in gage section) fabricated along the rolling direction of the sheet were used. Along with a regular smooth tensile specimen, two notched tensile specimens, with notch radii 2 mm and 4 mm, were prepared for the notch tensile tests. The measured load–displacement curves for both smooth and notch tensile tests are presented in Fig. 4.2a. For the smooth tensile test, the engineering stress–strain curve and true stress–strain curve are shown in Fig. 4.2b and Fig. 4.2c, respectively. The reference strain rate for the test was 0.002/s. The stress–strain curve shows the yield point elongation up to a strain of 3% and subsequent moderate hardening. The uniform elongation and total elongation are 12.9%, and 23.6%, respectively. The large post-uniform elongation (over 11%) of

the investigated steel may contribute to the higher formability before fracture during the HET. The elastic and plastic properties of the steel sheet are listed in Table 4.2. The Poisson's ratio was assumed to be 0.3 and the other properties were directly measured from the stress–strain curves.

For the measurement of HER, the initial diameter of 10 mm was fabricated from a sample sheet of dimensions 50 mm × 50 mm through wire cut. All the tests were conducted with a punch velocity of 8 mm/min with a holding force sufficiently large for preventing the drawing of the sheet. The test was stopped when the primary crack propagated throughout the sample thickness. Note that the hole edge was prepared by machining rather than by punching, which is suitable for practical applications. The measured HER of HB780 was $180 \pm 20\%$.

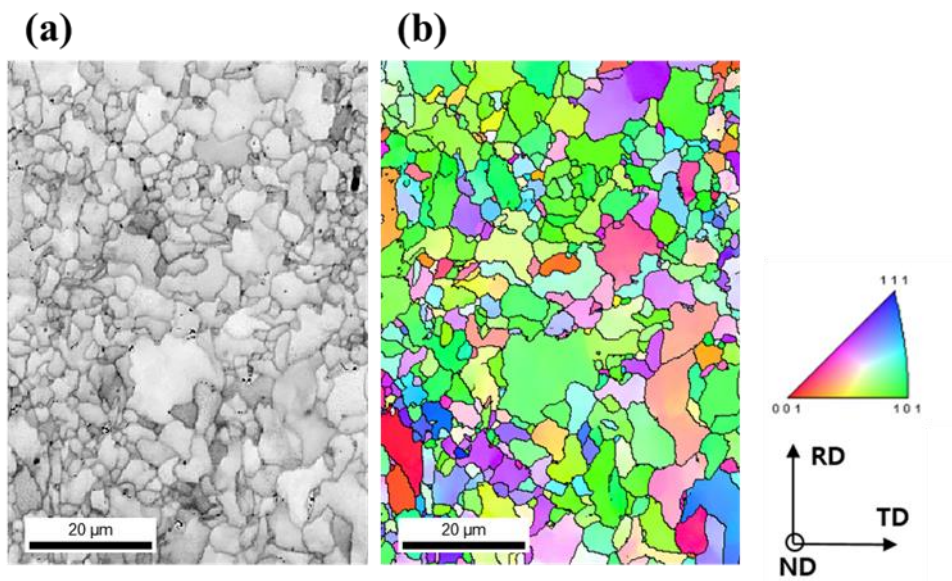


Figure 4.1 Microstructure of the investigated steel. (a) IQ map and (b) ND inverse pole figure map.

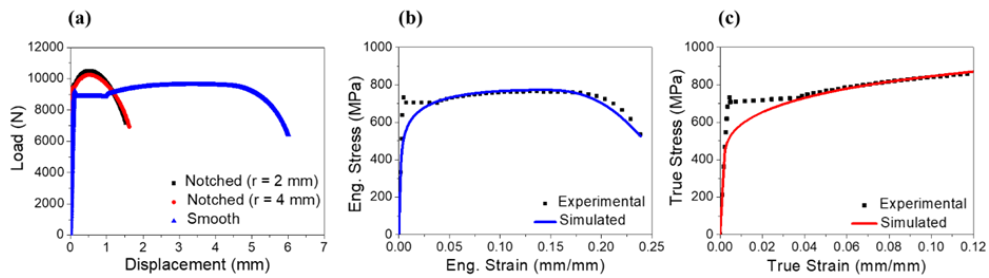


Figure 4.2 Results of uniaxial tensile tests: (a) Experimental load–displacement curves for the smooth and notched tensile tests, (b) comparison between the experimental engineering stress–strain curve and the one simulated (blue line) using the Swift hardening model, and (c) comparison between the experimental and simulated (red line) true stress–strain curves using dislocation-based constitutive equations.

Table 4.1 Chemical composition of HB780 steel sheet (weight %).

Elements (wt.%)							
Fe	C	Si	Mn	Ti	Nb	Cu	Ni
Bal.	0.055	0.05–0.1	1.0–1.5	0.1	0.02	0.01	0.01

Table 4.2 Chemical composition of HB780 steel sheet (weight %).

Young's modulus (GPa)	Poisson's ratio	Yield stress (MPa)		Tensile stress (MPa)	Uniform elongation (%)
		Upper	Lower		
208	0.3	737	705	770	12.9

4.3 Dual-scale FE simulation

4.3.1 Macroscale simulation

A simple uniaxial tension simulation was performed through the conventional continuum-based finite element method using an isotropic elasto-plastic constitutive model. The von Mises yield function and isotropic hardening based on the Swift hardening law were used for this macroscopic model. Note that the investigated material exhibits anisotropy but the present analysis assumes isotropic plasticity for simplicity. The Swift hardening equation fitted to the measured uniaxial tensile stress–strain curve of HB780 steel was

$$\sigma = K(\varepsilon_0 + \bar{\varepsilon}_p)^n \quad (1)$$

where K , ε_0 , and n are material constants. In this study, the engineering stress–strain curve was used to fit the Swift hardening equation to obtain the deformation history until the onset of fracture. As the post-uniform deformation is sensitive to the size of finite element meshes, preliminary simulations were performed before determining an optimum mesh size, which resulted in converged solutions without noticeable differences with a smaller size of elements. The hardening model could fit the measured engineering stress–strain curve with reasonable accuracy except in the initial yield point elongation region as shown in Fig. 4.2b. The best-fitting parameters for the hardening model are listed in Table 4.3. Besides the standard uniaxial tensile test, the macroscale simulations of notched tensile tests were conducted to consider the effect of stress triaxiality. The material constants for the

macroscale uniaxial tensile simulation were the same for all the tensile specimens. The details of finite element models for the uniaxial tensile tests with the corresponding specimen geometries are presented in Fig. 4.3.

Hole expansion simulations were conducted with the isotropic elasto-plastic constitutive model as in the case of the uniaxial tensile simulations. Fig. 4.4a shows the schematic representations of the hole expansion model. The same 3D 8-node continuum elements (C3D8) were used for a blank sheet, whereas 3D 4-node rigid body elements (R3D4) were used for a punch, die, holder, and hole expansion tip. For the hole expansion simulation, the tip angle was 60° . The friction between the blank sheet and tools was modeled with the Coulomb friction coefficient of 0.1. Finer meshes were used near the hole edge to extract more accurate deformation histories during the hole expansion simulations (Fig. 4.4b). Note that an axisymmetric mesh can also be used for the present simulation with isotropic constitutive laws. However, for future applications of the present model for the anisotropic constitutive law, the quarter model was employed in this study (Fig. 4.4b). All the simulations were performed using static implicit finite element code with rate-independent constitutive models; thus, the speed of hole tip movement does not influence the simulation results. The effect of strain rate on the hole expansion deformation will be a future topic of research.

From the macroscopic simulations of hole expansion, the deformation history was provided to the microscale RVE model for further analysis. Three different spots were selected through the sheet thickness to investigate the local deformation

behavior along the thickness direction. The principal strains were again recorded during the hole expansion simulations, which were used for the boundary conditions of the microscale RVE models. The deformation paths of the three distinctive spots at the hole edge were prescribed for different fracture models. Fig. 4.5 shows that the three spots (Spots 1, 2, and 3) represent the uniaxial-tension-like deformation mode from the three calculated principal strain histories during the hole expansion simulations. Among the three spots, spot 3 has a distinctive strain path from the other two spots, which is due to the contact between the blank sheet and conical punch. Note that strain hardening induced during the hole surface preparation was not considered for the wire cut hole edge. The HER was measured when the fracture criterion of each ductile fracture model was satisfied among the three spots.

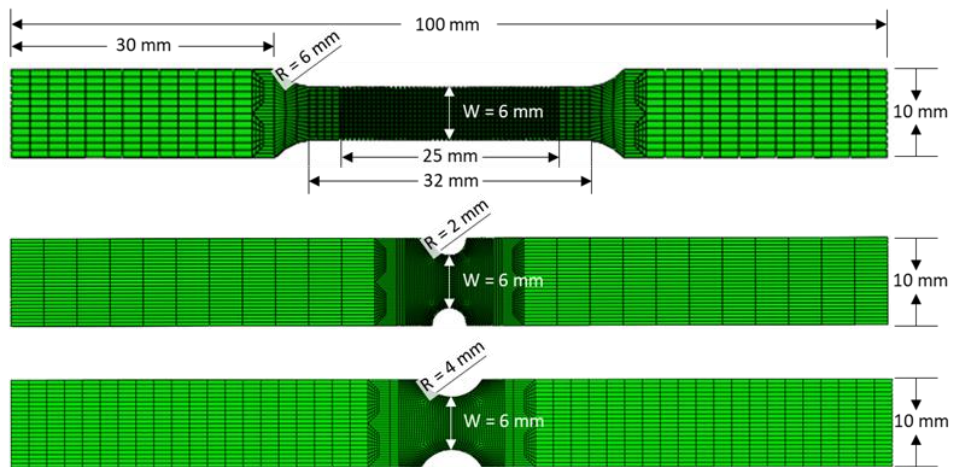


Figure 4.3 Finite element models of the uniaxial tensile tests. The thickness of all models is 3 mm.

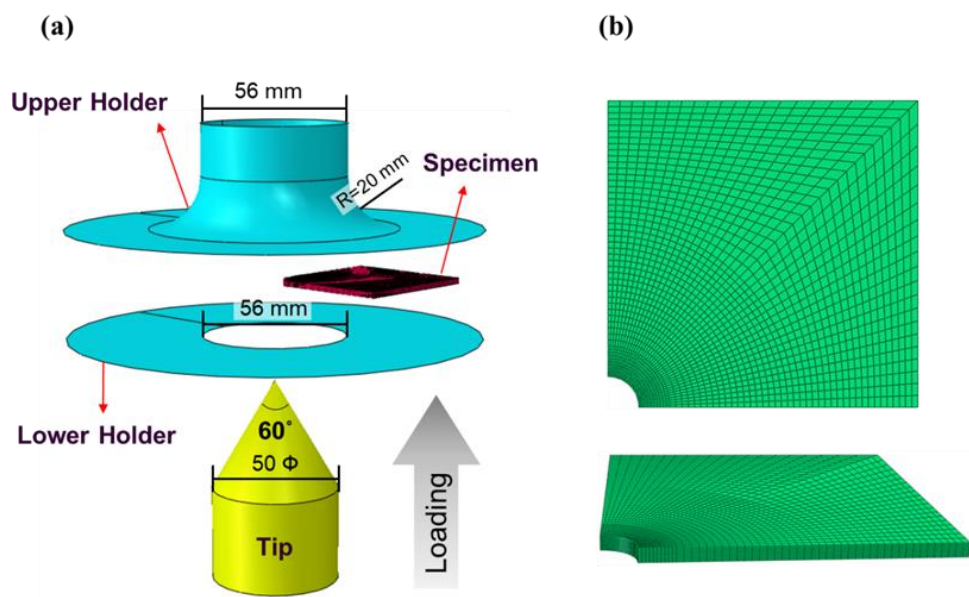


Figure 4.4 (a) Finite element model of the HET and (b) mesh configuration of the specimen.

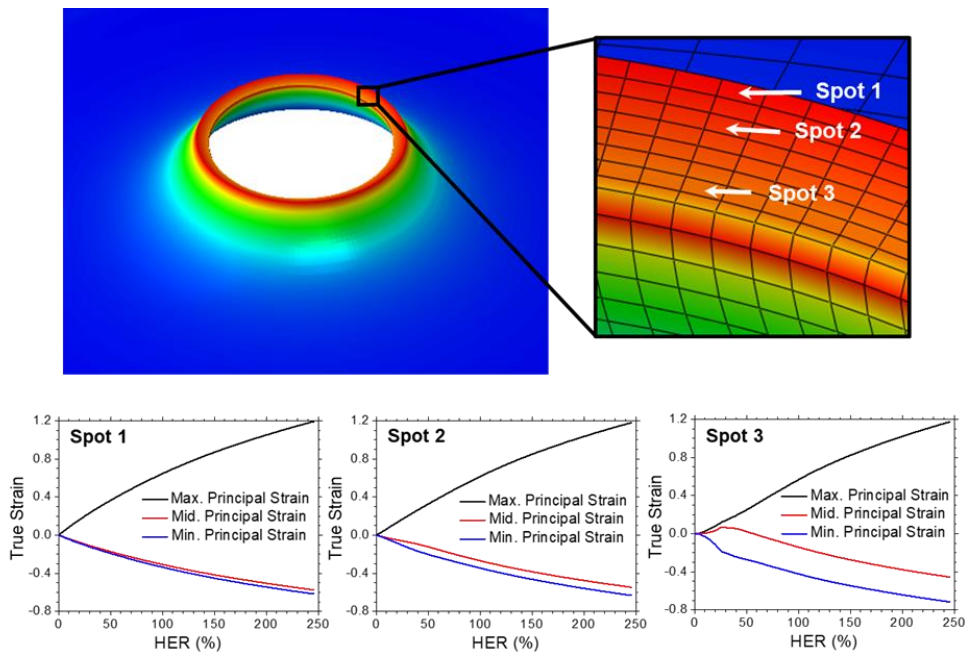


Figure 4.5 Deformed mesh after the HET simulation. The strain histories were extracted at three points of the hole edge (i.e. Spot 1, Spot 2, Spot 3).

Table 4.3 Optimized material parameters used in macro and micro constitutive equations.

K (MPa)	ε_0	n	A	p (m)
1138.9	3.429×10^{-9}	0.1322	60	3×10^{-7}

4.3.2 Microscale simulation

The microscale-level simulation utilizes the RVE constructed from the experimentally measured EBSD data. The grain boundary map was first obtained from EBSD by applying a misorientation angle of 5° , which was used for meshing with a 3-D continuum element for the finite element simulations. The RVE size was determined through preliminary sensitivity simulations using various sizes of RVE. The optimum RVE size was selected based on a difference in the stress-strain curve lower than 1%, when compared with a larger size. The determined optimum RVE size was $20\ \mu\text{m} \times 20\ \mu\text{m}$ with the thickness of $0.5\ \mu\text{m}$. Although the average grain size is much smaller than the thickness of the investigated steel, the RVE was assumed to be columnar for simplicity of computation. The effect of a realistic 3-D microstructure will be investigated in future work. Fig. 4.6 shows the procedure of constructing the RVE from the EBSD map. The optimized RVE has approximately 90,000 3-D continuum elements (C3D8) and 120,000 nodes. Note that more refined meshes were used near the grain boundaries to capture the localized plastic deformation by piled-up dislocation density profile, while rather coarse meshes were used in the grain interior to represent more homogeneous deformation for computational efficiency.

The constitutive models for the microscale-level simulation were based on isotropic linear elasticity and isotropic plasticity. For the hardening in the plastic deformation, the dislocation-density-based model introduced in the previous section was employed.

$$\sigma = \sigma_0 + \alpha \cdot M \cdot \mu \cdot \sqrt{b} \cdot \sqrt{\frac{1 - \exp(-M \cdot k_r \cdot \varepsilon)}{k_r \cdot L_m}} \quad (2)$$

The strengthening by the solid solution σ_0 can be calculated from the empirical equation for the chemical composition as follows [2]:

$$\sigma_0 = 77 + 750 \cdot \text{wt}\%P + 60 \cdot \text{wt}\%Si + 80 \cdot \text{wt}\%Cu + 45 \cdot \text{wt}\%Ni + 60 \cdot \text{wt}\%Cr + 80 \cdot \text{wt}\%Mn + 11 \cdot \text{wt}\%Mo + 5000 \cdot \text{wt}\%C \quad (3)$$

From the chemical composition of the investigated steel, the resulting σ_0 is 470 MPa.

The material parameters in Eq. (2) have been reported in literature for steels with similar microstructures and they are listed in Table 4.4.

As mentioned in the previous chapter, two model parameters A and p are to be optimized for microscale simulation using the dislocation-density-based hardening model. The two material parameters A and p are determined by iteratively fitting the experimental true stress–true strain curve using the microscale simulations. The true stress–true strain curve obtained from the best-fitting parameters of the dislocation-density-based hardening model in the microscale simulation is shown in Fig. 4.2c, which shows consistency with the experimental curve. The parameters determined through the dual-scale simulation approach are listed in Table 4.3. Note that only the two parameters A and p are determined from the simulations, whereas all other parameters were obtained from either literature or direct measurement. Figs. 4.7a–c show examples of microscale simulation under uniaxial tension, in which the contour maps of (a) dislocation density, (b) effective stress, and (c) local logarithmic strain distribution at the macroscopic strain of 0.10 are shown. Note that the current

microscale simulation can represent the local strengthening at the grain boundaries
and the inhomogeneity of plastic deformation at the grain interior

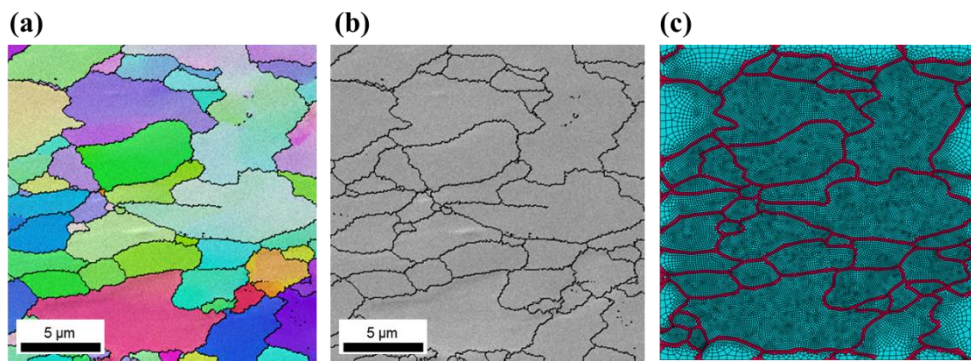


Figure 4.6 (a) RVE generated from the EBSD image. (a) IPF map, (b) grain boundary map, and (c) mesh generated from microstructure image.

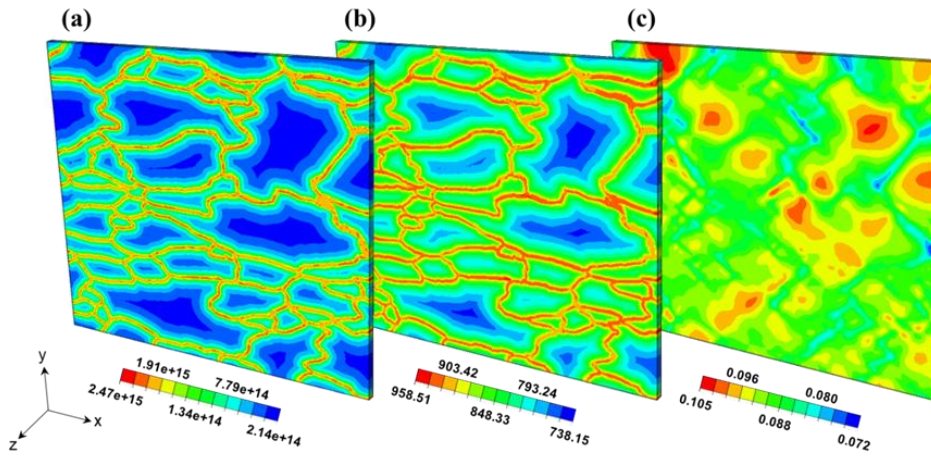


Figure 4.7 Contour map of (a) dislocation density (1/m²), (b) effective stress (MPa), and (c) logarithmic strain under the macroscopic strain of 0.10.

Table 4.4 Material constants for the dislocation-density-based hardening model [3].

α	M	μ (GPa)	b (m)	k_r (Unitless)
0.33	3	80	2.5×10^{-10}	$10^{-5}/d$ (d, grain size)

4.3.3 Fracture criterion

Various approaches for estimating fracture of materials have been proposed, which can be classified into two major groups: coupled plasticity and damage models, and uncoupled fracture criteria [4-7]. In this study, the uncoupled approach was employed owing to its simple integration in finite element simulations. In this approach, the fracture criterion, which is independent of the plasticity model, is applied for evaluating the initiation of fracture. Four different fracture criteria were considered in the present study. The simplest fracture criterion used in this study is the constant equivalent fracture strain model [8].

$$\bar{\varepsilon} = \sqrt{\frac{2}{3} \varepsilon_{ij} \varepsilon_{ij}} = C_1 \quad (4)$$

where C_1 is a critical fracture strain. In this fracture model, the fracture is initiated when the accumulated equivalent plastic strain reaches a critical value.

The maximum principal stress can also be used as a criterion for fracture as suggested by Cockcroft and Latham [9]

$$\int_0^{\bar{\varepsilon}_f} \sigma_1 d\bar{\varepsilon} = C_2 \quad (5)$$

where σ_1 is the maximum principal tensile stress and C_2 is a critical fracture value.

Clift suggested that fracture occurs when the total plastic work reaches a critical value as follows [10]:

$$\int_0^{\bar{\varepsilon}_f} \bar{\sigma} d\bar{\varepsilon} = C_3 \quad (6)$$

where $\bar{\sigma}$ is the effective stress and C_3 is a critical fracture value.

These three models are selected since their implementation in the finite element

simulation is simple and they have been used in various fields. However, these simple models cannot consider the dependency of different stress states including the effect of hydrostatic stress. Therefore, as proposed in the previous chapter, a simplified local-stress-triaxiality-dependent model is employed to investigate the effect of local stress triaxiality on the critical fracture strain. Fig. 4.8 shows the variation of local stress triaxiality under the uniaxial tensile test at the strain of 0.1 for the investigated material and specimen. Note that as in the case of ferrite bainite steel, the stress triaxiality in most of the region deviates from 0.33 (which corresponds to the value of macroscopic uniaxial tensile stress state) and it is higher at the grain interior than at the grain boundary region owing to the high effective stress induced by dislocation pile-up. Though there are models that consider both the effect of stress triaxiality and Lode parameter on the ductile fracture of metallic materials, a simplified exponential form, function of stress triaxiality, was used in this study to take into account the effect of the local stress state, induced by the local deformation inhomogeneity in the microscale model. The simplified model can be comparatively analyzed with other even simpler models used in the phenomenological numerical approach.

$$\bar{\varepsilon}_f = B_1 \cdot \exp\left(-B_2 \cdot \frac{\sigma_m}{\sigma}\right) + B_3 \quad (7)$$

where B_1 , B_2 , and B_3 are material constants determined from the microscale tensile simulation with different strain histories obtained from the macroscale notch tensile simulations.

The critical fracture values C_1 – C_3 were determined from the microscale uniaxial tensile simulation using the prescribed strain histories obtained from the macroscale uniaxial tensile simulation. For each step, the current value of the criterion is stored, by introducing a state variable. When the simulated load-displacement curve matches with the experimental one, the maximum value of the criterion is taken as the critical fracture value. The determined fracture values of the three models are listed in Table 4.5. For the fracture model with stress triaxiality dependency, additional tensile tests with notched specimens of radii 2 mm and 4 mm were conducted. The three constants B_1 , B_2 , and B_3 were obtained from the averaged stress triaxiality with respect to the equivalent plastic strain and the equivalent fracture strain $\bar{\varepsilon}_f$ obtained from the microscale simulation of uniaxial tensile tests for smooth and notched tensile specimens. As fracture is highly associated with the stress triaxiality, the analysis was performed for the material point with the maximum stress triaxiality in the RVE. As the stress triaxiality changes during the deformation as shown in Fig. 4.9a, the averaged value of stress triaxiality until fracture was used for fitting Eq.(7). The identification was performed considering a constant averaged value for each test condition, to simplify the analysis. A more rigorous identification could be developed to consider the effect of the evolution of the triaxiality during the deformation. The maximum value of stress triaxiality (at the grain interior) slightly decreased under the deformation of the smooth uniaxial tensile test because the stress deviation between the grain boundary and grain interior was diminished. In contrast, there was still a noticeable difference between the effective stress at the

grain boundary and grain interior up to fracture for the notched tensile test and a reduction of stress triaxiality was not observed. The determined constants are listed in Table 4.5. Fig. 4.9b shows the exponential type fracture criterion as a function of stress triaxiality, which was drawn from the determined fracture parameters. The presented fracture criterion may be over-simplified owing to the non-consideration of the fractures of shear- or compression-dominated deformation mode, which can be implemented with more rigorous models [23, 41]. However, considering that the major deformation mode in the hole expansion process is stretch-dominated, the current simplification might be reasonable considering its simplicity.

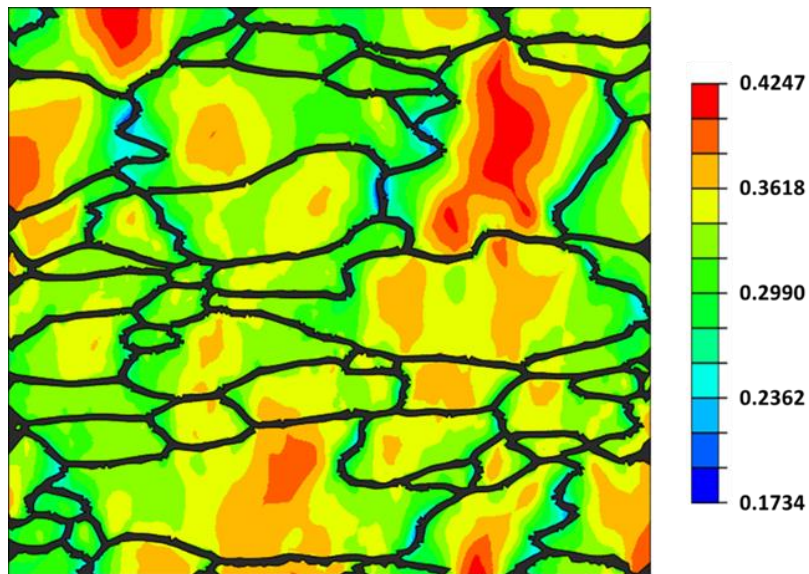


Figure 4.8 Contour map (top view) of stress triaxiality under the uniaxial tension at the strain of 0.1. The grain boundary elements are superimposed.

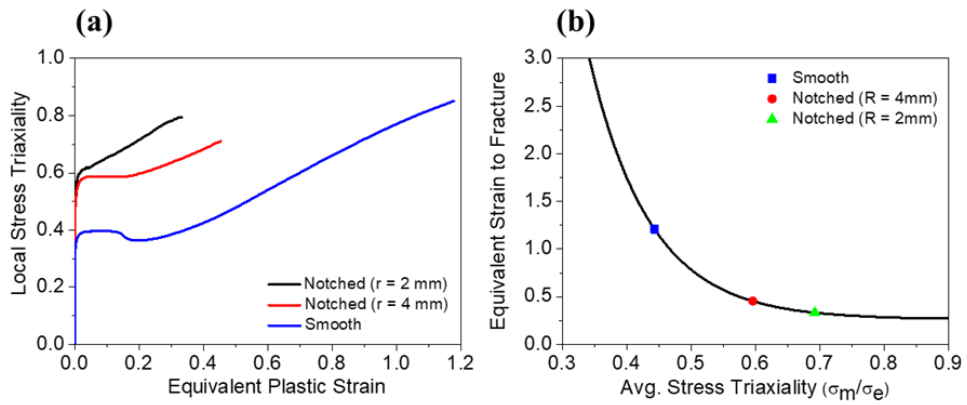


Figure 4.9 (a) Simulated local stress triaxiality during the uniaxial tensile tests and (b) the relationship between the equivalent strain to fracture and stress triaxiality under various stress conditions.

Table 4.5 Critical fracture values and material constants for each fracture criterion.

C_1	C_2 (MPa)	C_3 (MPa)	B_1	B_2	B_3
1.207	1483.25	1230.64	98.73	-10.49	0.2635

4.3.4 Hole expansion test

The deformation history (or strain path) of the macroscale hole expansion simulation was imposed as the boundary conditions of the RVE model. In the microscale simulations, the deformation paths of the three distinctive spots at the hole edge were prescribed for different fracture models. Fig. 4.5 shows that the three spots (Spots 1, 2, and 3) represent the uniaxial-tension-like deformation mode from the three calculated principal strain histories during the hole expansion simulations. Among the three spots, spot 3 has a distinctive strain path from the other two spots, which is due to the contact between the blank sheet and conical punch. Note that strain hardening induced during the hole surface preparation was not considered for the wire cut hole edge. The HER was measured when the fracture criterion of each ductile fracture model was satisfied among the three spots. Fig. 4.10a-c shows the equivalent plastic strain distributions of the three spots in the RVE predicted with the constant fracture strain criterion and their corresponding HERs. The initial fracture was indicated at spot 3 and the predicted HER was 207%. Fig. 4.11a-c shows the results of Cockcroft–Latham criterion, in which no fracture was initiated at the three spots even after an HER of 245.7%. The Clift criterion resulted in fracture initiation at spot 3 with the HER of 215%, which is shown in Fig. 4.12a-c. Except the Cockcroft–Latham criterion, the ductile fracture models based on the plastic strain and plastic work predicted the initiation of fracture at spot 3. From a microstructural point of view, the predicted fracture point was at the grain interior for the constant fracture strain criterion, but at the grain boundary for the other two criteria.

The same procedure was applied for the RVE with the simplified stress-triaxiality-dependent ductile fracture model. Fig. 4.13a shows the equivalent plastic strains of three critical elements at each spot as a function of stress triaxiality. Based on the prescribed fracture criterion, it was estimated that the fracture was initiated at spot 1 first. Note that the stress triaxiality gradually increased during deformation. This can be considered by introducing the apparent effective fracture strain, $\bar{\varepsilon}_f^*$, which is given as [11]

$$\bar{\varepsilon}_f^*(\eta) = \int d\bar{\varepsilon} - \bar{\varepsilon}_f(\eta)(1 - \omega) \quad (8)$$

with the damage initiation parameter, ω , given by

$$\omega = \int d\omega = \int \frac{d\bar{\varepsilon}}{\bar{\varepsilon}_f(\eta)} \quad (9)$$

where $\bar{\varepsilon}_f$ and $\bar{\varepsilon}_f^*$ are the deformation-path-independent effective fracture strain and apparent effective fracture strain, which is obtained by considering the deformation history, respectively, and $\bar{\varepsilon}_f(\eta)$ and $\bar{\varepsilon}_f^*(\eta)$ are the current values at $\eta = \bar{\eta}$. The detailed derivation of the apparent effective fracture strain can be found in [11]. In Fig. 4.13b, the solid line (which corresponds to $\bar{\varepsilon}_f$) is the deformation-path-independent reference value obtained from three microscale tensile simulations, whereas the dotted line is the apparent fracture strain obtained by considering the deformation history change. The corresponding HER was 192% and this value is much less than the one predicted by the stress triaxiality independent models. The

results also showed that the fractured spot is different from that of the other models. Fig. 4.14 shows the comparison of the predicted HERs from all four fracture criteria with the experimentally measured HER values. Notably, the HER could be better captured when the fracture criterion considers the stress triaxiality developed in the microstructure. The other three fracture models, which do not consider the effect of triaxiality, overestimated the experimental HER value. In the experiment, the exact fracture initiation site could not be accurately captured owing to very fast propagation of fracture through the thickness once initiated. Despite this uncertainty regarding the crack initiation site, many large cracks observed near the upper edge of the hole (which corresponds to spot 1). In addition, the stress state at the upper edge is similar to that of uniaxial tension, which is favorable for void nucleation as in the study of Butcher et al. [12]. Thus, it can be assumed that the upper edge is more vulnerable to fracture.

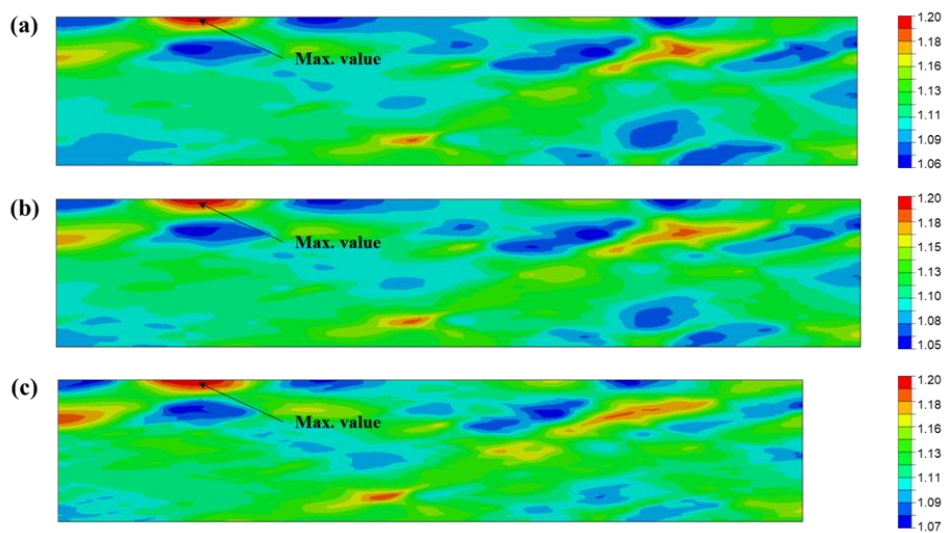


Figure 4.10 Contour map (top view) of constant fracture strain (a) Spot 1 (HER: 225%), (b) Spot 2 (HER: 228%), (c) Spot 3 (HER: 207%).

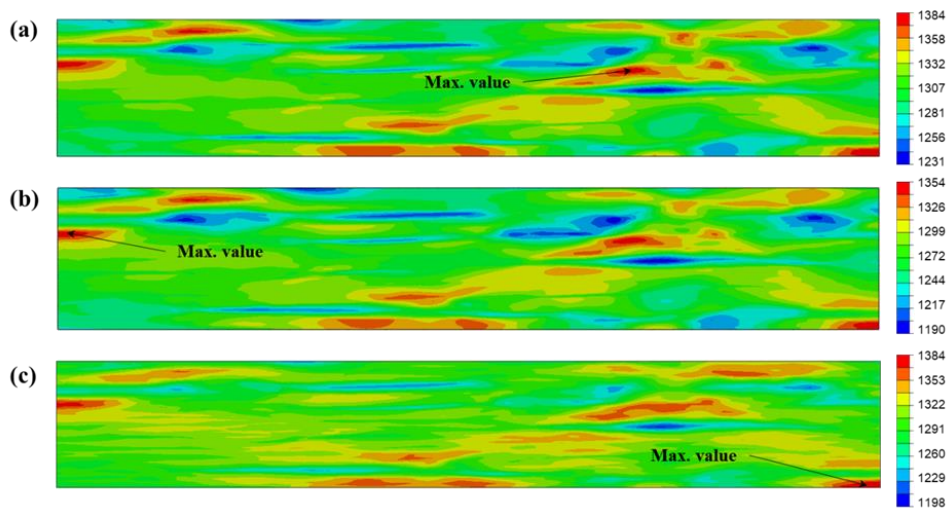


Figure 4.11 Contour map (top view) of the Cockcroft–Latham criterion (a) Spot 1 (HER: > 245.7%), (b) Spot 2 (HER: > 245.7%), (c) Spot 3 (HER: > 245.7%). No fracture occurred for each spot over an HER of 245.7%.

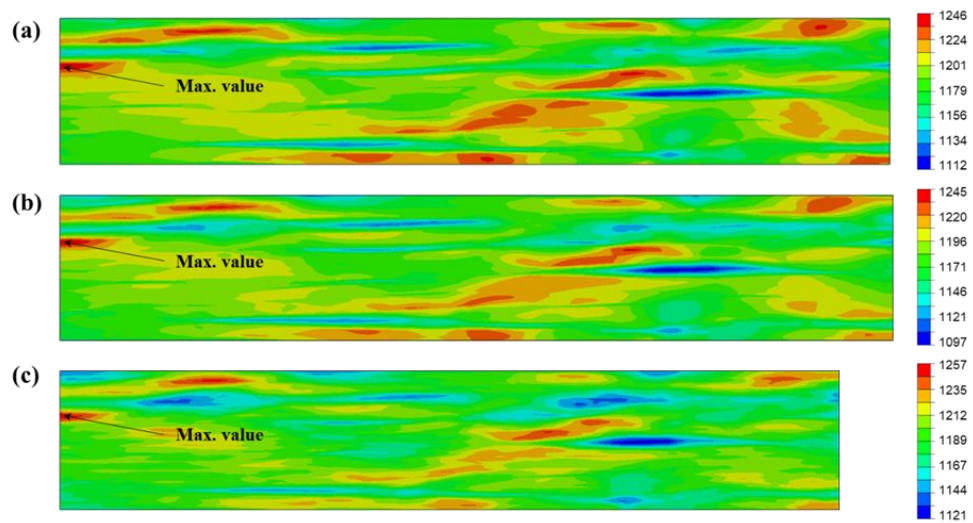


Figure 4.12 Contour map (top view) of the Clift criterion (a) Spot 1 (HER: 233%), (b) Spot 2 (HER: 235%), (c) Spot 3 (HER: 215%).

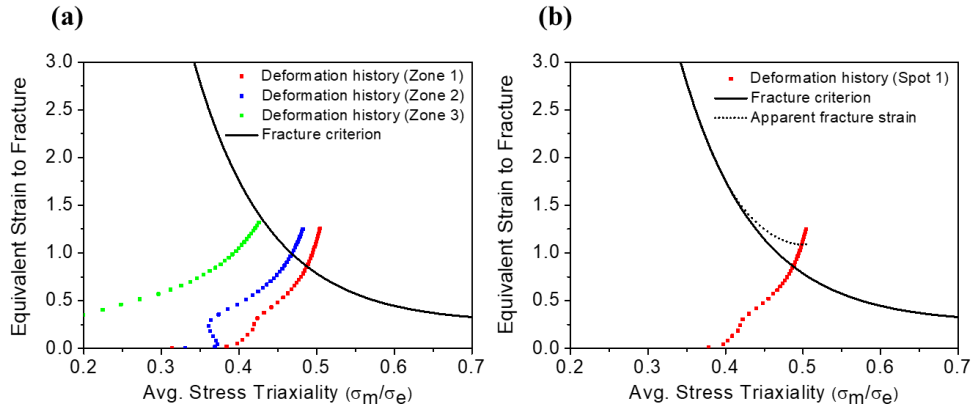


Figure 4.13 (a) Equivalent plastic strains of three critical elements at each spot as a function of stress triaxiality and (b) the apparent fracture strain considering the deformation history at spot 1.

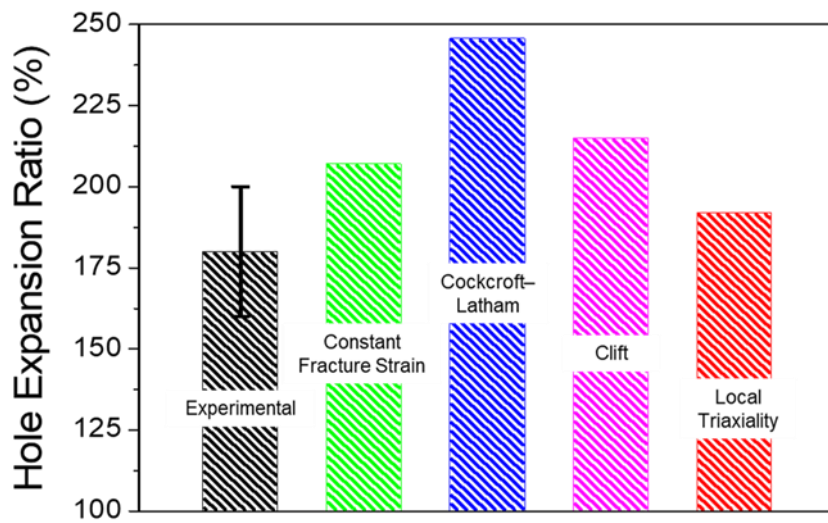


Figure 4.14 HER values predicted using various fracture criteria.

4.4 Effect of microstructural factors on HER: numerical sensitivity study

4.4.1 Grain size

A Numerous studies have been conducted on the relationship between the microstructure of the material and the HER. Uthaisangsuk et al. [13] conducted finite element simulation with two arbitrarily constructed RVE models containing different martensite volume fractions in order to investigate the influence of a multiphase microstructure on the mechanical properties and fracture mechanism. Kim et al. [14] conducted realistic microstructure-based finite element analysis for two DP steel sheets with different martensite volume fractions and morphological features to investigate the role of phase morphology in strain localization under the hole expansion test. In this study, the effect of grain size, which is a primary microstructure characteristic, on HER was investigated by implementing five different types of microstructure models (Fig. 4.15). Each model maintains the same grain shapes as the original one, whereas its size is expanded to 2 to 5 times that of the original model.

The material parameters for the microscale simulation were obtained for each model by fitting the true stress–true strain curve of HB780 and the resulting parameters are listed in Table 4.6. For each model, the deformation histories of the hole expansion simulation at the three spots (i.e. Spot 1, Spot 2, and Spot 3) were used as a boundary condition for the microscale simulation. From the constant

fracture strain criterion, in a model with a grain size of 10 μm , the HER was increased to 224% compared with that of the model with a grain size of 5 μm (HER: 207%), whereas the model with a grain size of 25 μm exhibited an HER value larger than 245.7%, which is the maximum predictable value in this study. From both Clift and Cockcroft–Latham criteria, no fracture was predicted, even for an HER larger than 245.7%, for all the models. From the perspective of stress triaxiality, when the grain size is enlarged, the stress concentration at the grain boundary decreases. For this reason, the deviation of the stress triaxiality reduces and the apparent fracture strain increases, as shown in Fig. 4.16, since the deformation progressed with a relatively low stress triaxiality, when compared to the model with a grain size of 5 μm . Notably, for a model with a smaller grain size, a larger effect of the grain boundary geometry can be imposed. The predicted HER values were 209%, 226%, and 242% for models with grain sizes ranging from 10 μm to 20 μm , respectively. The model with the grain size of 25 μm exhibited an HER larger than 245.7%. The HERs for different grain sizes are summarized in Table 4.6. Note that the hardening effect owing to grain size was not considered here because all the models used parameter optimization based on the same stress–strain curve.

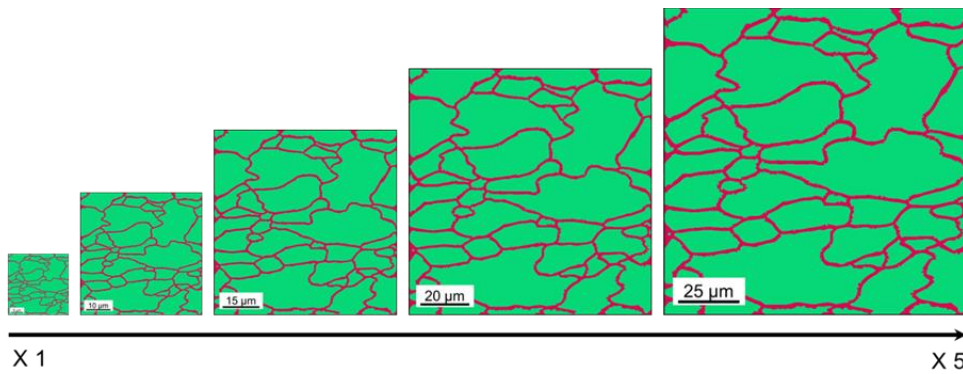


Figure 4.15 Five types of microstructure models. The size of the model has expanded to 2, 3, 4, and 5 times that of the original model (the leftmost one).

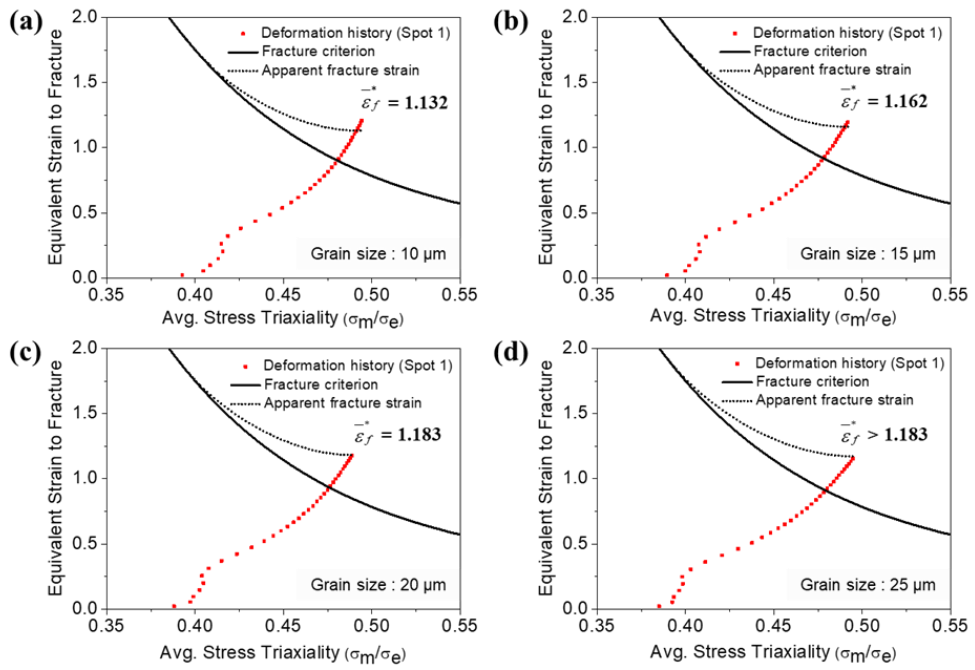


Figure 4.16 Apparent fracture strain and deformation history for models with grain sizes of (a) 10 μm , (b) 15 μm , (c) 20 μm , and (d) 25 μm .

Table 4.6 Optimized material parameters and predicted HER values from the local stress triaxiality criterion for the microscale model with different grain sizes.

10 μm		15 μm		20 μm		25 μm	
A	p (m)	A	p (m)	A	p (m)	A	p (m)
69	2.2×10^{-7}	75	1.8×10^{-7}	81	1.5×10^{-7}	95	1.1×10^{-7}
HER		HER		HER		HER	
209%		226%		242%		>245.7%	

4.4.2 Grain boundary characteristics

Grain boundaries act as obstacles to the movement of mobile dislocations, which form the pile-up of dislocations and induce deformation inhomogeneity. However, the interactions between the mobile dislocations and grain boundaries are very complex and depend on the slip activities and grain boundary characteristics. These interactions have been investigated using TEM highlighting three types of interactions, i.e., the penetration of dislocations through grain boundaries, the reflection of dislocations at grain boundaries, and the absorption of dislocations into grain boundaries [15, 16]. In this section, the effect of dislocation distribution on the HER was investigated by controlling the degree of pile-ups at the grain boundaries as a simplistic approach. This effect can be indirectly verified by adjusting the square root term of Eq. (7). When the exponent 0.5 is lowered, the degree of pile-up can be alleviated. Accordingly, four types of pile-up configurations were assumed including the original one (for convenience, these conditions will be referred to as Cond.1–4, respectively). The material parameters obtained from the fitting of the true stress–true strain curve of HB780 are listed in Table 4.7 and the results of the microscale simulations for Cond.1–4 are presented in Fig. 4.17. As shown in Fig. 4.17(b) and (c), a higher HER was predicted when the degree of pile-up was alleviated (or equivalently less pile-up was formed owing to larger transmission). This is because the stress concentration at the grain boundary was decreased, which results in reduced deviation of stress triaxiality. In other words, the HER increases as the deformation becomes more homogeneous inside the grain.

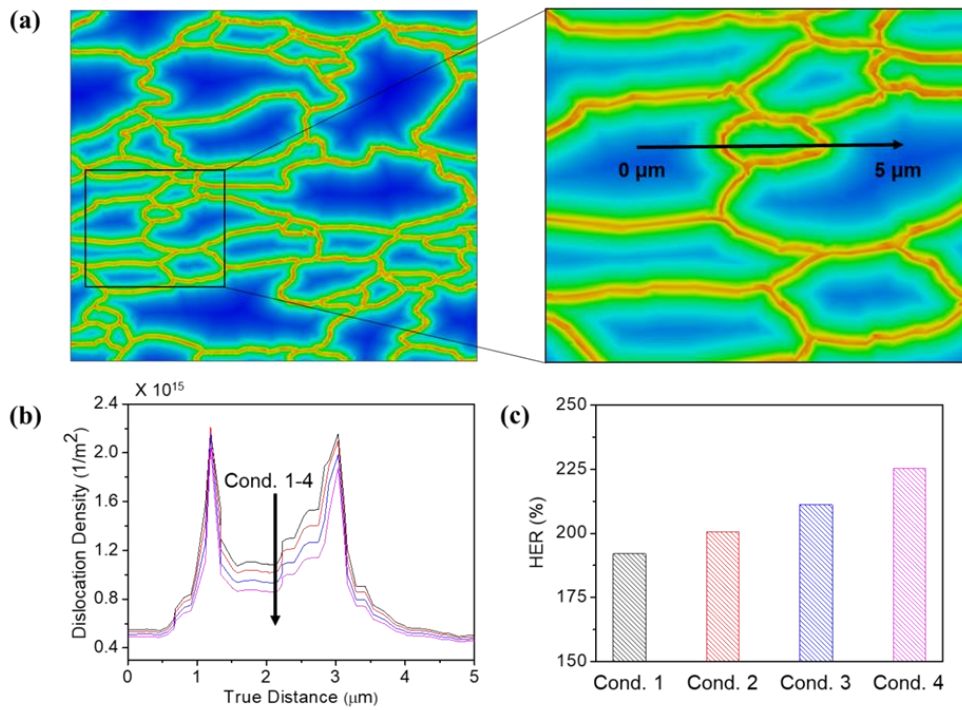


Figure 4.17 Effect of grain boundary characteristics (or dislocation distribution) on HER. (a) The contour map of dislocation density under the true strain of 0.12. The magnified image shows the profiling direction and the distance of dislocation density, (b) the profile of dislocation density, and (c) the predicted HER for each condition.

Table 4.7 Optimized material parameters and predicted HER values from the local stress triaxiality criterion for the microscale model of Cond.2–4.

Cond. 2			Cond. 3			Cond. 4		
A	p (m)	HER	A	p (m)	HER	A	p (m)	HER
60	2.5×10^{-7}	200.5%	58	2.5×10^{-7}	211%	56	2.5×10^{-7}	225.3%

4.5 Conclusion

In this chapter, a dual-scale finite element simulation was proposed to predict the HER of a hyper-burring steel sheet. In the simulation process, macroscale HET was simulated based on classical isotropic elasto-plasticity. The deformation histories at the hole edge as a potential fracture initiation site were used in the lower-scale microstructure-based RVE model as boundary conditions. The microscale model featured the realistic grain morphologies obtained from the experimental microscopy and the dislocation-density-based hardening model in an average sense. For modeling the initiation of the fracture at the hole edge, four different phenomenological ductile fracture models were evaluated in the microscale simulations.

The comparative study on the fracture initiation during the hole expansion simulations with different fracture models showed that HER could be better captured when the fracture criterion considered the stress triaxiality developed in the microstructure. The other fracture models based on either equivalent plastic strain or plastic work significantly overestimated the experimentally measured HER value.

The microstructural factors influencing the HER were investigated by calibrating the numerical parameters of the microscale constitutive models. From the microscopic simulation of HET, a higher HER value could be predicted as the grain size increases and the degree of pile-up decreases. This is because the local stress concentration at the grain boundary increases the inhomogeneity of deformation inside the grain, which eventually decreases the hole expansion formability.

4.6 References

- [1] J.Y. Lee, J.W. Lee, M.-G. Lee, F. Barlat, *Int. J. Solids Struct.*, 49 (2012) 3562-3572.
- [2] A. Ramazani, K. Mukherjee, A. Schwedt, P. Goravanchi, U. Prahl, W. Bleck, *Int. J. Plast.*, 43 (2013) 128-152.
- [3] S.K. Paul, *Comput. Mater. Sci.*, 56 (2012) 34-42.
- [4] L. Xue, T. Wierzbicki, *Eng. Fract. Mech.*, 75 (2008) 3276-3293.
- [5] T. Wierzbicki, Y. B. Bao, Y.W. Lee, Y.L. Bai, *Int. J. Mech. Sci.*, 47 (2005) 719-743.
- [6] S.T. Oh, H.J. Chang, K.H. Oh, H.N. Han, *Met. Mater. Int.*, 12 (2006) 121-129.
- [7] H.N. Han, K.H. Kim, *J. Mater. Process Tech.*, 142 (2003) 231-238.
- [8] X. Teng, T. Wierzbicki, *Eng. Fract. Mech.*, 73 (2006) 1653-1678.
- [9] M.G. Cockcroft, D.J. Latham, *J. Inst. Met.*, 96 (1968) 33-+.
- [10] S.E. Clift, P. Hartley, C.E.N. Sturgess, G.W. Rowe, *Int. J. Mech. Sci.*, 32 (1990) 1-17.
- [11] K. Chung, N. Ma, T. Park, D. Kim, D. Yoo, C. Kim, *Int. J. Plast.*, 27 (2011) 1485-1511.
- [12] C. Butcher, D. Anderson, M. Worswick, *Int. J. Mater. Manuf.*, 6 (2013) 304-312.
- [13] V. Uthaisangsuk, U. Prahl, W. Bleck, *Comput. Mater. Sci.*, 45 (2009) 617-623.
- [14] J.H. Kim, M.-G. Lee, D. Kim, D.K. Matlock, *Mater. Sci. Eng. A*, 527 (2010) 7353-7363.

- [15] Z. Shen, R.H. Wagoner, W.A.T. Clark, *Scr. Metall.* 20 (1986) 921-926.
- [16] T. Kehagias, P. Komninou, G.P. Dimitrakopoulos, J.G. Antonopoulos, T. Karakostas, *Scr. Metall. Mater.*, 30 (1994) 1311-1315.

Chapter 5

Punching effect on hole expansion ratio

5.1 Introduction

The edge crack sensitivity of advanced high-strength steel (AHSS) has been one of the limiting factors for its use in automotive parts. The prominent edge crack sensitivity of AHSS is based on their microstructural features such as difference in hardness of constituent phases. This microstructural inhomogeneity can cause strain localization and is favorable for the initiation and accumulation of ductile damage [1-2].

The hole expansion test is widely adopted as a way to evaluate stretch-flangeability to predict edge cracks. Hole expansion tests are used more often than hole tension [3] and shear edge tension [4], which are performed for the same purpose. On the prediction of hole expansion formability, numerous researches have been done based on finite element simulation [5-6]. In many cases, the effect of microstructure on stretch-flangeability was investigated using representative volume elements (RVEs) and for two different AHSS with similar macroscopic mechanical properties, it was found that the HERs were different [7]. Therefore, in predicting edge cracks, it is difficult to understand in-depth in relation to fracture unless microstructural details are considered. As part of this effort, numerous researches has

been conducted based on the finite element analysis reflecting the actual microstructure [8-9]. Another approach to reflect the microstructural effect is the crystal plasticity, which models the plastic deformation of the material through slip, twinning, and transformation induced plastic deformation, etc.

In addition to the aforementioned microstructure factors, external factors related to the edge manufacturing process also have a great influence on edge cracks. In the case of hole expansion test, it has been reported that hole expandability greatly varies depending on the fabrication method of the hole edge, i.e., machining, drilling, punching, water-jet cutting, etc. Karelova et al. [10] investigated the hole expansion ratio of DP800 and CP800 steel with a hole fabricated by punching, drilling and wire cutting. The result shows that the imperfections and damage evolved near the hole edge during the hole-punching and hole-drilling have a detrimental effect on the HER. The shearing (punching) process introduces severe work hardening in the vicinity of the hole and surface roughness at the hole edge. Pathak et al. [11] evaluated HER for ferritic-martensitic DP and ferritic-bainitic CP steels which have different edge conditions with conical and flat punch. From the measurement results, a higher HER was obtained in the reamed edge condition in both the conical punch and the flat punch. However, in the case of using the conical punch where the crack occurs at the edge of the hole, the measured HER is almost twice higher in the reamed edge condition than that of in the sheared edge condition.

As described above, factors that affect the hole expansion ratio include punch geometry, edge preparation, mechanical properties and microstructure of materials

[12]. In this study, unlike the case of processing of hole through wire cutting, the prediction of the hole expansion ratio was performed by considering the factors that may occur when the hole is fabricated through the punching process. As factors that can affect HER, analysis of surface roughness, work hardening, and edge geometry near the punched hole was performed for various clearance condition. The prediction of HER was conducted through the dual scale finite element simulation described in detail in the previous chapter.

5.2 Punch-die clearance

The schematic representation of punch process is shown in Fig. 5.1. The hole edge condition, which is represented by surface roughness, edge shape and degree of work hardening, is determined by the punch-die clearance. The punch-die clearance is the distance between the cutting edge of the punch and the cutting edge of the die divided by the thickness of material being punched which is defined as follows:

$$clearance(\%) = \frac{D_d - D_p}{2t} \times 100 \quad (1)$$

where D_d , D_p , t are die diameter, punch diameter, and thickness, respectively.

The process parameter optimization is mostly done by numerous experiments which are costly and time consuming. Therefore, in this study, the prediction of HER was performed through numerical simulation using the experimentally measured data. To take into account the punching effect on HET, surface roughness, hole edge geometry, and work hardening degree were analyzed for holes fabricated with 8, 12, and 16% punch-die clearance.

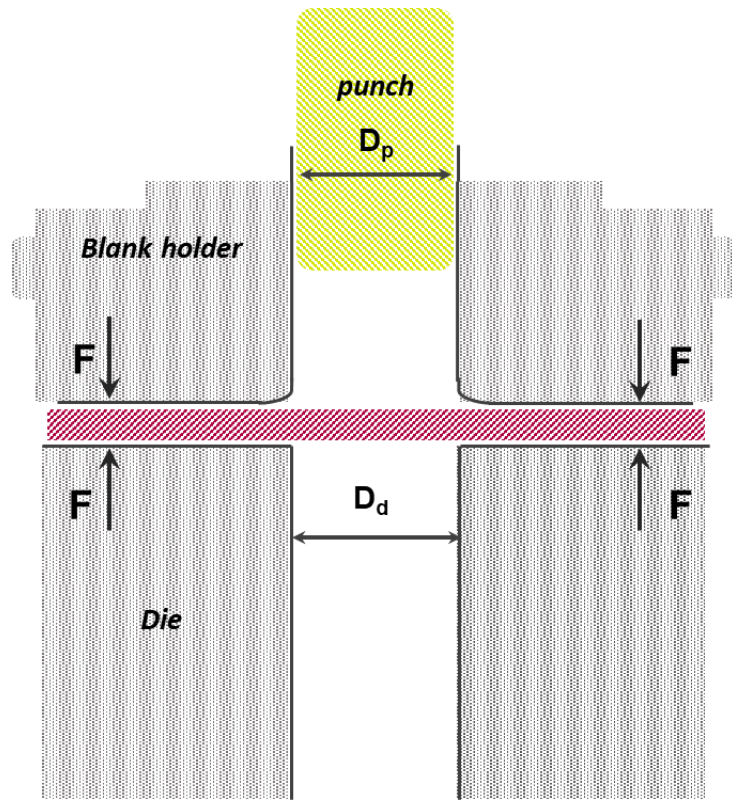


Figure 5.1 The schematic representation of punch process.

5.3 Surface roughness effect on HER

Surface roughness has been considered as one of the factors that can affect edge fracture. In this study, the surface roughness of the hole edge was analyzed by using confocal microscopy. To quantitatively compare the surface roughness by clearance condition, the concept of neighbor roughness distribution (NRD) was introduced as follows:

$$NRD = \frac{1}{N} \sum_{k=1}^N |h_{adj,k} - h| \quad (2)$$

where h , $h_{adj,k}$, N are height at certain point, height of the pixel in the 10th adjacent layer, and total number of pixel, respectively. The reason for calculating the NRD value from the height difference at the 10th layer is that if the adjacent layer is set too small, the height difference may be underestimated. Thus the height difference at the 10th layer is an optimized value at a level where the maximum height difference does not change significantly. The step size was 1.4 μm , and since the height difference was calculated with the 10th adjacent layer, the N value used in the NRD calculation for surface roughness analysis was 80. Fig. 5.2a shows the confocal microscope image and the NRD mapping of microscope image is shown on Fig. 5.2b. The NRD value was evaluated for various conditions. The average NRD value was analyzed for the entire area of the hole edge, and since fracture occurred in the fractured zone, the average NRD value only in the fracture zone was also analyzed. In addition, the average value was calculated for NRD values in excess of 10 microns, because local high surface roughness may have a greater likelihood of causing

fracture. Fig. 5.3 shows the relationship between the average value of NRD and HER for each clearance. From the plot data, it can be seen that the surface roughness did not show any trend with respect to clearance and HER. These results are consistent with the other studies on the relationship between surface roughness and HER. For example, Pathak et al. [11] performed a hole expansion test by polishing the surface of the hole edge to remove the surface roughness of the punched hole specimen, and compared it with the HER of the unpolished specimen. From the experimental results, it was confirmed that there was little difference between the HER value of the specimen from which the surface roughness was removed and the unpolished specimen. From the NRD analysis results and previous studies conducted by other researchers, it can be seen that surface roughness has little effect on HER.

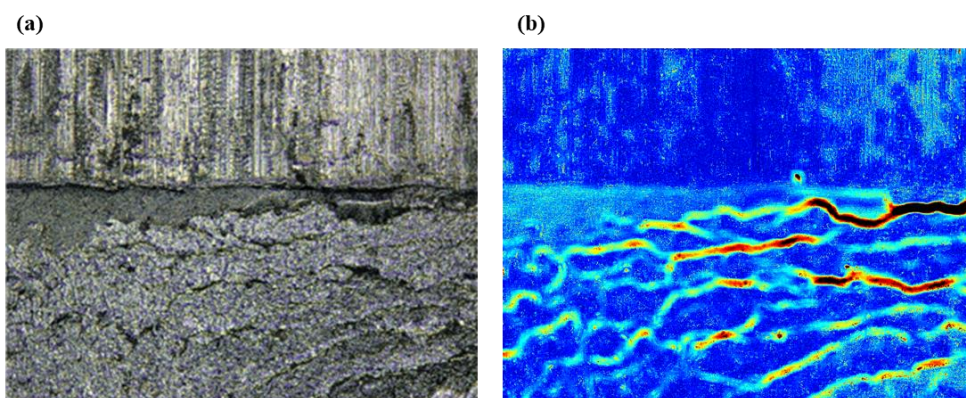


Figure 5.2 The confocal microscope image of hole edge and the neighbor roughness distribution (NRD) mapping of measured image.

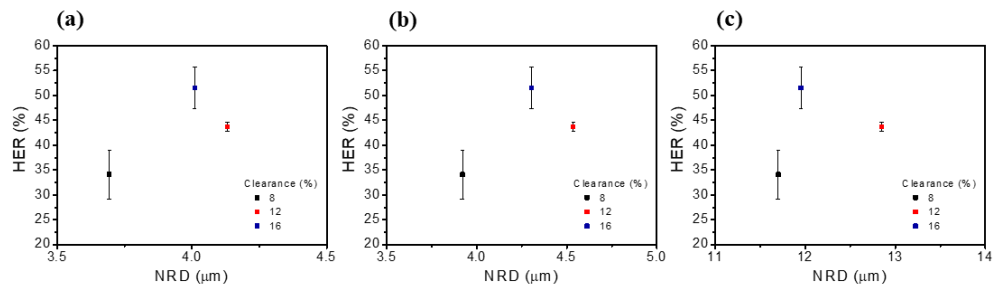


Figure 5.3 The relationship between the NRD and HER for each clearance. Averaged NRD for (a) whole edge region, (b) only fracture region, (c) only fracture region with NRD value over 10 μm .

5.4 Geometrical effect

The hole expansion test according to ISO 16630 standard is to expand the hole with a conical expansion tool with a punch tip angle of $60^\circ \pm 1^\circ$. In addition to the conical punch, many studies have been conducted on hole expansion testing using other punch geometries such as hemispherical and flat bottom punches [13-15]. Konieczny et al. [16] performed a hole expansion test with punch tips with various geometries, and found out that the HER is highest for the conical punch, intermediate for the hemispherical punch, and lowest for the flat bottom punch. Similar results have been reported in many other studies. Pathak et al. [11] also reported that a higher hole expansion ratio was obtained when using a conical punch than when using a flat punch. One interesting point is that HER was not significantly affected by hole edge conditions for flat bottom punches, unlike conical punches. The reason for this difference is that the location where fracture occurs during the hole expansion test is different for each punch geometry. Another reason is that for conical punches, the strain gradient is introduced in the direction of the thickness of the edge of the sample [12]. Therefore, if strain gradient is induced in the direction of the hole edge during the hole expansion test, it can be expected that the shape of the hole edge formed during the hole fabrication process can also affect the HER. In this study, finite element modeling was performed by reflecting the geometry of the hole edge measured after the punching process using a confocal microscope. Fig. 5.4 shows the schematic representation of hole edge for each clearance condition. From the measurement results, it can be seen that the shape of the fracture zone is different for

each clearance condition, and the ratio of the sheared zone and the fractured zone is also different. As a result of the FE simulation, it was confirmed that the maximum principal strain induced to the hole edge decreases as the degree of cut out at the fracture zone increases. The strain history at the spot 1 where fracture occurred obtained through the macroscale hole expansion test simulation was applied as the boundary condition of the microscale simulation. Averaged stress triaxiality versus equivalent plastic strain calculated from the microscale simulation of hole expansion tests is shown in Fig. 5.5 and the resulting hole expansion ratio is presented in Fig. 5.6. From the results of the experiment and FE simulation, as the clearance increases, the slope of the fracture zone formed from punching process becomes larger, and this geometric characteristic acts as a factor to increase the HER. Note that this result did not take into account the work hardening of the specimen caused by punching, and only considered geometric factors. Details on the effect of work hardening induced during the hole fabrication through punching process are described in the next chapter.

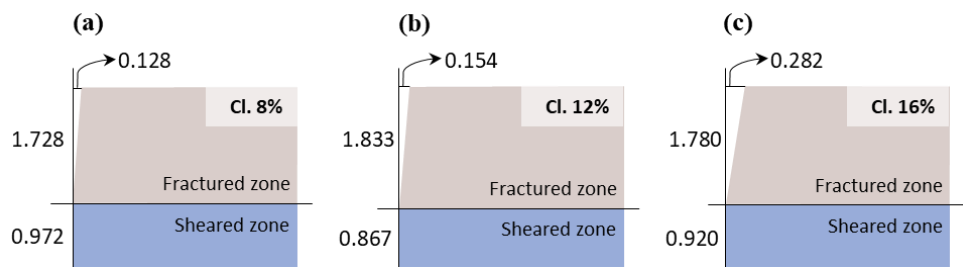


Figure 5.4 The schematic representation of hole edge for each clearance condition.

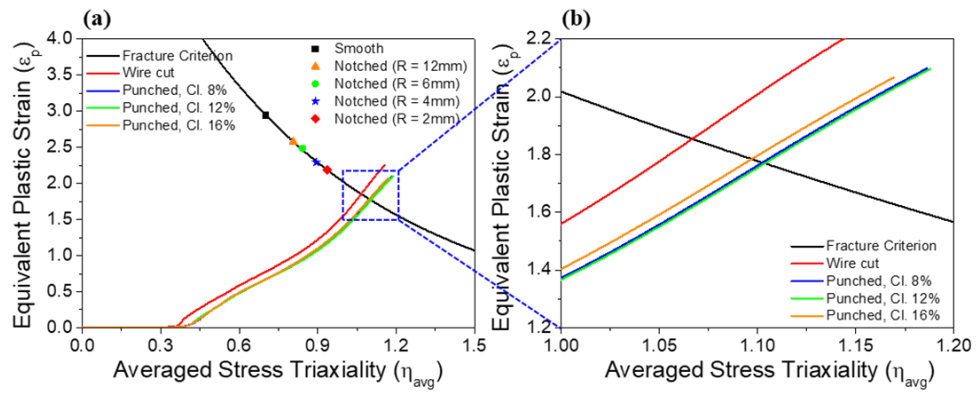


Figure 5.5 Averaged stress triaxiality versus equivalent plastic strain calculated from the microscale simulation of hole expansion tests.

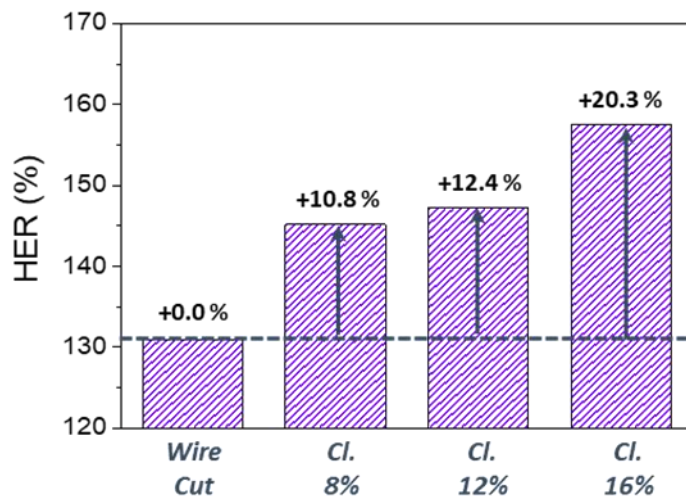


Figure 5.6 Predicted HER from microscale RVE simulation for various clearance condition (work hardening is not considered).

5.5 Work hardening effect

5.5.1 Macroscale simulation

The shear-affected zone (SAZ), which is a pre-damaged region, is introduced during the punching process for the preparation of hole expansion test specimen. The hardness profile is an effective method for quantitatively analyzing SAZ. In this study, the hardness was measured in the radial direction near the hole edge for 3 different clearance condition (Fig. 5.7). The hardness profiling was measured for the sheared and fractured zones, and measurements were made at a location 30 μm apart from both ends in the thickness direction of the specimen. In the fractured zone, work hardening due to the punching process has been found to occur up to about 300 μm from the edge of the hole. However, no significant work hardening was found in the sheared zone.

Since work hardening has occurred near the hole edge due to the punching process, the strain history at the hole edge will be different during the hole expansion tests compared to the wire cut sample which has homogeneous material properties. Therefore, to consider the hardening due to punching process, the hardness measured by position was converted into an equivalent plastic strain. First, hardness was converted into flow stress through the relationship between hardness and flow stress as follows.

$$\sigma_{fr} = -90.7 + 2.876 \times H_{fr} \quad (3)$$

The equivalent plastic strain was calculated from the previously derived stress-strain

relationship using the converted flow stress and this equivalent plastic strain was considered as a pre-strain in the FE model. Fig. 5.8 shows the comparison of the deformation history at the hole edge when the hardening effect is considered and not. When the hardening effect is considered, the amount of deformation is greater at the same step time, i.e., at the same HER value. The strain history (at the spot 1) of the case considering the hardening effect was set as the boundary condition for the microscale simulation.

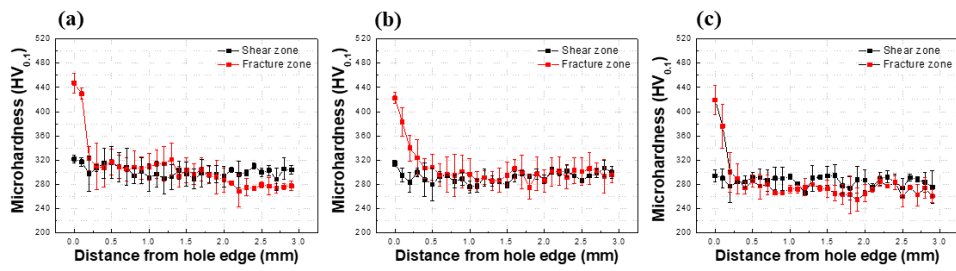


Figure 5.7 Experimentally measured hardness profile for each clearance condition.

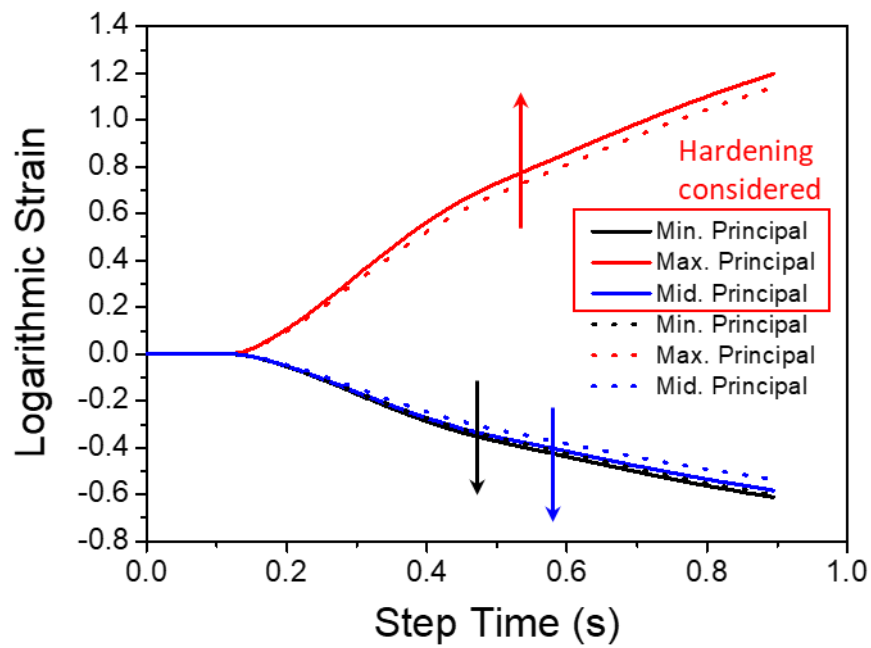


Figure 5.8 Calculated strain histories at the hole edge (spot 1) during the hole expansion test for the samples with and without hardening effect.

5.5.2 Microscale simulation

The microscale simulation was performed using the RVE of ferrite bainite steel constructed in the previous chapter. Similar to the previous macroscale simulation approach, the equivalent plastic strain introduced from the punching process was considered as a pre-strain in the form of uniaxial tension. The microscale RVE model after applying work hardening effect as a pre-strain is shown Fig. 5.9a. The microscale RVE model to which the pre-strain was applied was set as the initial microstructure for the hole expansion test simulation. After applying the pre-strain, the strain history calculated from the macroscale hole expansion test simulation for each clearance was additionally applied as a boundary condition. The averaged stress triaxiality versus equivalent plastic strain calculated from the microscale simulation of hole expansion test is shown in Fig. 5.9b and the resulting HER is shown in Fig. 5.10, and it was confirmed that the predicted value falls within the error range of the experimentally measured HER.

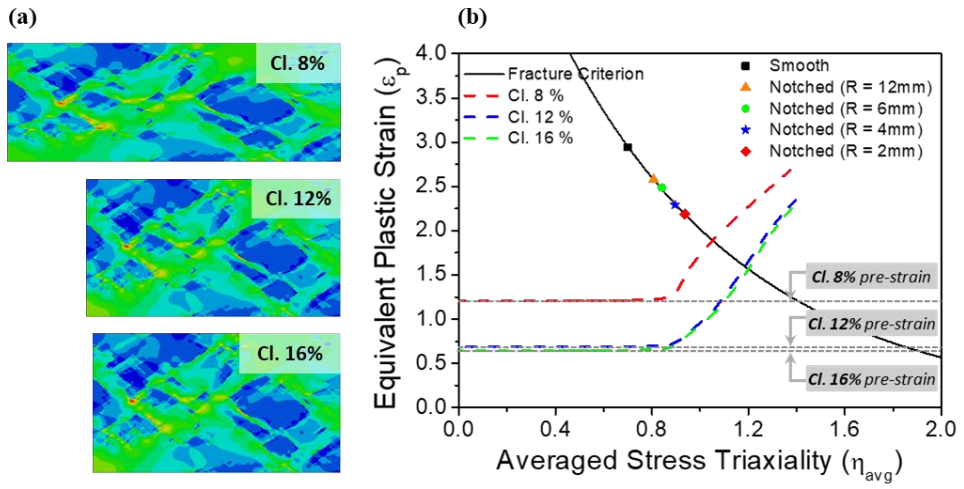


Figure 5.9 The microscale RVE model after applying work hardening effect as a pre-strain and averaged stress triaxiality versus equivalent plastic strain calculated from the microscale simulation of hole expansion test.

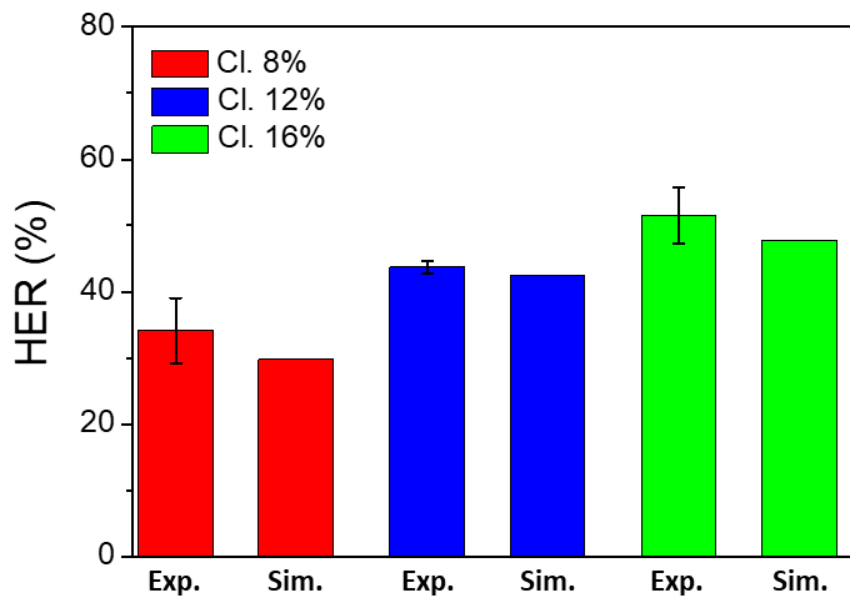


Figure 5.10 Experimental and predicted HER for each clearance condition.

5.6 Conclusion

In this chapter, the prediction of the hole expansion ratio of ferrite bainite steel was performed by considering the factors that may occur when the hole is fabricated by punching process. The damage introduced in the shearing process was analyzed by dividing it into three factors: surface roughness, geometry of the hole edge, and work hardening near the hole as factors that can affect hole expansion. The surface roughness of the hole edge was analyzed quantitatively by introducing the concept of NRD, which is the average of the height difference measured through confocal microscopy and it was confirmed that the surface roughness has little effect on HER. To analyze the effect of hole edge geometry on HER, FE modeling was performed using the measured edge geometry using a confocal microscope. From the experimental and FE simulation results, it was confirmed that the higher the clearance, the larger the slope of the fracture zone formed through the punching process, and in this case, the maximum principal strain applied to the hole edge decreased, and the HER increased. Finally, in order to investigate the effect of work hardening introduced near the hole edge from the punching process on the HER, the hardness profile was measured in the radial direction near the hole edge. The measured hardness was converted into equivalent plastic strain and considered as pre-strain in the FE model. The strain history at the hole edge was calculated for the work hardened specimen through macroscale simulation, which was reflected as the boundary condition of the microscale RVE simulation. As a result of the dual-scale FE simulation considering the geometry of hole edge and hardness profile, it was

confirmed that the predicted HER value for each clearance condition falls within the error range of the experimentally measured HER value.

5.7 References

- [1] H. Ghadbeigi, C. Pinna, S. Celotto, J.R. Yates, *Mater. Sci. Eng. A*, 527 (2010) 5026-5032.
- [2] T. Sirinakorn, S. Wongwises, V. Uthaisangsuk, *Mater. Des.*, 64 (2014) 729-742.
- [3] T. Gläsner, M. Schneider, M. Troitzsch, S. Westhäuser, *Mater. Sci. Eng.*, 159 (2016) 012029.
- [4] W. Volk, O. Böttcher, M. Feistle, C. Gaber, D. Jocham, *Advanced Failure Prediction in Sheet Metal Forming*, Institute of Virtual Manufacturing, Zurich, Switzerland (2015) 166.
- [5] J.-Y. Lee, K.-J. Lee, M.-G. Lee, T. Kuwabara, F. Barlat, *Int. J. Solids Struct.*, 156-157 (2019) 107-118.
- [6] V.K. Barnwal, S.-Y. Lee, S.-Y. Yoon, J.-H. Kim, F. Barlat, *Int. J. Fract.*, 224 (2020) 217-233.
- [7] K. Hasegawa, K. Kawamura, T. Urabe, Y. Hosoya, *ISIJ Int.*, 44 (2004) 603-609.
- [8] X. Sun, K.S. Choi, W.N. Liu, M.A. Khaleel, *Int. J. Plast.*, 25 (2009) 1888-1909.
- [9] J.H. Kim, M.-G. Lee, D. Kim, D.K. Matlock, R.H. Wagoner, *Mater. Sci. Eng. A*, 527 (2010) 7353-7363.
- [10] A. Karelova, C. Krempaszky, E. Werner, P. Tsipouridis, T. Hebesberher, A. Pichler, *Steel Res. Int.*, 80 (2009) 71-77.
- [11] N. Pathak, C. Butcher, M. Worswick, *J. Mater. Eng. Perform.*, 25 (2016) 4919-

4932.

[12] S. K. Paul, *Materialia*, 9 (2020) 100566.

[13] S.K. Paul, *J. Eng. Manuf.*, 234 (2020) 671-676.

[14] M. Stanton, R. Bhattacharya, I. Dargue, R. Aylmore, G. Williams, *AIP Conf. Proc.*, 1353 (2011) 1488.

[15] L. Chen, J.-K. Kim, S.-K. Kim, G.-S. Kim, K.-G. Chin, B.C. De Cooman, *Steel Res. Int.*, 81 (2010) 552-568.

[16] A. Konieczny, T. Henderson, *SAE Transaction*, 116 (2007) 20-29.

Chapter 6

Total conclusion

In this study, the prediction of HER for ferrite single phase (hyper burring steel) and ferrite-bainite dual phase steel was conducted using dual-scale approach. In Chapters 2 and 3, discussions on how to predict the HER of ferrite-bainite dual phase steel were discussed. Chapter 2 deals with the microstructure and mechanical properties of ferrite-bainite dual phase steel. For the ferrite-bainite dual phase steel an experimental method based on grain average IQ and grain average misorientation was presented to identify the two constituent phases of the investigated steel. The phase identification results were verified by the selective nanoindentation using SPM and the mechanical property of each phase was obtained from the macroscale nanoindentation simulation using the experimentally measured load-displacement curve.

In Chapter 3, detailed explanations have been made regarding dual-scale simulation and local stress triaxiality fracture criterion. The dual-scale model first simulated the macroscopic level of HET, from which the deformation histories of the region of interest at the hole edges were applied as boundary conditions for the subsequent microscopic simulations. The microscopic-level simulation utilized the realistic microstructure-based RVE model, which implemented dislocation-density-based constitutive equations to represent practically the flow stress hardening with

local dislocation density pile-ups near grain boundaries.

The fracture criterion for HER prediction was formulated as a function of local stress triaxiality and equivalent plastic deformation, noting on the point that the stress triaxiality is higher at the grain interior than at the grain boundary region owing to the high effective stress induced by dislocation pile-up. The predicted HER through the dual-scale simulation approach and the fracture criterion using local stress triaxiality proposed in this study had similar value to the experimentally measured one.

In Chapter 4, the model was verified by applying the dual-scale simulation introduced in the previous chapter to hyper burring steel composed of single phase ferrite. For comparison, three other conventional fracture criteria were introduced, and it was confirmed that the fracture criterion considering local stress triaxiality predicted HER more accurately. In addition, in order to analyze microstructure effects from various angles, HER was predicted according to various grain sizes and grain boundary characteristics.

In Chapter 5, the severe damage near the hole edge introduced in the shearing process was considered by dividing it into three factors: surface roughness, hole edge geometry, and work hardening. The influence of surface roughness on HER was analyzed by introducing the concept of NRD calculated from roughness data obtained using confocal microscopy and found that surface roughness did not show any relationship with HER. Regarding the effect of the hole edge shape on the HER, it was confirmed that the larger the slope of the fracture region formed through the

punching process, the lower the maximum main strain applied to the hole edge and the HER increased. To consider the work hardening near the hole edge caused by the punching process, the hardness profile was measured, which was converted into an equivalent plastic strain and set as a pre-strain in the FE model. For microscale RVE simulation, the model introduced in Chapter 3 was applied. It was confirmed that the predicted HER falls within the error range of the experimentally measured HER.

The model proposed in this study reflected microstructure factors by using the realistic microstructure-based RVE model, and grain boundary hardening could be considered by applying the dislocation-pile up model. In the case of conventional FE simulation using RVE reflecting microstructure characteristics, the application to single-phase steel has been limited because hardening due to grain boundary is not considered. Therefore, the model proposed in this study considering dislocation-pile up at the grain boundary has significance that it can be applied to a wider variety of materials, and can be used for optimal microstructure design.

국문 초록

최근 자동차의 연비 및 CO₂ 가스 배출량 규제에 대한 관심이 증가함에 따라 자동차용 경량 소재에 대한 연구가 활발히 수행되고 있다. 이에 따라 기존 철강에 비해 강도와 연신이 우수한 고강도강(AHSS)을 개발하였지만 자동차 부품 성형 중 발생하는 모서리 균열(edge crack)은 실제 공정의 적용에 여전히 문제가 되고 있다. 판재 성형 공정 중 성형 한계를 예측하기 위한 연구로는 일반적으로 성형 한계도(FLD)와 관련된 연구가 많이 수행되었다. 하지만 모서리 균열의 경우 파단 전 변형을 극소화(strain localization)가 일어나지 않기 때문에 일축 인장 시험 또는 성형 한계도를 기반으로 한 성형성 평가 방법으로 파단을 예측하는 것은 적절하지 않다. 따라서 기존의 성형성 평가 방법을 대체하고 판재의 모서리 또는 플랜지(flange)의 균열을 포함하는 신장-플랜지성(stretch-flangeability)에 대한 평가 방법으로 구멍 확장 시험(hole expansion test, HET)이 고안되었다. 구멍 확장성은 초기와 균열이 발생한 시점에서 구멍의 직경비로 정의되는 값으로 재료의 미세조직에 상당한 영향을 받는 것으로 알려져 있다.

본 연구에서는 페라이트-베이나이트강 및 페라이트 단상강의 구멍 확장성을 예측하기 위해 미세조직 기반 다중 스케일 시뮬레이션(dual-

scale simulation)이 고안되었다. 다중 스케일 시뮬레이션의 첫번째 단계에서는 구멍 확장 시험 간 시편의 거시적 변형 해석이 수행되며, 거시 스케일의 변형 해석을 통해 얻은 관심 영역에서의 변형 이력은 두번째 단계인 미시적 변형 해석에서의 경계조건으로 활용되었다. 거시 스케일 해석은 강재의 이방성을 고려해주기 위하여 Hill의 이차항복식이 적용되었으며, 압연 방향을 기준으로 0° , 45° , 90° 에 대하여 변형 이력이 추출되었다. 미시 스케일의 변형 해석은 재료의 미세조직을 고려하기 위하여 후방산란전자회절분석기(EBSD) 관찰 결과를 통해 구축된 대표 체적 요소(RVEs)를 활용하였다. 재료의 구성상을 구별하기 위하여 EBSD로부터 얻어진 평균 결정립 이미지질(grain average image quality)과 평균 결정립 어긋남각(grain average misorientation)을 활용하였으며, 상 분리 결과는 나노압입시험(nanoindentation test)과 주사 탐침 현미경(scanning probe microscopy)을 활용하여 수행된 선택적 압입시험으로 측정된 압입하중-변위곡선으로부터 검증되었다. 구성 방정식은 결정립계에서의 전위 집적(dislocation pile-up)을 고려하기 위하여 전위 밀도 기반 경화식을 채택하였으며, 전위 밀도는 결정립계로부터 거리에 대한 함수의 형태로 설정하여 기존의 식을 재구성 해 주었다. 각 상 별 기계적 물성은 나노압입시험을 통해 측정되었으며 이를 통해 상 별 강화 거동을 수치적으로 고려해 주었다.

파괴 기준은 유효변형률과 삼축응력비에 대한 함수의 형태로 도출되었으며, 해당 강재의 파괴 기준 설정을 위해 2, 4, 6, 12 mm의 반경을 갖는 노치 인장 시험편을 제조하여 실험과 해석을 수행하였다.

편칭(punching)에 의한 구멍 근처의 손상은 표면 거칠기와 구멍 단면부의 형상, 가공 경화의 세 인자로 나누어 고려되었다. 표면 거칠기와 구멍 단면부의 형상은 공초점 현미경(confocal microscopy)을 활용하여 측정이 이루어졌으며, 측정된 수치데이터를 활용하여 모델링을 수행하였다. 편칭으로 인한 가공 경화는 구멍 근처의 경도 프로파일을 통해 분석되었으며, 측정된 경도는 유효변형률로 변환되어 예변형의 형태로 유한요소해석 모델에 반영해 주었다.

제안된 다중 스케일 모델은 실험 오차 범위 내에서 구멍 확장성을 정확하게 예측하였을 뿐 아니라 균열이 발생한 위치 역시 예측이 가능한 것으로 확인되었다. 또한 해당 모델은 실제 미세조직이 반영되어, 결정립의 형상 및 크기와 같은 미세조직적 요인들이 구멍 확장성에 미치는 영향을 정량적으로 분석할 수 있기 때문에, 최적 미세조직의 설계를 위한 도구로 활용될 수 있다. 이와 더불어, 파괴 기준을 설정하기 위한 거시 스케일에서의 실험량을 현저히 줄일 수 있어 시간적, 비용적 측면에서도 효율적이라고 평가될 수 있다.

핵심어: 구멍 확장성, 고강도강, 연성 파괴, 대표 체적 요소, 상분리, 전위, 파괴 기준, 다중 스케일 유한요소해석, 나노압입시험, EBSD, TEM

Student number: 2015-20818